2015-9

Tapered Optical Microfibre Based Structures for Sensing Applications

Lin Bo
Technological University Dublin

Tapered Optical Microfibre Based Structures for Sensing Applications

By

Lin Bo

Supervisors: Prof. Gerald Farrell
Prof. Yuliya Semenova
Dr. Pengfei Wang

School of Electrical and Electronic Engineering
College of Engineering and Built Environment
Dublin Institute of Technology

A thesis submitted for the degree of Doctor of Philosophy

September 2015

Abstract

There has been an increasing demand in recent years from a wide variety of industries for sensors which combine high sensitivity, fast response, compact size and low power consumption. Tapered optical microfibres can generate easily accessible evanescent fields with a large intensity and short decay distance which make microfibres very suitable candidates as the basis of sensors to suit a variety of application areas.

In this thesis, experimental research is presented concerning the development of sensors using structures based on tapered optical microfibres, with a particular emphasis on biochemical sensing applications.

Light propagation along an optical microfibre depends on its shape, diameter and surface roughness. A microfibre fabrication setup developed as a key prerequisite to the research undertaken, that utilized an adapted microheater brushing and tapering technique is described. The setup allows for the fabrication of microfibres and related structures with controllable taper shapes and diameters.

There is a tradeoff between sensitivities and microfibre diameters (which directly affects the robustness of the microfibre structures) for microfibre based sensors. To mitigate this tradeoff, two microfibre based structures were chosen and investigated for sensor development in the research reported in this thesis.

The first structure was an optical microfibre coupler. Such an optical microfibre coupler, which has environment dependent coupling coefficients in addition to easily accessible evanescent fields, is a simple and efficient structure for sensing. A refractive index sensor with a maximum sensitivity of 4155 nm/RIU was developed using an optical microfibre coupler. Utilizing the structure's refractive index sensitivity, a humidity sensor was developed by coating a microfibre coupler with a layer of humidity sensitive polymer. A biosensor was also developed by immobilizing a bio-receptor on the surface of a packaged microfibre coupler. The ability of the developed biosensor to detect the specific binding between an antibody-antigen pairing for potential applications in clinical diagnostics was demonstrated and is reported in this thesis.

The second structure was a tapered optical microfibre which incorporates gold-silver alloy nanoparticles. By immobilizing nanoparticles onto the surface of a tapered optical

microfibre to generate localized surface plasmon resonances, sensitivity enhancement can be achieved for microfibres with relatively large diameters, which has the benefit of being more mechanically robust. The use of gold-silver alloy nanoparticles with different alloy formulations can offer the extra advantage of tunable physicochemical properties. The localized surface plasmon resonance effects were investigated and compared for sensor samples incorporating nanoparticles with different alloy formulations. As an example of a sensing application using the structure, a novel pH sensor was demonstrated by coating the immobilized nanoparticles with a pH sensitive polyelectrolyte multilayer film.

Declaration

I certify that this thesis which I now submit for examination for the award of Doctor of Philosophy, is entirely my own work and has not been taken from the work of others, save and to the extent that such work has been cited and acknowledged within the text of my work.

This thesis was prepared according to the regulations for postgraduate study by research of the Dublin Institute of Technology and has not been submitted in whole or in part for an award in any other Institute or University.

The work reported on in this thesis conforms to the principles and requirements of the institute's guidelines for ethics in research.

The Institute has permission to keep, to lend or to copy this thesis in whole or in part, on condition that any such use of the material of the thesis be duly acknowledged.

Lin Bo

Signed: _____

Date: _____

Acknowledgements

This thesis could not have been completed without a number of people who have guided, helped and supported me throughout the course of my PhD.

Firstly, I would like to thank Prof. Gerald Farrell, whom I was fortunate to have as my supervisor. The most elucidating moments I had in my PhD were through my interaction with him. Trying to follow his keen mind during a meeting could be a bit stressful, but always rewarding. A Chinese proverb can adequately express my gratitude to Gerry, "I benefit more from one conversation with you than from ten years of reading".

I would also like to thank my co-supervisors, Prof. Yuliya Semenova and Dr. Pengfei Wang. Yuliya's wisdom has helped me overcome many difficulties on the way of pursuing my PhD. Her views and encouragement have helped eliminate many doubts and moments of hesitation. Pengfei's practical advice and guidance opened the door of research for me and helped build my confidence, especially when I was dreadfully "illiterate" about how to carry out research at the beginning of this PhD.

Within our Photonic Research Centre, I would also like to thank Dr. Qiang Wu, who taught me many things about fibre optics and Dr. Mingwei Yang who patiently answered many questions and helped solve several problems I encountered in experiments. I am also grateful to Dr. Ginu Rajan, Dr. Sunish Mathews, Dr. Jinesh Mathew, Ms. Manjusha Ramakrishnan, Mr. Youqiao Ma, Mr. Vishnu Kavungal, Mr. Dejun Liu and Mr. Arun Kumar Mallik for all the help they provided. It was my pleasure to work with them.

I really appreciated my opportunity to work with Dr. Christy Charlton O'Mahony and Dr. Niamh Gilmartin on biosensing experiments and with Dr. João Conde and Dr. Furong Tian on nanoparticle experiments. Their expertise has expanded my knowledge and added much value to my work. I am also thankful to Dr. Timothy Lee who kindly shared his simulation work with me and Dr. Benjamin Schazmann who provided assistance in microfibre surface modification.

I am extremely grateful to my family, including my mother, father, brother, sister-in-law and my wonderful nephew for their unconditional love and support. Finally, I want to thank my boyfriend Colm. He shines full-spectrum light into my life, nourishing and vitalizing me, simply making me happy every day.

Contents

List of Publications

Journals:

1. **L. Bo**, Y. Semenova, J. Conde, F. Tian, B. Schazmann, P. Wang, and G. Farrell, "Localized surface plasmon resonance effect based optical microfibre sensor incorporating gold-silver alloy nanoparticles," submitted to *Sens. Actuators B Chem*..
2. P. Wang[*], **L. Bo**[*], Y. Semenova, G. Farrell, and G. Brambilla, "Optical microfibre based photonic components and their applications in label-free biosensing," *Biosensors*, vol. *5*, no. 3, pp. 471–499, Jul. 2015.
3. **L. Bo**, C. C. O'Mahony, Y. Semenova, N. Gilmartin, P. Wang, and G. Farrell, "Microfiber coupler based label-free immunosensor," *Opt. Express*, vol. 22, no. 7, pp. 8150–8155, Apr. 2014.
4. **L. Bo**, P. Wang, Y. Semenova, and G. Farrell, "High sensitivity fiber refractometer based on an optical microfiber coupler," *IEEE Photonics Technol. Lett.*, vol. 25, no. 3, pp. 228–230, Feb. 2013.
5. **L. Bo**, P. Wang, Y. Semenova, and G. Farrell, "Optical microfiber coupler based humidity sensor with a polyethylene oxide coating," *Microw. Opt. Technol. Lett.*, vol. 57, no. 2, pp. 457–460, Feb. 2015.
6. P. Wang, **L. Bo**, C. Guan, Y. Semenova, Q. Wu, G. Brambilla, and G. Farrell, "Low-temperature sensitivity periodically tapered photonic crystal-fiber-based refractometer," *Opt. Lett.*, vol. 38, no. 19, pp. 3795–3798, Oct. 2013.
7. P. Wang, M. Ding, **L. Bo**, C. Guan, Y. Semenova, W. Sun, L. Yuan, G. Brambilla, and G. Farrell, "Photonic crystal fiber half-taper probe based refractometer," *Opt. Lett.*, vol. 39, no. 7, pp. 2076–2079, Apr. 2014.
8. P. Wang, M. Ding, **L. Bo**, C. Guan, Y. Semenova, Q. Wu, G. Farrell, and G. Brambilla, "Fiber-tip high-temperature sensor based on multimode interference," Opt. Lett., vol. 38, no. 22, pp. 4617–4620, Nov. 2013.
9. P. Wang, M. Ding, **L. Bo**, Y. Semenova, Q. Wu, and G. Farrell, "A silica singmode fibre-chalcogenide multimode fibre-silica singlemode fibre structure," *Photonics Lett. Pol.,* vol. 4, no. 4, pp. pp. 143–145, Dec. 2012.
10. P. Wang, M. Ding, G. S. Murugan, **L. Bo**, C. Guan, Y. Semenova, Q. Wu, G. Farrell, and G. Brambilla, "Packaged, high-Q, microsphere-resonator-based add-drop filter," *Opt. Lett.*, vol. 39, no. 17, pp. 5208–5211, Sep. 2014.

11. P. Wang, T. Lee, M. Ding, Z. Lian, X. Feng, Y. Ma, **L. Bo**, Q. Wu, Y. Semenova, W. Loh, G. Farrell, and G. Brambilla, "White light trapping using supercontinuum generation spectra in a lead-silicate fibre taper," *J. Light. Technol.*, vol. 32, no. 1, pp. 40–45, Jan. 2014.
12. P. Wang, M. Ding, T. Lee, G. S. Murugan, **L. Bo**, Y. Semenova, Q. Wu, D. Hewak, G. Brambilla, and G. Farrell, "Packaged chalcogenide microsphere resonator with high Q-factor," *Appl. Phys. Lett.*, vol. 102, no. 13, p. 131110, Apr. 2013.
13. P. Wang, G. Brambilla, M. Ding, T. Lee, **L. Bo**, Y. Semenova, Q. Wu, and G. Farrell, "Enhanced refractometer based on periodically tapered small core singlemode fiber," *IEEE Sens. J.*, vol. 13, no. 1, pp. 180–185, Jan. 2013.
14. P. Wang, C. C. O'Mahony, T. Lee, R. Ismaeel, T. Hawkins, Y. Semenova, **L. Bo**, Q. Wu, C. McDonagh, G. Farrell, J. Ballato, and G. Brambilla, "Mid-infrared Raman sources using spontaneous Raman scattering in germanium core optical fibers," *Appl. Phys. Lett.*, vol. 102, no. 1, p. 011111, Jan. 2013.

Conference proceedings:

1. **L. Bo**, C. C. O'Mahony, P. Wang, Y. Semenova, and G. Farrell, "Microfiber coupler based biosensor for immunoglobulin G antigen detection," in *Asia Communications and Photonics Conference*, 2013, p. AF2I.20.
2. **L. Bo**, P. Wang, Y. Semenova, G. Brambilla, and G. Farrell, "An investigation of the polarization dependence of a temperature sensor based on an optical microfiber coupler," in *22nd International Conference on Optical Fiber Sensors*, 2012, p. 84217Y–84217Y–4.
3. Y. Semenova, **L. Bo**, P. Wang, F. Tian, H. Byrne, and G. Farrell, "Microfiber coupler based biosensor incorporating a layer of gold nanoparticles with improved sensitivity," in *23rd International Conference on Optical Fiber Sensors*, 2014, p. 91578T.
4. G. Farrell, **L. Bo**, C. Guan, Y. Semenova, and P. Wang, "Periodically tapered photonic crystal fibre based strain sensor fabricated by a CO_2 laser technique," in *SPIE Photonics Europe*, 2014, p. 91280G.
5. V. Kavungal, **L. Bo**, Q. Wu, M. Teng, C. Yu, G. Farrell, and Y. Semenova, "Study of whispering gallery modes in a cylindrical microresonator excited by a tilted fiber taper," in *23rd International Conference on Optical Fiber Sensors*, 2014, p. 91578N.
6. Y. Semenova, **L. Bo**, P. Wang, S. Mathews, Q. Wu, M. Teng, C. Yu, and G. Farrell, "Experimental study of temperature response of a microfiber coupler sensor with a

liquid crystal overlay," in *22nd International Conference on Optical Fiber Sensors*, 2013, p. 87942L.

7. P. Wang, **L. Bo**, Y. Semenova, G. Farrell, G. Brambilla, "A multimode fibre tip based temperature sensor," in *OSA Sensors*, 2013, p. SM2D.4.

Abbreviations

Au	Gold
Ag	Silver
BBS	Broadband source
BSA	Bovine serum albumin
BSE	Back-scattered electron
EDX	Energy-dispersive X-ray spectroscopy
FBG	Fibre Bragg grating
FE-SEM	Field emission scanning electron microscope
FFT	Fast Fourier transform
FSR	Free spectral range
FWHM	Full width at half maximum
ICP	Inductively coupled plasma
IgG	Immunoglobulin G
LbL	Layer-by-layer
LPG	Long period grating
LSPR	Localized surface plasmon resonance
MI	Michelson interferometers
MZI	Mach-Zehnder interferometer
OMC	Optical microfibre coupler
OSA	Optical spectrum analyzer
PAH	Poly(allylamine hydrochloride)
PBS	Phosphate-buffered saline
PCF	Photonic crystal fibre
PDMS	Polydimethylsiloxane
PEM	Polyelectrolyte multilayers
PEM-NP-PEM	PEM-nanoparticle-PEM
PEO	Polyethylene oxide
PMF	Polarization-maintaining optical fibre
PSS	Poly(styrene sulfonate)
PTFE	Polytetrafluoroethylene
Q factor	Quality factors
RI	Refractive index

RIU	Refractive index unit
RH	Relative humidity
SEM	Scanning electron microscope
SDS	Sodium dodecyl sulphate
SMF	Single-mode fibre
SMS	Singlemode-multimode-singlemode
SPR	Surface plasmon resonance
TEM	Transmission electron microscope
UV	Ultraviolet
WGM	Whispering gallery mode

List of Figures

List of Tables

Chapter 1

Introduction

Optical fibres have played a critical role in modern telecommunications since the development of low-attenuation optical fibres for long-distance light transmission in the 1970s [1]. In parallel with the development of fibre waveguides and optical fibre based components for communication purposes, significant effort has also been invested in exploiting optical fibres' potential for sensing in a variety of application areas. Various sensors have been developed using optical fibres to detect physical and chemical parameters such as temperature, strain, vibration, pH, etc. In general, the sensing capability is achieved by allowing the transmitted light in an optical fibre to interact with the measurands in the surrounding medium. The intensity, phase, polarization and wavelength of the transmitted light can be modified by local environmental parameters and in turn can convert the measurands to measurable and quantifiable optical signals. Compared with conventional electronic sensors, optical fibre sensors offer useful advantages such as high sensitivity, small size, light weight, immunity to electromagnetic field interference, capability to work in high temperature environments and the potential for remote operation [2]. As a result, numerous optical fibre sensors have been developed in the past few decades to facilitate sensing applications in areas such as environmental monitoring, manufacturing control, national security, aerospace etc.

With the rise of biomedical and nano technologies in recent years, there is an increasing demand for high-performance miniaturized sensors to provide sensitive and fast detection of measurands such as chemical compounds, biomolecules and cells. Conventional optical fibres allow limited access to the evanescent field and show inefficient light-environment interactions that make it difficult to use such fibres for

many micro/nano-scale sensing applications. One way to get access to the evanescent fields is by removing part of the fibre cladding through mechanical polishing or chemical etching. However such cladding-removed optical fibres suffer from residual surface roughness and poor control over the diameter of the decladded fibre section. The polishing and etching procedures are also complex and time consuming.

The development of optical microfibres provides a more efficient and promising solution to meet the challenge. Optical microfibres are optical fibres with diameters which are comparable with the wavelength of the transmitted light. The diameters of optical microfibres are in the range of a few micrometers which means such fibres are much smaller than conventional optical fibres which have a typical diameter of 125 μm. The small diameters of optical microfibres can be achieved by either drawing fibres from bulk glass material or by heating and stretching conventional optical fibres to form tapered microfibres. The latter approach is preferable because it allows the retention of the original fibre input and output ends, which facilitate fibreized input and output connections with negligible losses. Most of the microfibre based devices developed to date have been based on tapered optical microfibres. The resultant small diameter of optical microfibres provides several advantages over conventional optical fibres [3]:

- **More effective access to the evanescent field**. For conventional optical fibres, light is transported within the fibre via total internal reflection. From an intuitive perspective this means that the optical fibre works as a "light pipe". For optical microfibres, a substantial proportion of light can propagate outside the fibre. In this case, the fibre can be viewed working as a "light rail". Such a light-guidance configuration allows the evanescent fields to interact with the measurands in the surrounding medium in a much more efficient way. As a result, measurands that cannot be detected using conventional fibres can be detected using microfibre based sensors. Additionally, even for measurands that are detectable using conventional fibre sensors, it is found that detection sensitivities can be enhanced by using microfibre based sensors [4].
- **Greater versatility of configuration**. Optical microfibres can be bent and manipulated into various structures with low bend loss. Conventional optical fibres suffer from bend induced attenuation when the bend radii are of several centimetres [5]. Optical microfibres can achieve a millimetre- or even micrometre-order bend

radii with low bend loss. Thus the potential for sensor miniaturization can be enhanced with microfibre based structures.

- **Stronger mode confinement/Shorter decay distance of the evanescent field**. The evanescent field can be restrained within a small distance close to the microfibre surface. This is due to the large difference in refractive index (RI) between the silica microfibre and the surrounding medium (usually air or water), described further in Section 2.2.1. This small decay distance and high intensity of the evanescent field are particularly useful when using microfibres to detect small particles such as chemical compounds and biomolecules. Such molecular scale induced environmental changes can occur very close to the microfibre surface (normally within tens of nanometres) and the high intensity of the evanescent field close to the surface of a microfibre is a significant advantage in this case.

In general, measurand induced changes in light propagation in optical fibre based sensors can be detected in one of the following domains: intensity, phase, wavelength, or polarization state. A single tapered optical microfibre can work as a sensing element in the intensity domain (that is the detected light intensity at the interrogation system is used as a measure) but this is only possible if a strong light-environment interaction is available. The dimensions for a single microfibre to exhibit such a large evanescent field fraction are essentially within the sub-wavelength scale [6]. Microfibres with such small diameters (less than 1 μm) are very fragile, have poor mechanical stability and are difficult to manipulate. Moreover, overly thin microfibres are more likely to exhibit high loss due to surface degradation and contamination. Therefore it is more practical to develop sensors using microfibres which have relatively large and thus easily manageable diameters (typically over 2 μm). However larger diameter microfibres generate smaller evanescent fields compared with sub-wavelength diameter microfibres. Thus insufficient intensity-environment interactions can occur, reducing sensitivity when used for sensing. However this tradeoff between stability and sensitivity can be mitigated by adopting one of two approaches thus:

1. Utilize phase-sensitivity: This approach involves forming phase-sensitive microfibre structures via the mode interference within a microfibre or the light intercoupling between adjacent microfibres. Typical structures include nonadiabatic single microfibres, microfibre based interferometers, some microfibre based resonators, and optical microfibre couplers (OMC). These structures can offer effective phase-

environment interactions with easily manageable diameters, but with the consequence that wavelength domain operation becomes necessary. These structures are further explained in Section 2.2.

2. Utilize high intensity non-fibre resonances: This approach involves combining microfibres with higher intensity resonances such as those induced by localized surface plasmon resonance (LSPR). The evanescent field of a microfibre can excite LSPR around conductive nanoparticles which are deposited on the microfibre surface [7]. It is known that LSPRs have higher intensities and even shorter field decay distances than the evanescent fields of microfibres [8]. Biomolecules attached to the nanoparticles' surface can efficiently modify the LSPR and in turn modify light transmission along the optical microfibre.

In Chapter 2 of this thesis the fundamentals of microfibres are considered in more detail along with examples of application areas for microfibre based sensing.

1.1 Motivation

This thesis presents research on the development of sensors utilizing simple microfibre based structures that can be easily fabricated. As outlined above, the development of sensitive microfibre based sensors with fibre diameters larger than the sub-wavelength regime are desirable to ensure good mechanical stability but necessitate the use of the two approaches outlined above to ensure efficient light-environment interactions.

In regard to the first approach that utilizes phase-sensitivity, this thesis focuses on using an OMC structure as the basis of sensors. An OMC has a very similar structure to that of a conventional fused optical fibre coupler. The main difference between the two is that an OMC has a much smaller diameter, usually in the order of few micrometers [9]. Among the various phase-sensitive structures mentioned earlier, an OMC structure shows potentially high sensitivity and its fabrication is relatively straightforward and does not involve complex manipulations of the microfibres to form the necessary structure. The coupling coefficient of an OMC can be highly dependent on the RI of the surrounding medium [10]. However, apart from the use of an OMC structure as a high temperature sensor demonstrated in 2012 [11], many sensing applications of OMCs

have not been explored in detail. One important example is that the potential for an OMC structure to work as a biosensor has remained unexplored. In principle such sensors are possible since biomolecules which adsorb on the OMC surface, particularly along the fused area between the two microfibres, can effectively modify the local RI profile and change the coupling coefficient.

In regard to the second approach that utilizes non-fibre resonances, this thesis focuses on combining microfibres with gold-silver (Au-Ag) alloy nanoparticles to generate LSPR as the basis of sensors. Gold and silver nanoparticles have been extensively studied for LSPR based sensors. A wide range of biochemical sensing applications for clinical diagnostics, imaging, therapeutics and drug delivery have been developed utilizing gold or silver nanoparticles [12]. Microfibre based LSPR biosensors in conjunction with gold or silver nanoparticles have also been extensively studied [13][14]. However, the use of Au-Ag alloy nanoparticles for microfibre based LSPR sensors has received no attention to date, which is a shortcoming in knowledge in this area since the physicochemical properties of Au-Ag alloy nanoparticles can be tuned by varying the alloy formulation [15] to good effect in sensor design. A key motivation in this thesis is to explore this untapped advantage of alloy nanoparticles combined with microfibres.

1.2 Objectives

The research reported in this thesis aims to explore the sensing potential for (1) OMC structures and (2) microfibre and alloy nanoparticle facilitated LSPR structures. The specific objectives of the research were:

- **To develop microfibre fabrication facilities.** The development of a robust microfibre fabrication technique was required as a key prerequisite to the research. The light guidance properties of a tapered optical microfibre greatly depend on the shape and diameter of the tapers. Therefore the development of a flexible automated fibre tapering process controlled by a computer program was required to facilitate fabrication of microfibres with controllable shapes and diameters.
- **To develop a high sensitivity RI sensor using an OMC.** An OMC has the potential to work as a high sensitivity refractometer given its RI dependent coupling coefficient. Moreover, many sensing applications rely on the detection of the

surrounding RI changes via a change in an applied coating for example. By investigating the RI dependence of the OMC structure it is possible to underpin not only RI sensing, but also to deliver prerequisite work for the development of OMC based biosensors.

- **To develop a label-free biosensor based on an OMC.** By immobilizing suitable receptor on the microfibre surface, an OMC has the potential to work as a biosensor to detect specific analytes of interest. The design of a biosensor with high selectivity, good stability and repeatability was essential to achieve reliable sensing results.
- **To develop an LSPR based sensor combining a microfibre with Au-Ag alloy nanoparticles.** The first objective, essential for sensor fabrication, involved carrying out investigations on deposition methods and processing of alloy nanoparticles on the microfibre surface. A comparison of the LSPR effects and the consequent RI sensitivity among sensors incorporating nanoparticles with different Au-Ag alloy formulations were required to understand the effects of nanoparticles' Au-Ag ratios for a microfibre based LSPR sensor. The results were also required to demonstrate the tunable sensing properties of the structure.

1.3 Thesis structure

Following this introduction chapter, there are five subsequent chapters. Chapter 2 starts with an overview of the light guiding properties of optical microfibres with an emphasis on the generation and theoretical characterization of evanescent fields. The fabrication process for the microfibres used in this research is then described. In the last section of this introduction chapter, a review based on the existing literature is provided for a variety of microfibre structures for sensing applications, emphasizing OMC based sensors and microfibre facilitated LSPR sensors.

Chapter 3 presents the theoretical and the experimental results of studies of a RI sensor based on an OMC. The polarization effects, temperature dependency and humidity dependency are experimentally demonstrated. These results provided useful information on system interrogation for the OMC based sensors. The results presented in Chapter 3 also underpin the work which follows in the subsequent chapter on OMC based biosensors.

In Chapter 4 a label-free biosensor is reported using an packaged OMC structure. The development of the sensor starts with preliminary work on verifying the structure's capability to detect the RI changes occurring within a few nanometres from the surface of the OMC. This was done by detecting polyelectrolyte multilayers (PEM) assembled on the OMC surface. Then the principle and operation of an OMC based label-free immunosensor is demonstrated using fibrinogen antibody-antigen pairing. Results on the detection of Immunoglobulin G (IgG) using an anti-IgG functionalized OMC are also presented, demonstrating that OMC based immunosensors have potential for clinical diagnostics.

Chapter 5 begins by briefly describing the synthesis of the Au-Ag alloy nanoparticles. A method to immobilize the nanoparticles on the surface of microfibres is then described. The LSPR effects are compared for Au-Ag nanoparticles with various alloy formulations. Then the performance of the microfibre based LSPR structure in detecting RI changes occurring in the vicinity to the fibre surface is investigated. The capability of the structure to detect PEM adsorbed on the nanoparticles' surface is also demonstrated. A potential application for such a microfibre based LSPR structure to work as a pH sensor is demonstrated. The pH sensor utilizes a composite nanostructure which consists of alloy nanoparticles which have an alloy formulation of 50% gold and 50% silver and pH sensitive PEM as the sensing element.

Finally, Chapter 6 summarizes the results achieved in this thesis, draws overall conclusions and proposes several potential research directions into which the current work can be extended.

Chapter 2

Tapered Optical Microfibres

This chapter presents an overview of the (1) optical guidance properties; (2) fabrication and (3) sensing applications of optical microfibres. In considering the first topic on the optical guiding properties of microfibres, including the intensity and radial decay profile of the evanescent field generated by a 2 μm diameter microfibre are investigated, with the justification that the sensing capability of a microfibre relies on efficient light-environment interactions facilitated by the evanescent field (as explained in Section 1.2).

Various methods have been developed to fabricate silica optical microfibres. Examples include direct drawing from bulk glass [16], chemical etching [17] and self-growth from silica nanomaterial [18]. However, tapering from standard optical fibres remains a widely used method for fabricating microfibre based sensors to date due to the advantages of this method such as low fabrication induced losses, a smooth taper surface and the ease with which low-loss connections can be made to other optical fibre devices [19]. In considering the second topic on microfibre fabrication, a fabrication process based on a microheater brushing technique [19] is introduced in this chapter. The design and implementation of a custom fabrication setup used and the model used to control the geometry of the fabricated microfibres are also presented.

A wide range of sensing applications based on optical microfibres have been proposed in the last decade. Microfibre based structures such as single microfibres, microfibre based interferometers, resonators and couplers have been used to develop sensors. Structures combining microfibres with non-fibre resonators such as metallic nanoparticles and WGM resonators have also been proposed. The measurands range from RI and

temperature to more sophisticated parameters such as acceleration, acoustic emissions, electric field, and biochemical molecules. A review on the sensors developed based on these structures is given in this chapter.

2.1 Optical microfibres

Research on tapered optical fibre structures with diameters smaller than those of standard optical fibres date back to the 1970s [20]. Typical taper diameters ranging from several to tens of micrometers were fabricated and used. In these early investigations, using tapers fabricated by heating and stretching standard optical fibres, it was found that the tapered fibres experience mode variations along the conically tapered sections. The interest of researchers was mainly focused on reducing the excess loss of the tapers [21] and studying mode evolutions along the conically shaped tapers [22][23][24] during the early-stage development. Applications in optical filtering [25], amplification [26] and supercontinuunm generation [27] were proposed for optical communications based on tapered optical fibres. Some work was also carried out to explore the potential of tapered optical fibres for sensing using the evanescent fields [28] or the bending effects in the tapers [29]. In 1999, Moar et al. directly measured the evanescent fields of tapered optical fibres using scanning near field optical microscopy [30]. That work provided further understanding of the evanescent fields generated by tapered optical fibres for sensor development. From the late 1990s, research interests started to shift to optical fibres with even smaller diameters, in the subwavelength range, sometimes described as “subwavelength diameter optical fibres" or “nanofibres”. Bures et al. published a theoretical study of the evanescent field generated by fibre tapers with subwavelength diameters (down to nanometre scale) [31]. However low-loss fabrication of such optical nanofibres remained impractical until the experimental demonstration of optical fibres with nanometre-scale diameters drawn from bulk silica by Tong et al. in 2003 [32]. This breakthrough research opened the way to a new range of optical fibre based applications, such as atom trap and particle manipulation [33][34][35]. Such optical nanofibres also raised the sensing ability of fibre based sensors to a new level with reports such as single molecule detection [36].

Although optical nanofibres with subwavelength diameters have exciting potential in sensing, their experimental realization is difficult due to nanofibres’ poor mechanical

stability and difficulties in manipulation. Therefore in parallel with extensive theoretical explorations of the potential of nanofibres, many experimental explorations are focused on using optical microfibres, more specifically tapered optical microfibres, with microscale diameters that are slightly above the wavelengths of the transmitted light. As explained in Chapter 1, such tapered optical microfibres still possess some of the advantages of nanofibres but are easier to fabricate and more practical for experimental demonstrations.

A typical tapered optical microfibre has a shape and structure as shown in Fig. 2.1. The tapered microfibre consists of a uniform diameter waist region at the center and two tapering transition regions. The fibre ends retain the original untapered fibre dimension and thus can be easily connected to other standard optical fibres.

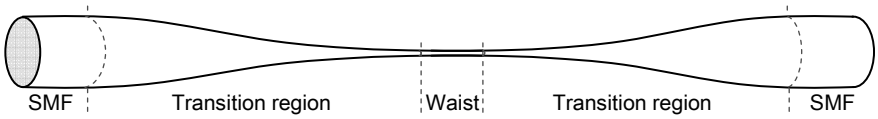

Figure 2.1: Schematic diagram of a tapered microfibre with a uniform waist region in the center which is connected to the original fibre ends via two transition regions.

In principle, the optical properties of the tapered microfibre depend on the geometry of both the transition and the waist regions. However the waist region plays the key role in sensing because the waist region exhibits the largest evanescent field. In this thesis only adiabatic tapers where light can propagate along the tapered region with negligible loss for the fundamental modes are considered [37]. As a result it is practical to consider only the uniform waist region in the design and simulation of optical microfibres for sensing purposes to avoid unnecessary complexity in modelling.

2.1.1 The evanescent fields of optical microfibres

A standard single-mode optical fibre (SMF) has a step-index core-cladding structure. The typical diameters of the core and cladding are 8 μm and 125 μm respectively. The RI of the fibre core is slightly higher than that of the cladding to achieve the weakly-guiding condition [38]. Due to the small RI difference between the core and the cladding, the weakly-guided fundamental modes have a mode field diameter which exceeds that of

the core and thus extends into the cladding with the result that a substantial fraction of the light propagates within the cladding as evanescent field. However, this evanescent field is not accessible for sensing purposes due to the large diameter of the cladding relative to the mode field diameter. In the case of tapered optical microfibres, the total fibre diameter is reduced to a few micrometers. The evanescent field extends into the surrounding medium, effectively propagating outside of the fibre. It is by this means that the evanescent field of an optical microfibre is accessible and can be utilized for sensing.

It should be noted that when the diameter of a tapered optical microfibre is greatly reduced, the original fibre core at the waist region is effectively of negligible dimension. In this case, an optical microfibre can be considered as a cylindrical waveguide with a homogeneous RI profile. The surrounding environment becomes the microfibre's "cladding". Since a significant proportion of light propagates outside of the microfibre, it is necessary for the cladding media to have a lower RI value than the microfibre, so an adequate level of confinement for light to propagate along the microfibre can be achieved. Depending on the proposed application, typical "claddings" for microfibres can be air, water or low RI polymer materials.

The propagating electric and magnetic fields of an optical microfibre can be calculated by solving Maxwell's equations in a similar manner to that used for a standard SMF. However due to the higher contrast of the RIs between the optical microfibre and the environment-cladding, a weakly-guiding approximation (where the index difference between the core and cladding is close to 1%) used for standard SMF cannot be generally used for the case of optical microfibres. Therefore light propagation along an optical microfibre needs to be calculated by rigorously solving Maxwell's equations for a uniform cylindrical waveguide with a homogeneous index profile [39].

Due to the large index difference between the core and the cladding, optical microfibres with relatively large diameters (a few micrometres) can confine and support the transmission of several higher order modes. At a fixed wavelength, only microfibres with diameters that fall below certain values (normally smaller than the wavelength) can support single-mode guidance. However, this dimension criterion for single-mode guidance does not strictly hold for adiabatically tapered optical microfibres, where the coupling between the fundamental mode and higher order modes is negligible throughout the length of the tapered microfibre. Adiabatically tapered optical fibres even with relatively large diameters, due to the slow variation of diameter along the

transition region, support the propagation of the launched fundamental mode along the tapers. Therefore only the electric field distribution of the fundamental HE_{11} mode is considered here for mode field analysis, since all the tapered microfibres discussed in this thesis are adiabatic in nature. In this case, the solution for the Maxwell's equations can be expressed as [38]:

$$\left[\frac{J_1'(U)}{UJ_1(U)}+\frac{K_1'(W)}{WK_1(W)}\right]\left[\frac{J_1'(U)}{UJ_1(U)}+\frac{n_1^2K_1'(W)}{n_2^2WK_1(W)}\right]=\left(\frac{v\beta}{kn_1}\right)^2\left(\frac{V}{UW}\right)^4 \tag{2.1}$$

Where J_1 is Bessel function of the first kind and K_1 is the modified Bessel function of the second kind, $U=a\sqrt{k^2n_1^2-\beta^2}$, $W=a\sqrt{\beta^2-k^2n_2^2}$, a is the microfibre radius, $k=2\pi/\lambda$, n_1 and n_2 are the RIs of the microfibre and the surrounding medium respectively, β is the propagation constant and $V=\sqrt{U^2+W^2}$ is the normalized frequency.

Using a cylindrical coordinate system (r, θ, z), the electric field distributions for the HE_{11} modes are expressed as [6]:

$$E_r=\begin{cases}-\dfrac{a_1J_0\left(U\dfrac{r}{a}\right)+a_2J_2\left(U\dfrac{r}{a}\right)}{J_1(U)}\cdot f_1(\theta) & (0<r\le a)\\ -\dfrac{U}{W}\dfrac{a\ K_0\left(W\dfrac{r}{a}\right)-a_2K_2\left(W\dfrac{a}{r}\right)}{K_1(W)}\cdot f_1(\theta) & (a<r<\infty)\end{cases} \tag{2.2}$$

$$E_\theta=\begin{cases}-\dfrac{a_1J_0\left(U\dfrac{r}{a}\right)-a_2J_2\left(U\dfrac{r}{a}\right)}{J_1(U)}\cdot g_1(\theta) & (0<r\le a)\\ -\dfrac{U}{W}\dfrac{a\ K_0\left(W\dfrac{r}{a}\right)+a_2K_2\left(W\dfrac{a}{r}\right)}{K_1(W)}\cdot g_1(\theta) & (a<r<\infty)\end{cases} \tag{2.3}$$

$$E_z=\begin{cases}-\dfrac{iU}{a\beta}\dfrac{J_1\left(U\dfrac{r}{a}\right)}{J_1(U)}\cdot f_1(\theta) & (0<r\le a)\\ -\dfrac{iU}{a\beta}\dfrac{K_1\left(W\dfrac{r}{a}\right)}{K_1(W)}\cdot f_1(\theta) & (a<r<\infty)\end{cases} \tag{2.4}$$

where a is the microfibre radius,

$$a_1 = \frac{V}{2UW(b_1+b_2)} - \frac{1}{2} \quad , \quad a_2 = \frac{V}{2UW(b_1+b_2)} + \frac{1}{2}$$

$$b_1 = \frac{1}{2U}\left[\frac{J_0(U)}{J_1(U)} - \frac{J_2(U)}{J_1(U)}\right] \quad , \quad b_2 = \frac{1}{2U}\left[\frac{K_0(W)}{K_1(W)} - \frac{K_2(W)}{K_1(W)}\right]$$

$$f_1(\theta) = \sin(\theta) \quad , \quad g_1(\theta) = \cos(\theta)$$

As an example of the use of the analysis above, the electric field components of the HE_{11} mode at a 1550 nm wavelength were calculated using a model developed by Lee [39]. The electric field intensity $|E|^2 = |E_r|^2 + |E_\theta|^2 + |E_z|^2$ of a 2 μm diameter microfibre with air cladding is shown in Fig. 2.2 (a). It can be observed that a small portion of the light is guided as the evanescent field outside of the microfibre with a power discontinuity at the fibre surface. This evanescent field fades away within a distance of circa 500 nm from the microfibre surface.

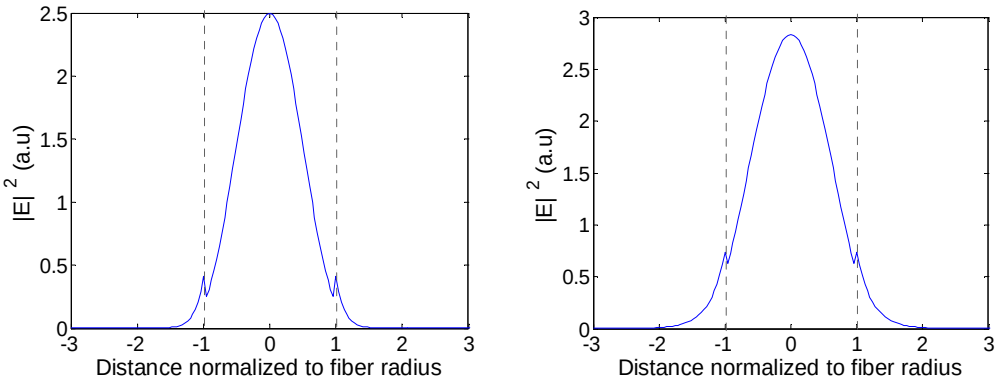

(a) (b)

Figure 2.2: Mode field intensity distribution for a microfibre with a diameter of 2 μm in (a) an air cladding and (b) a water cladding.

For many sensing applications, microfibres work in an aqueous environment. Thus as a second example, the electric field intensity for the same microfibre with a water cladding is shown in Fig. 2.2 (b). In comparison with the air-clad microfibre, the smaller RI difference between water and silica results in a weaker confinement of the guided modes. The electric field expands further outside the microfibre with a longer tail for the evanescent field (in the order of 1 μm).

The ratio of the power fraction in the microfibre to the total guided power is denoted as η and calculated as:

$$\eta = \frac{\int_0^a S_z dA}{\int_0^a S_z dA + \int_a^\infty S_z dA} \tag{2.5}$$

where S_z is the longitudinal component of Poynting vector and $dA = r \cdot dr \cdot d\theta$.

Fig. 2.3 shows the change of η with the microfibre diameter for both air-clad and water-clad situations calculated using the same model as demonstrated in [39]. A low value of η corresponds to a large evanescent field power. For microfibres with an air cladding, η starts to decrease when the microfibre diameter falls below circa 4.0 μm. As the diameter keeps reducing, η continues to decrease in a more drastic fashion. The power fraction of the evanescent field exceeds the power within the microfibre when the diameter drops to approximately 0.8 μm. In comparison, microfibres with water cladding show smaller values of η because the smaller RI contrast between water and silica results in a weaker mode confinement. To achieve a η < 1 requires a microfibre diameter of less than 6.5 μm diameter and η reaches 0.5 where the power in the evanescent field becomes dominant at a diameter of approximately 1.25 μm. In summary then, a microfibre shows a larger evanescent field fraction when surrounded by a water environment than by an air environment.

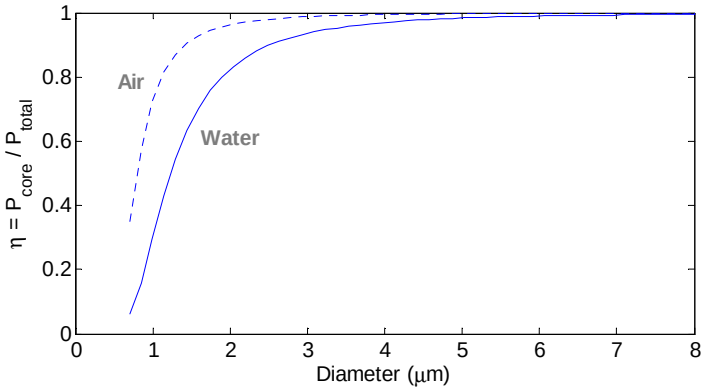

Figure 2.3: Fraction of the guided power in the microfibre vs. microfibre diameter. The dashed line and the solid line correspond to microfibres with an air cladding and with a water cladding respectively.

In general, the fraction of the evanescent field increases with decreasing microfibre diameter. Therefore microfibres with smaller diameters can facilitate stronger light-environment interactions and as a result higher sensitivities when engaged as sensors. However, overly thin microfibres (less than 1 μm typically) have poor mechanical strength, are less stable during measurements and additionally are very difficult to

handle. It is easier in practice to control the diameter of the microfibre to a manageable level while retaining to the greatest extent possible capacity of the microfibre to act as a sensing platform.

2.1.2 Microfibre fabrication

Tapered microfibres can be fabricated using the same method as fabricating conventional tapered fibres. A standard fibre tapering process can be described in a general sense as follows. The coating of a short section (3–4 centimetres) of an optical fibre is stripped off and the stripped fibre is cleaned. The fibre is pulled straight and the two ends (with cladding on) are fixed onto two translation stages. The bare fibre section is placed into/over a high-temperature heating source. The temperature should be high enough (usually over 1100 °C) to sufficiently soften the silica fibre into a viscoelastic state. Then the two translation stages slowly move outwards in the opposite directions to stretch the fibre and form it into a biconically tapered shape with the required diameters.

A fibre tapering setup as shown schematically in Fig. 2.4 (a) was developed to fabricate tapered microfibres used in this research. The setup adapted the microheater brushing technique demonstrated in [19].

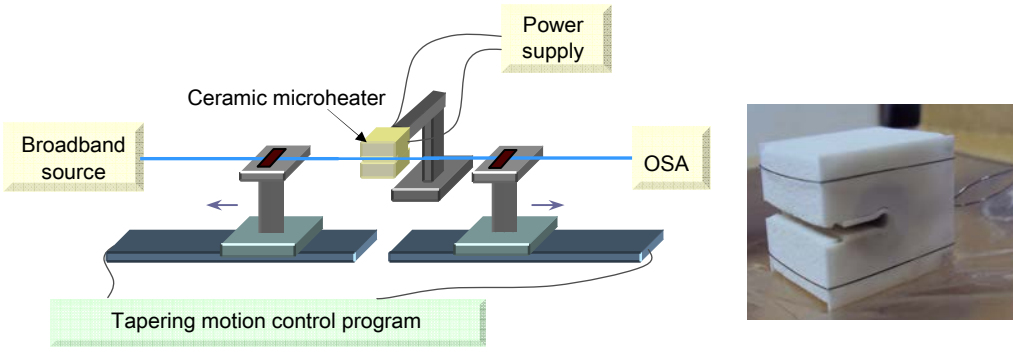

(a) (b)

Figure 2.4: (a) Schematic diagram of the microfibre fabrication setup built based on the microheater brushing technique. (b) A photo of the ceramic microheater.

The setup consists of two major parts:

- **Heating source.** A ceramic microheater (CMH-7019, NTT-AT), shown in a photo in Fig. 2.4 (b) was used to heat the optical fibre to approximately 1150 °C. Silica fibres

can reach a viscoelastic state around this temperature range which is suitable for tapering. The microheater was mounted on a 3-dimensional translation stage to precisely control the position of the microheater relative to the fibre. One factor that must be accounted for is that the temperature along the heat zone of the microheater is not uniform. The highest temperature occurs at the center and gradually drops towards the edges. For instance, when the measured temperature in the center reaches 1250 °C, the temperature at the edges only reaches 900 °C (Fig. 2.5). This quasi-Gaussian distribution of the temperature means that only a 1–2 mm heating zone at the center out of the 19 mm overall heating zone is realistically effective for fibre tapering. This 1–2 mm long heating zone is defined as microheater's effective heating zone and its length is L_{ehz}. The length of the microfibre uniform diameter waist region is assumed to be equal to L_{ehz} [40], where a simple single stretching pull of the fibre is employed. In order to fabricate microfibres with longer uniform waist regions, the effective heating zone can be extended by introducing a repeated brushing motion of the microheater into the tapering process [41]. The travel range of this repeated brushing motion is defined as microheater brushing length L_{brush}. Thus tapered microfibres with various lengths of the uniform waist region can be fabricated by varying the total effective heating length $L = L_{ehz} + L_{brush}$ (as shown in Fig. 2.5) by controlling the microheater brushing length L_{brush}.

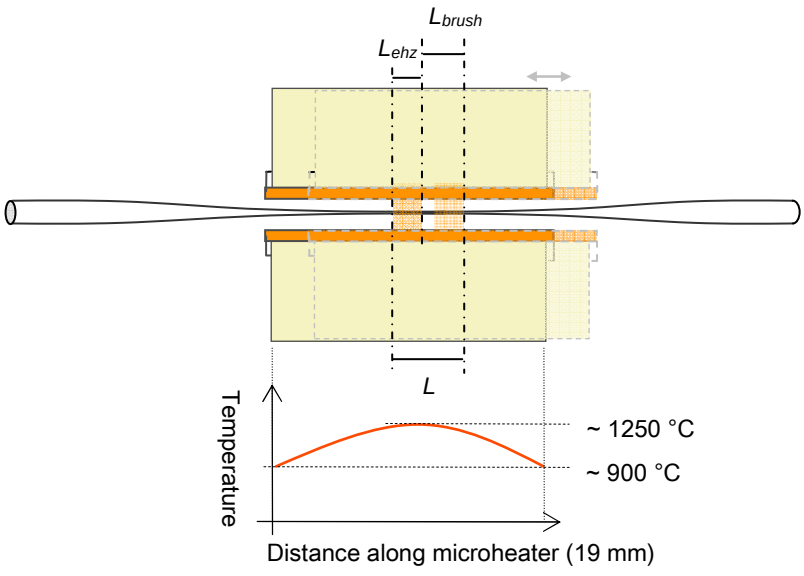

Figure 2.5: Schematic diagram of a microheater in brushing motion to illustrate the effective heating zone L_{ehz}, microheater brushing length L_{brush}, and the total effective heating length L. Temperature distribution along the heating slot of the microheater is also shown.

- **Pulling rigs**. Two precision controlled linear motorized translation motion stages (A-LSQ150B-E01, Zaber) were used to stretch the heated fibre. A tapering motion control program, written in C#, was developed to precisely control the tapering process. By setting parameters in the program such as original fibre diameter, required microfibre waist diameter, microheater brushing length etc., microfibres with a controllable profile for both the waist and the transition regions could be fabricated. In the actual tapering process, the two motorized translation stages not only perform the pulling motion but also the microheater brushing motion. It is possible to move the microheater to perform the brushing technique but this is more difficult in practice because of positioning instability and the potential safety hazards of actually moving the microheater itself. Instead the pulling and brushing motions were integrated in the following way. During tapering, the two motorized translation stages work together in a synchronous fashion to create an equivalent effect of a "brushing" microheater. At the same time, a small difference in translation speed (0.1 mm/s) was maintained between the two stages to elongate the fibre. However the term “microheater brushing length” is still used for consistency in this thesis.

The program for controlling the motions is based on the theory developed by Birks et al [40]. The model assumes the volume of the fibre to be constant during the tapering process. The length of the uniform waist region always equals the length of the softened fibre, which also equals the total effective heating length L which was defined earlier in Fig. 2.5. The following equation holds under these conditions [40]:

$$\frac{dr_w}{dx} = -\frac{r_w}{2L} \tag{2.6}$$

where r_w is the radius of the microfibre waist and x is the total elongation of the fibre after tapering. During fabrication, L can be kept constant or varing during the tapering process. A constant L value is used to fabricate tapers which have relatively shallow transition regions with a decaying-exponential profile. With a constant L and given an initial radius of the original fibre r_0, the final waist radius of the microfibre r_w is expressed as [40]:

$$r_w(x) = r_0 e^{\frac{-x}{2L}} \tag{2.7}$$

The profile of the transition region can be expressed as follows:

$$r(z) = r_0 e^{\frac{-z}{L}} \tag{2.8}$$

Microfibres with other types of transition region profiles can be fabricated by varying the heating length L with the taper elongation x in a real-time fashion during the tapering process. Details on calculating the waist radius and plotting the transition region profile for varying L can be found in ref. [40]. The research described in this thesis only considers microfibres with an exponentially decaying transition region profile fabricated using a constant L value. Tapers with such an exponentially decaying transition profile can be approximately considered to be adiabatic. In principle, fibre tapers are adiabatic if the transition profile meets the adiabaticity criteria described in [37]. Such optimal adiabatic tapers should be fabricated by varying the heating length L during the tapering process according to the relationship between L and x (taper elongation) demonstrated in [40]. However it was experimentally proved [42] that long tapers with an exponentially decaying profile are a very good approximation to being truly adiabatic with loss of less than 0.05dB.

It should be noted that discrepancies between the calculated and the actual diameters of the microfibres can occur in practice during fabrication. The temperature along the microheater slot where fibre is inserted in has a quasi-Gaussian profile as shown in Fig. 2.5. This temperature profile makes it difficult to estimate the exact length of the effective heat zone L_{ehz} of the microheater which in turn affects the total effective heating length L. Also the airflow in the lab can significantly influence the temperature profile of the microheater. A small variation in L can lead to large error in predicting r_w since r_w exponentially depends on L. Thus the determination of an appropriate value for L_{ehz} is critical for accurate prediction of the diameter of the fabricated microfibres. To do so, the actual diameters for a range of fabricated microfibres with different calculated diameters were first measured using a microscope. Then different values of L_{ehz} were tested until the discrepancy between the calculated and the actual diameters was minimized. The value of L_{ehz} which allowed the reduction of the error in predicting the diameter of the fabricated microfibres to less than 10% was determined to be 1.65 mm. The developed microfibre tapering setup and program were also used to fabricate OMCs used in this research. Further fabrication detail for OMCs is explained as required in Chapter 3.

2.2 Microfibre based sensing applications

Optical microfibres have a wide range of applications due to their ability to generate large evanescent fields which are readily accessible, the capability to form useful configurations with small losses to allow for the development of physically compact devices and the ability to tightly confine modes to the microfibre surface. Tong et al. [43] provided a comprehensive review of the recently developed microfibre based photonic applications in various fields such as near-filed optics, quantum optics, nonlinear optics, plasmonics, etc.

This section focuses on approaches to utilizing the near-field interactions between microfibres and their local environment as a means to underpin sensors. In this section several typical microfibre related structures reported in the literature to date that utilize tapered microfibres are reviewed, with a mention where appropriate of the sensing application involved. The structures covered in this review include:

1. single microfibres
2. microfibre based interferometers
3. microfibre based resonators
4. microfibre based couplers including optical microfibre couplers (OMC)
5. microfibre combined with non-fibre based resonance effects

Many of the sensors based on structures 1–4 above (with a particular emphasis on OMC) focus on utilizing phase-environment interactions for detection which correspond to the phase-sensitive approach mentioned in Chapter 1. Structure 5 on the other hand utilizes a microfibre's evanescent field to excite other resonance effects such as localized surface plasmon resonance (LSPR) for metallic nanoparticles, which corresponds to the non-fibre resonance approach mentioned in Chapter 1.

2.2.1 Single microfibre based sensors

Tapered microfibres can be divided into two categories: adiabatic and nonadiabatic. As briefly introduced previously in Section 2.1.1, a tapered microfibre can be defined as adiabatic for the fundamental mode, if the coupling between the fundamental mode and higher order modes is negligible throughout the length of the tapered microfibre. From

an intuitive perspective, the taper angles are so small (shallow) for an adiabatic taper that the propagating mode sees a straight fibre [44]. If the taper angle that exists along the transition regions of a tapered microfibre is large (abrupt) enough so the fundamental mode does not support propagation without coupling of power into higher order modes then such a microfibre can be considered as nonadiabatic for the fundamental mode.

(a) Adiabatically tapered microfibre based sensors

Microfibres with subwavelength scale diameters can generate evanescent fields that are easily accessible and strong enough for sensing in the intensity domain by detecting the intensity variation of the guided modes that results from local environmental changes. After Tong's demonstration of low-loss optical micro/nanofibres [32], several sensors were developed based on adiabatically tapered optical microfibres. For example, Polynkin et al. developed a RI sensor using a 700 nm diameter single microfibre for the detection of the RI of a liquid flowing through a microfluidic channel [45]. Due to the large evanescent fields, subwavelength optical micro/nanofibres are sensitive to small changes that occur locally on the fibre surface. Several biochemical sensors were developed using nanometre diameter optical fibres. These sensors can detect chemical compounds such as hydrogen [46] and sub-monolayers of 3,4,9,10-perylene-tetracarboxylic dianhydride molecules [47] as well as proteins such as bovine serum albumin (BSA) [48]. Although subwavelength micro/nanofibres can provide high sensitivity in detection, these ultra-thin fibres can suffer from poor mechanical strength and stability during experiments. Thus the applications of those sensors are most likely limited to specific situations, within for example a controlled laboratory environment.

(b) Nonadiabatically tapered microfibre based sensors

As mentioned earlier, mode coupling between the fundamental mode and the higher order modes occurs in nonadiabatic tapered fibres. As a result, the tapered fibres exhibit wavelength dependent transmission spectra that are sensitive to external RIs. Such nonadiabatic tapered fibres utilize phase-environment interactions and thus do not essentially require ultra-narrow subwavelength diameters for detection. This makes nonadiabatic tapered microfibre based sensors more robust and thus more suitable for a wider range of applications. The idea of using a nonadiabatic tapered fibres for sensing was first proposed by Cassidy et al. in 1985 [49]. Later Lacroix et al. carried out

extensive studies to elaborate the nonadiabaticity of the mode propagation and coupling in abrupt tapers in several papers [50][51][23][52]. In recent years, the potential of such nonadiabatically tapered optical fibres for biosensing applications has drawn researchers' attention. A wide variety of biosensors have been developed and a comprehensive review by Latifi et al. of the biosensors based on nonadiabatic tapered optical fibres can be found in [53]. In parallel to exploring new sensing applications, researchers have also been engaged in enhancing the detection sensitivity using nonadiabatic tapered optical fibres. For example in 2012, an ultra-high sensitivity RI sensor based on a nonadiabatic microfibre was proposed by Ji et al [54]. The sensor achieved a maximum sensitivity of 18681.82 nm/RIU for detecting a RI in the range of 1.3337–1.3700.

2.2.2 Microfibre based interferometers

Mach-Zehnder interferometers (MZI) and Michelson interferometers (MI) are widely used as the basis of sensors due to their phase sensitivity to local RI changes. By combining the advantages of optical microfibres with MZI or MI, high sensitivity sensors can be developed. Several microfibre based interferometric sensors have been proposed to date. For example, Lou et al. demonstrated for the first time in 2005 that the theoretical sensitivity of a microfibre MZI sensor is higher than that of a conventional MZI based on the use of integrated planar waveguides [55]. Subsequently an experimental realization of a microfibre based MZI RI sensor was achieved by Wo et al., which achieved a sensitivity of up to 7195 μm/RIU [56]. In order to make the interferometric structure simpler and more compact, MIs were fabricated within a single piece of optical fibre by creating an abrupt taper [57] or concatenating two abrupt tapers [58] within in the fibre. As a demonstration of a practical sensor, Chang et al. developed a liquid level sensor using an MZI fabricated by concatenating two strands of tapered fibres [59]. Inspired by the use of interference in well-known singlemode-multimode-singlemode (SMS) structures as a the basis of a range of sensors [60], Wang et al. developed a microfibre based RI sensor by tapering the multimode section of an SMS structure [61]. The sensitivity of such a tapered SMS structure was found to be higher than that of a conventional SMS structure.

2.2.3 Microfibre based gratings

By fabricating fibre Bragg gratings (FBG) within optical microfibres, the advantages of microfibres and FBGs can be combined to develop sensors with improved compactness and faster responses. Similar to conventional FBGs, microfibre FBGs can be fabricated by periodically modifying the RI along the microfibres. Typical techniques include inscription of photosensitive microfibres using ultraviolet (UV) lasers [62] or inscription of microfibres that are not photosensitive using femtosecond lasers [63]. FBGs can also be fabricated by direct precision milling on the surface of microfibres using focused ion beams [64]. Several microfibre FBG structures have been developed for use as RI sensors [62][63][64][65]. The diameters of the microfibres used in the literature ranged from 2 to 6 μm. In addition to RI sensors, a microfibre FBG temperature sensor [66] and a force sensor [67] have also been developed. Apart from FBGs that are written in microfibres, several sensors were also developed by concatenating an FBG written in a conventional fibre with a fibre taper to create a microfibre-FBG composite structure. An accelerometer [68] and a strain sensor [69] have been developed based on such configurations.

In addition to FBGs, long period gratings (LPG) can also be written in microfibres. Xuan et al. demonstrated a microfibre based LPG fabricated using a focused high frequency CO_2 laser [70]. Both the temperature and RI sensitivity of that microfibre LPG were investigated.

2.2.4 Microfibre based resonators

Due to the strong evanescent fields and the versatility of configuration, microfibres can be configured into a self-coupling loop or coil structure to form resonators with high quality factors (Q factors).

(a) Loop and knot resonators

A microfibre can be bent into a loop with sections of the microfibre parallel overlapping together to form a loop resonator (sometimes referred to as a ring resonator in literature) [71]. The schematic diagram of a typical microfibre loop resonator is shown in Fig. 2.6 [72]. Light can evanescently couple within the overlapped region and recirculate within the loop to generate a whispering gallery mode. The loop geometry is

mechanically maintained by the weak electrostatic force between the overlapped microfibre sections. The first microfibre loop resonator was proposed by Caspar and Bachus in 1989 by forming a loop using a 8.5 μm diameter tapered SMF [71]. Later Sumetsky et al. carried out work to both theoretically and experimentally investigate the optical properties of microfibre loop resonators that were formed by subwavelength diameter micro/nanofibres [73][74]. High Q factors of magnitudes of 10^5 were achieved with such microfibre loop resonators.

Figure 2.6: Schematic diagram of a microfibre loop resonator (taken from [70]).

The suitability of a microfibre loop resonator for RI sensing was first theoretically investigated by Shi et al. in 2007 [75]. The next year, experimental realization of such a RI sensor was achieved by Guo et al. using a microfibre loop resonator supported by a copper rod [76]. Since the loop geometry is only maintained by the weak electrostatic force between the overlapped sections of the microfibre, the mechanical stability of a bare loop structure is poor and thus applications are limited. To improve the mechanical stability of the loop structure, the overlapped sections were fused with a CO_2 laser in [77]. Alternatively a means to improve structure stability was achieved by embedding the structure in a low RI polymer [78][79].

Another approach to improving the mechanical stability as well as to ensure the close proximity of the overlapped fibre sections of the resonator is by modifying the loop structure into a knot to form a microfibre knot resonator [80]. Figure 2.7 shows the schematic diagram of a typical microfibre knot resonator [72]. Different from a loop resonator, the geometry of a knot resonator is maintained by the electrostatic force and the friction between the knotted sections of the microfibre.

Figure 2.6: Schematic diagram of a microfibre knot resonator (taken from [72]).

Since the first demonstration of a microfibre knot resonator in 2003 [32], a wide range of sensors have been developed. Examples include a temperature sensor [81], a humidity sensor [82], an accelerometer [83], a current sensor [84], a magnetic field sensor [85], an acoustic sensor [86], a solution concentration sensor [87] and a RI sensor [88].

(b) Coil resonators

Another important class of microfibre based resonators are microfibre coil resonators. A microfibre coil resonator is fabricated by tightly wrapping a microfibre around a central rod to form a coil. A schematic diagram of a microfibre coil resonator is shown in Fig. 2.7 [89]. Light can evanescently couple between the adjacent turns and recirculate within the coil to achieve a high Q resonance. Such a coil resonator can achieve in theory a Q factor in the order of 10^9 which is much higher than that of a loop or a knot resonator [89].

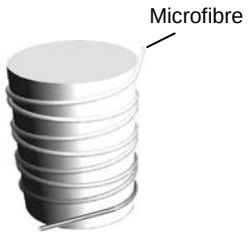

Figure 2.7: Schematic diagram of a microfibre coil resonator (adapted from [89]).

Following the demonstration and theoretical investigation of a microfibre coil resonator by Sumetsky et al. [89][90], Xu et al. carried out series of studies to optimize the theoretical design [91][92], to fabricate and package the structure [93][94], and to develop a RI sensor [95] using microfibre coil resonators. The authors also suggested the potential for such a structure to work as a biosensor. Later Yung et al. from the same research group improved the fabrication and packaging technique used for the microfibre coil resonator and experimentally achieved a Q factor of 10^6 [96]. Following Xu and Jung's work, Ismaeel et al. recently demonstrated a new type of microfibre coil resonator which combines a microfibre coupler and a coil resonator [97]. The structure was formed by coiling a microfibre coupler around a central rod. The mode coupling within the microfibre coupler together with the resonance of the coil resonator resulted in an increased extinction ratio of the resonance spectra which could facilitate sensing with improved performance.

2.2.5 Optical microfibre couplers

As introduced in Chapter 1, an OMC is an efficient microfibre structure which has great potential for sensing applications and is one of the structures that the research reported in this thesis focuses on. An OMC is fabricated by laterally fusing two SMFs and tapering them down to a diameter close to the scale of a microfibre. Unlike a microfibre where the environment influences a single evanescent field, an OMC used as a sensor relies on the environment influencing on the coupling between two evanescent fields. The fabrication of an OMC is also relatively simple and straightforward compared with other microfibre based phase-sensitive sensors such as resonators and interferometers. The coupler structure is formed by fusing which occurs during the fibre tapering process and does not require complex post-tapering manipulations of the microfibres to form the necessary structures.

The OMC is a structure that is an adaptation of a conventional fused optical fibre coupler. Conventional fibre couplers were originally designed to function in optical communications systems for routing, splitting and combining signals. The coupler's wavelength sensitive coupling behaviour was also utilized in wavelength-division multiplexing for various photonic devices such as optical switches and filters [98]. The potential for the application of conventional fibre couplers in sensing was demonstrated by several research groups. Fornel et al. measured the dependence of a single-mode fused tapered coupler on the RI of the surrounding medium [99]. The sensitivity was limited but the potential for developing efficient sensors using couplers with higher taper ratios was recognized. Lamont et al. studied the RI dependences of single-mode fused tapered couplers with various degrees of fusion and waist diameters [100]. Subsequently in 2007, Tazawa et al. developed a biosensor using a 9 μm diameter tapered fibre coupler [101], in which the ability of the coupler to detect proteins using an avidin-biotin interaction was demonstrated.

After Tong's demonstration of low-loss subwavelength diameter optical fibres [32], research interest in the area of fibre couplers was drawn to fibres with smaller diameters. In 2009, Jung et al. proposed for the first time an OMC with a diameter close to the wavelength of the transmitted light [9]. In that paper, the authors used an OMC with a waist diameter of 1.5 μm to achieve single-mode operation in a broad wavelength region of 400–1700 nm. The use of such close-to-wavelength diameter fibres in a coupler structure for sensing applications is attractive because of the large evanescent

fields and mode coupling possible. Following Jung's work, Wang et al. proposed a potential high temperature sensor using OMCs with waist diameters around 2 μm [11]. By cleaving a full OMC at the waist region to form an OMC tip probe (as shown in Fig. 2.8 [102]), the compactness and spatial resolution of the sensor can be further improved. Such an OMC tip temperature sensor was demonstrated by Ding et al [102]. The sensor could measure temperature up to 1280 °C with a sensitivity of 11.96 pm/°C. Due to the minimal size and high sensitivity of the OMC structure, sensors aiming at detecting small-scale measurands were also developed. For example, a biosensor for DNA detection based on an OMC was proposed by Ismaeel et al [103]. Very recently, Chen et al. developed a micro-force sensor using an OMC with a 1.6 μm diameter OMC [104]. A sensitivity of circa 3754 nm/N was achieved to measure forces with magnitudes as low as 10^{-4} N.

Figure 2.8: Schematic diagram of an OMC tip probe (adapted from [101]).

The OMCs introduced above were all fabricated by fusing and tapering two standard SMFs together. Another approach to fabricate OMCs is by fusing two pre-narrowed microfibres together using a CO_2 laser [105]. If the diameters of the fibres are very small, a coupler can be formed by simply positioning two freestanding micro/nanofibres in close proximity with each other, using electrostatic forces between the micro/nanofibres to achieve contact between the fibres. Such a micro-coupler was demonstrated by Tong et al [106]. Liao et al. fabricated a similar micro-coupler by twisting two microfibres together [107]. The authors used the twisted coupler as a RI sensor and achieved a sensitivity of 2735 nm/RIU. In general, these type of micro-couplers can have extra advantages compared with fused OMCs. For example, where the fibres used are drawn microfibres, the overall length of the coupler can be significantly reduced since the coupling length of such a micro-coupler does not need to incorporate transition regions. In addition, the coupling coefficient can be tuned by varying the coupling angle between the two micro/nanofibres. However the micro-couplers have a significant disadvantage that they require "micro-manipulation" of the micro/nanofibres to form the necessary structure. Thus the accuracy and repeatability of the fabrication is more critical.

2.2.6 Microfibres combined with non-fibre based resonance effects

Tapered optical microfibres are widely used as intrinsic sensors. They also often work as light coupling agents given their large evanescent fields for efficient coupling, and utilizing the original fibre ends for easy and low-loss optical connections. By placing an optical microfibre in close proximity with another optical microstructure, light can be launched into and collected from the structure to facilitate the generation of other optical effects.

a) Microfibres combined with WGM resonators

One example of such an approach is the use of tapered microfibres as a delivery and coupling waveguide to couple an evanescent field into and out of various microcavities for the generation of WGMs. Light is confined within the microcavities due to total internal reflection and achieves a state of resonance at certain wavelengths. Typical WGM microcavities used within this approach include silica microspheres [108], microcapillaries [109], microdisks [110] and microtoroids [36]. The generated WGM is usually characterized by high Q-factor resonances visible in measured spectra. Such resonances can be extremely sensitive to small particles adsorbed onto the surface of the microcavities. Thus such optical micro-resonators have the potential for developing biosensors which can not only provide information about the affinity and concentration but also about the size and shape of the analyte [108].

b) Microfibres combined with LSPR

Another example of microfibre facilitated resonators is associated with the use of microfibres to couple light into conductive nanoparticles for the generation of LSPR. This is another structure that the research reported in this thesis focuses on in addition to the OMC structure discussed previously. LSPR is a collective electron oscillation in conductive nanoparticles caused by incident light waves [111]. Light incident on the nanoparticles induces conduction electrons to oscillate collectively at a resonant frequency. This resonance frequency depends on the nanoparticles' size, shape, composition, interparticle distance and dielectric properties [112]. By immobilizing nanoparticles onto the surface of a tapered microfibre, the evanescent field guided along the microfibre can be coupled to the LSPR around the nanoparticles. The coupled LSPR shows a strong intensity and a very short decay distance of typically 5–30 nm [8].

Biomolecules trapped on the nanoparticles' surface can interact with this LSPR and in turn efficiently modify the light transmission and the detected signal.

Chemically etched optical fibres and cleaved fibre ends were used in some early work to get access to the evanescent fields and in turn facilitate LSPR sensors [113][114][115][116][117]. However chemical etching can result in surface roughness and the diameters of the etched fibres are difficult to control. Given the advantages of tapered optical microfibres, as introduced in Chapter 1, several LSPR sensors were developed by immobilizing gold or silver nanoparticles onto the surface of the tapered microfibres. The first work on immobilizing nanoparticles onto the surface of tapered optical microfibres to generate LSPR was carried out by Cui et al. in 2011 [7]. The effect of the size of the gold nanoparticles on the performance of the LSPR based tapered optical microfibre sensor was investigated in that paper. It was found that the sensor with larger size nanoparticles exhibited higher sensitivities in detecting RI changes in the local environment. The next year, Lin et al. developed a LSPR based RI and biochemical sensor by incorporating gold nanoparticles on the surface of a 48 μm diameter tapered fibre [14]. The resonance wavelength and the transmission intensity were shown to vary linearly with the local RI changes. Very recently in 2014, Li et al. proposed a sensor for cancer diagnostics by immobilizing gold nanoparticles onto the surface of a 1 μm diameter tapered microfibre [13]. A detection limit of 0.2 ng/ml was achieved in the detection of alpha-fetoprotein in a phosphate-buffered saline (PBS) solution. Apart form spherical nanoparticles, nanoparticles in other shapes were also studied in conjunction with microfibres. For example, Zhang et al. compared the effect of two chemical solvents used for immobilizing star-shaped gold nanoparticles onto the surface of tapered optical fibres[118].

Table 1.1 compares the microfibre based structures reviewed in this section and lists their key advantages and limitations when used for sensor development.

Table 1. 1: Comparison of microfibre based structures for sensing applications.

Microfibre structure	Advantage	Limitation
Adiabatic single tapered microfibre	• Simplicity of structure • Easy to fabricate	• Requires subwavelength diameter to achieve effective light-environment interaction • Unsuitable for wavelength domain interrogation

Nonadiabatic single tapered microfibre	• Relatively large and thus easily manageable fibre diameter • Short transition region for higher compactness	• Requires precise control of taper shape to achieve mode interference • Limited extinction ratio in transmission spectrum
Microfibre based interferometer	• High RI sensitivity	• Requires two light paths which can increase setup complexity and limit device miniaturization
Microfibre based gratings	• High strain and temperature sensitivity • Relatively high mechanical stability of the structure	• Grating inscription is complex and expensive • Limited RI sensitivity
Microfibre based resonators	• High Q-factor resonance for potential high sensitivity	• Complex manipulation of microfibre to form the structure • Low reproducibility
Optical microfibre coupler	• High RI sensitivity • Easy and inexpensive one-step fabrication	• Straight structure with limited lengthwise compactness
Microfibre combined with WGM	• High Q-factor resonance for high biosensitivity	• Requires precise alignment between the microfibre and the WGM cavity
Microfibre combined with LSPR	• Low-cost fabrication • Suitable for biosensing due to lack of bulk effects of LSPR • Easy biofunctionality of nanoparticles	• Require surface modification of microfibre for immobilizing nanoparticles

In general, most of the microfibre based sensors reviewed and described in this thesis are based on the detection of RI changes either in the surrounding environment or of the microfibre itself. Such RI based sensing structures can provide solutions for a wide variety of applications such as many biosensors, chemical sensors, gas sensors, humidity sensors, temperature sensors etc.

2.3 Summary

The theoretical analysis presented in this chapter has shown that optical microfibres can guide a substantially large fraction of the light outside of the microfibre as an evanescent

field. The power fraction and decay distance of the evanescent field depends on the fibre diameter and the index contrast between the microfibre and the surrounding medium. Such a mode intensity profile means that microfibres offer great potential for developing a range of fibre optic sensors.

Fabricating optical microfibres using ceramic microheater heating and tapering method offers a flexible fabrication method allowing for the control of the shape and diameter of the tapered microfibres with the advantages of ease of fabrication and low loss connections with other optical fibre components.

To date various photonic devices based on optical microfibres have been developed for a wide range of sensing applications. Sensors developed using microfibre based interferometers, gratings, resonators and couplers were reviewed in this chapter. Optical microfibre couplers were shown to have the potential to form a basis to develop high sensitivity RI sensors and biochemical sensors, due to the OMCs' highly environment-dependent coupling behaviour, as well as the ease of fabrication and handling. Optical microfibres can also be used as light coupling waveguides to facilitate WGM and LSPR sensors. Incorporating nanoparticles onto microfibres' surfaces allows for the development of microfibre based LSPR sensors with enhanced sensitivities.

Chapter 3

Optical Microfibre Couplers for Sensing

Research on conventional fused optical fibre couplers has shown that by reducing the diameter of such couplers to increase the evanescent fields and thus to support stronger light-environment interactions, such couplers can be used as sensors (as introduced in Section 2.4.5). Recent demonstrations by a variety of authors on the fabrication of 1–3 μm diameter optical microfibre couplers (OMCs) and their applications for high temperature sensing [11][102] confirmed the feasibility of developing OMC based sensors for a range of sensing applications in real world. This chapter explores the potential of OMCs for biosensing. Initially this chapter focuses on explaining the principles of operation of an OMC, on the fabrication of an OMC and on preliminary spectral results used to verify that the fabrication process was delivering useful OMC samples. The chapter then goes on to describe the development of an RI sensor using an OMC with a diameter of 2 μm (the diameter of each microfibre). The chapter also explores the polarization effects, temperature dependency, and humidity dependency of OMC based devices. The proposed OMC sensor can work as a high sensitivity refractometer but importantly can also underpin sensors for a variety of other measurands that rely on the measurement of local RI as an operating principle.

3.1 Principles of operation for OMC sensors

An OMC has a structure very similar to that of a conventional fused optical fibre coupler, which has been originally developed at the end of the 1970s [119][120]. The main

difference between the two structures is that compared with a conventional fibre coupler, an OMC has a much smaller diameter, usually of a few micrometres. Due to the small diameters and the resultant evanescent fields, OMCs are sensitive to local environmental changes and thus have strong potential to be used to develop sensors.

The structure of a typical tapered fibre OMC is shown in Fig. 3.1. The OMC consists of two identical microfibres with the entire waist region and part of the transition regions fused together. Light launched into one input port can be coupled and split between two output ports.

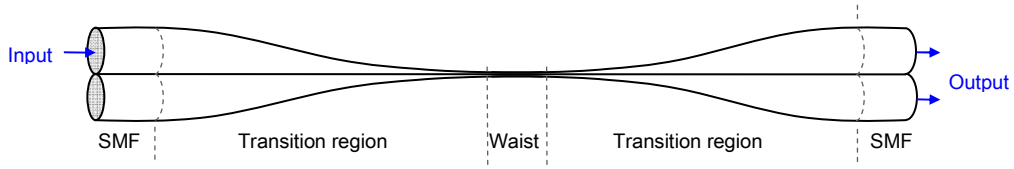

Figure 3.1: Schematic diagram of an OMC consisting of two fused microfibres with a uniform waist region and two transition regions.

Depending on the taper fabrication temperature [121], various degrees of fusion can be achieved between the microfibres within the OMCs [122][123]. For weakly fused OMCs, both fused microfibres roughly maintain their original cross-section geometry throughout the entire tapering process. Thus such OMCs have a dumbbell-shaped cross section. In this case, the aspect ratio, which is defined as the ratio between the total width and the height of the cross section at the OMC waist region, is usually larger than 1.8 [121]. For strongly fused OMCs, the cross-section geometry is altered in a way that the distance between the two microfibre axes reduces faster than the decrease of the fibre diameters. The resulting OMC can have a cross section with an elliptical or a circular shape [123]. The aspect ratios for such strongly fused OMCs can vary between 1.0 and 1.8. Compared with weakly fused OMCs, strongly fused OMCs require shorter coupling lengths and less critical diameters in order to achieve a complete power transfer from one fused fibre to the other. In addition, strongly fused OMCs also show weaker dependence on polarization and surrounding RI changes. Therefore strongly fused OMCs are more suited to work as beam combiners and splitters for optical fibre communications. In contrast, weakly fused couplers show a stronger dependency on surrounding RIs than the strongly fused ones [10] and are better suited to work as sensing elements. Therefore only weakly fused OMCs were fabricated and studied in this thesis.

In the light of the discussion on tapered microfibres presented in Section 2.1, the waist region of an OMC plays the key role in the coupling process due to the large evanescent field resulting from its narrow diameter. To understand the coupling behaviour of an OMC, an acceptable simplification is to consider two identical cylindrical silica waveguides with a uniform shape and homogenous RI profile fused together. The schematic of such a simplified OMC is shown in Fig. 3.2 (a). Optical properties of such symmetric directional couplers have been extensively investigated [124][125]. Coupled mode theory is commonly used for the theoretical analysis of light interactions between two fused fibres [126]. The theory assumes that the two single-mode microfibres work together as a composite system to support the propagation of an even mode and an odd mode. Light launched into one microfibre may be considered as a linear combination of the even and the odd modes. The superposition of the two modes, which have different propagation constants, results in a periodic interchange of guided power between the two adjacent microfibres [11].

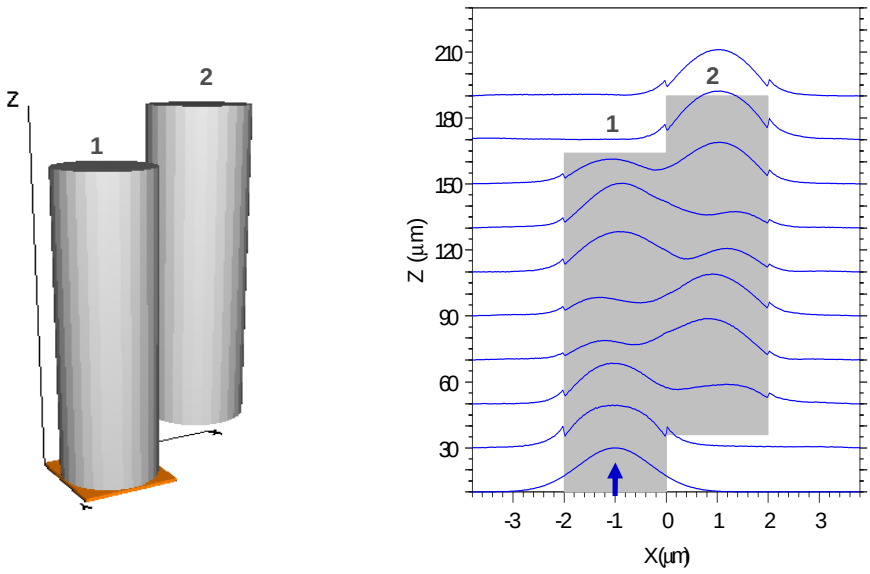

(a) (b)

Figure 3.2: (a) An OMC can be simplified to two adjacent cylindrical silica waveguides with uniform shape and homogenous RI profile. (b) Periodic light power interchange between the two microfibres as a result of the even-odd mode superposition.

An example of the electric field development along the direction of propagation for the electric field in an OMC with air cladding is shown in Fig. 3.2 (b) and was calculated using the commercial RSoft software (BeamPROP module). The diameter for each microfibre was assumed to be 2 μm and the RIs of the OMC and the surrounding medium

are 1.45 and 1.0 respectively. The wavelength used was 1550 nm. In Fig. 3.2 (b) transfer of energy (represented by the electric field intensity) between fibre 1 and fibre 2 is evident. It is also evident that over the length of this simplified OMC that the transfer reverses and energy is transferred back from fibre 2 to fibre 1 and so on, illustrating the periodic nature of coupling.

The coupling coefficient of a weakly fused OMC can be approximately denoted as [127]:

$$C(\lambda) = \frac{\pi\sqrt{n_1^{\,2} - n_2^{\,2}}}{2an_1} e^{-2.3026(A+B\tau+C\tau^2)} \tag{4.1}$$

$$\begin{array}{llll} A = a_1 + a_2V + a_3V^2 & a_1 = 2.2926 & a_2 = -1.591 & a_3 = -0.1668 \\ B = b_1 + b_2V + b_3V^2 & b_1 = -0.3374 & b_2 = 0.5321 & b_3 = -0.0066 \\ C = c_1 + c_2V + c_3V^2 & c_1 = -0.0076 & c_2 = -0.0028 & c_3 = 0.0004 \end{array}$$

where λ is the wavelength, n_1 and n_2 are the RIs of the silica fibre and the surrounding medium, a is the radius of the microfibre, $\tau = d/a$ is the aspect ratio of the cross section of the OMC, d is the distance between the axes of the fused microfibres, a is the radius of the microfibre and V is the normalized frequency where $V = [(2\pi a)/\lambda] \cdot \left(n_1^{\,2} - n_2^{\,2}\right)^{1/2}$. The output powers of the throughput port and the coupled port of the OMC are:

$$\begin{aligned} P_1(\lambda) &= P_0 \sin^2(CL_{eff}) \\ P_2(\lambda) &= P_0 \cos^2(CL_{eff}) \end{aligned} \tag{4.2}$$

where P_0 is the input power and P_1 *and* P_2 are the output powers of the throughput port and the coupled port respectively, and L_{eff} is the coupling length.

A model using Matlab was built based on Equation 4.1 and 4.2 to plot the transmission spectra of the OMC and to predict the sensitivity of the OMC sensor in detecting RI changes in the surrounding medium. The RI of the silica microfibre used in the model is 1.45. The OMC has a radius of 1.25 μm and a coupling length of 2 mm. The aspect ratio τ is chosen to be 2 for a weakly fused coupler (as explained in the lower section on Page 32). Examples of transmission spectra for the OMC with various surrounding RIs were calculated and are shown in Fig. 3.3 (a). The transmission spectra in the figure are normalized to the maximum intensity calculated at the wavelength of 1536 nm when RI is 1.349. From the figure, it is clear that an increase in the surrounding RI varies the

coupling coefficient C (according to Equation 4.1). Due to the $\sin^2$ (or $\cos^2$) dependence of the output power on C (according to Equation 4.2), the resulting output power variation manifests itself, in the wavelength domain, as a minimum intensity wavelength shift (referred to as dip wavelength shift in this thesis) of the transmission spectrum. The relationship between the surrounding RI and the dip wavelength shift is shown in Fig. 3.3 (b). An increase in the surrounding RI causes a significant blueshift of the OMC spectrum. The shifts are linear for the RI range between 1.334 and circa 1.359 and the shifts are nonlinear for the RI range above 1.360. However, the OMC based sensors demonstrated in the subsequent chapters in this thesis work mainly within the linear RI range. The calculated result shows that the sensitivity of an OMC based sensor can be expected to achieve circa 4200 nm/RIU within this linear RI range between 1.334 and 1.356. The average sensitivity of the sensor over the entire calculated RI range between 1.334 and 1.380 is 2609 nm/RIU.

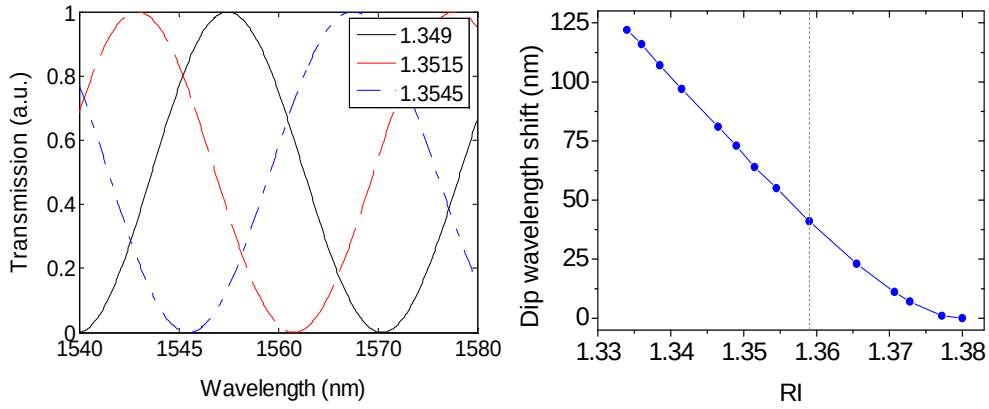

Figure 3.3: (a) Calculated spectral responses of the OMC in different RI media. (b) Calculated dip wavelength shift vs. the surrounding medium RI.

3.2 OMC fabrication

An OMC was fabricated using the same fibre tapering setup described in Chapter 2. The coatings of two standard single-mode optical fibres (SMF-28, Corning) were stripped for 4 cm long sections of the fibres respectively. The two bare fibre sections were placed in close proximity before being fixed onto the linear motorized translation stages. The fibres were also moderately twisted together, as shown in Fig. 3.4, to ensure the fibres remained in contact during fabrication. The same tapering motion control program used

for tapering single microfibres was used for the fabrication of OMCs. The temperature of the ceramic microheater was set to circa 1300 °C to ensure weak fusion of the fibres.

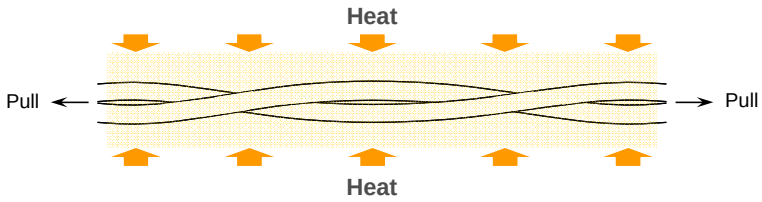

Figure 3.4: Two fibres are slightly twisted together to ensure close proximity between them during the fusing and tapering process.

As an example, the fabricated OMC sample has a total length of 29 mm, which consists of an approximately 2–3 mm long uniform waist region between two 13 mm long transition regions. The geometry and surface morphology of this OMC was examined under a field-emission scanning electron microscope (FE-SEM) (SU6600, Hitachi). An FE-SEM image of a short section of the OMC waist region is shown in Fig. 3.5. The image was taken with a magnification of 2000x. The diameter for each fused microfibre is approximately 2 μm giving a total width (or referred to as a total diameter in some literature) of 4 μm for the OMC. The inset shows a cross section of an OMC cleaved at the waist region observed under an optical microscope. The aspect ratio of the cross section (b/a) is measured to be 1.94, which confirms the weakly fused status of the fabricated OMC. Since the fabricated OMCs are weakly fused this means the two fused microfibres maintain the circular cross section shape throughout the entire tapering and fusing process (as explained previously in Section 3.1). Thus the model, described in Chapter 2, used to predict the shape and diameter of single tapers also applies to the case of OMC fabrication.

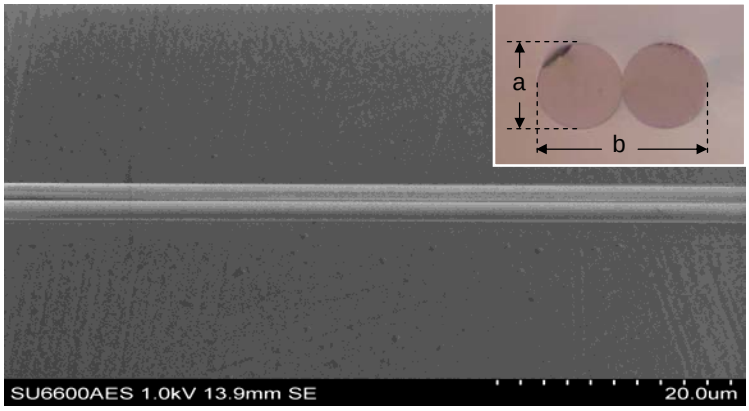

Figure 3.5: FE-SEM image of the waist region of an OMC taken at a magnification of 2000x. The diameter of each fused microfibre is circa 2 μm. The weakly fused status of the OMC is confirmed by the cross section image (as shown in the inset) observed under an optical microscope.

The output spectra for both the throughput port and the coupled port of a fabricated OMC sample were measured using an optical spectrum analyzer and the corresponding spectra are shown in Fig. 3.6. The spectra (for either throughput or coupled port) display a series of peaks due to the mode coupling over the taper length. The free spectral range (FSR), which is defined as the difference in wavelengths between the two consecutive spectral dips, depends on the waist diameter, the coupling length of the OMC and on the aspect ratio. Smaller diameters and longer coupling lengths result in smaller FSRs [127].

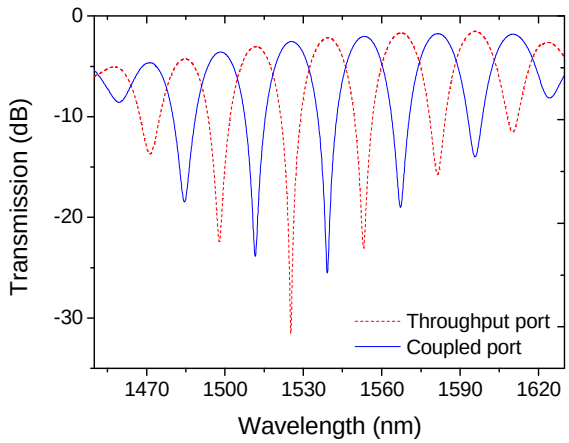

Figure 3.6: Output spectra for both the throughput port and the coupled port of a fabricated OMC sample.

3.3 RI sensing

In various microfibre based sensing applications, the detection of the analyte relies on the detection of the RI changes in the local environment. To verify the feasibility of using an OMC structure as a sensor, the sensitivity of the OMC to detect RI changes in the local environment was investigated experimentally.

The experimental details are as follows. A series of 14 liquid samples with various RIs were prepared by dissolving dimethyl sulfoxide in water with different concentrations. The 14 solutions had RIs ranged from 1.3340 to 1.3800 with an interval of circa 0.003 and were calibrated with a commercial refractometer (ABBE5, Bellingham+Stanley). For each liquid sample the entire coupling region of the OMC was covered with the solution and the transmission spectrum was measured. Each liquid sample was placed as a drop around the coupling region to create a surrounding medium with a defined RI. A schematic of the RI immersion setup is shown in Fig. 3.7. As shown in the figure, the OMC was placed on a polytetrafluoroethylene (PTFE) (Teflon) flat panel which has a relatively low RI of circa 1.35 since materials with a high RI will absorb the transmitted light due to the relatively large evanescent fields of the microfibres.

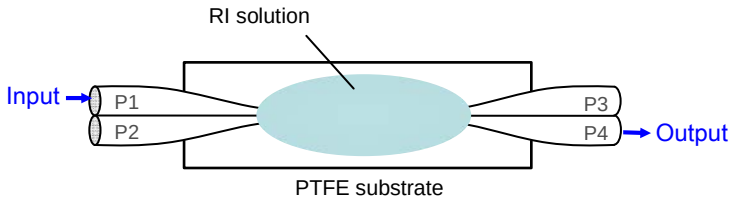

Figure 3.7: Schematic diagram of the RI immersion setup.

Figure 3.8 (a) shows the measured spectral responses of the OMC for three surrounding medium RI values used in the previous calculations shown in Fig. 3.3 (a). The experimental results show a good match with the calculated results in Fig. 3.3 (b). When the external RI increases, the selected dip wavelength of the spectrum experiences a blue shift within the measured RI range. The experimental and the calculated results for the relationship between the wavelength shift and the surrounding medium RI are compared in Fig. 3.8 (b). The experimental results show that the fabricated sensor has an average sensitivity of circa 2723 nm/RIU over the entire measured RI range from 1.3340 to 1.3800. Furthermore a high sensitivity of 4155 nm/RIU is obtained for the RI range from 1.3340 to 1.3515.

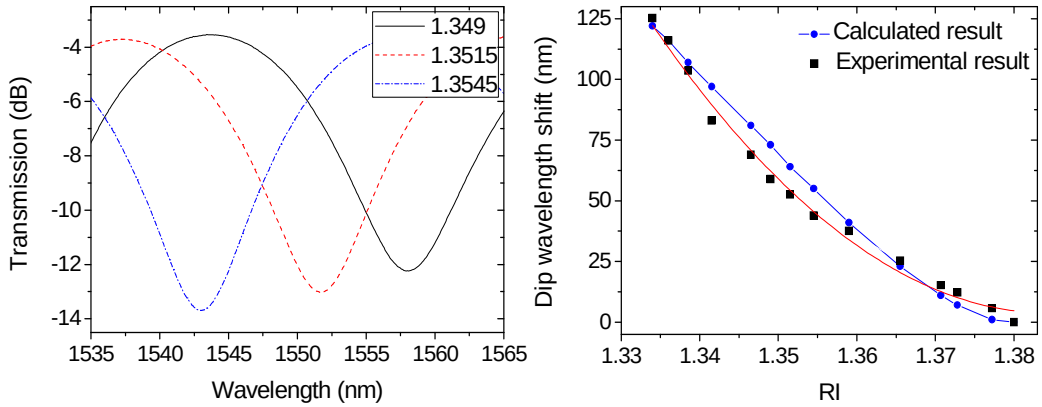

(a) (b)

Figure 3.8: (a) Examples of spectral responses of the OMC surrounded by liquid samples with different RIs (1.3490, 1.3515 and 1.3545). (b) Dip wavelength shift vs. RI changes in the surrounding medium.

It can also be seen from Fig. 3.8 (b) that the measured result is in a good agreement with the calculated result with a maximum deviation of approximately 12.8 nm. The perceptible discrepancy between the experimental and theoretical results may be caused by (1) the limitation of the theoretical model which has only considered the coupling between two parallel fibres with a uniform diameter and an ideal cylindrical shape. However the fabricated OMC has a considerable transition region length in the shape of a taper, and in reality the fibres are not strictly parallel; (2) as illustrated in Fig. 3.7 the mechanical stability of the OMC may be disturbed by the applying and removing the solutions during the measurements; (3) temperature effects may also play a role since the RI of the solution is temperature dependent; (4) finally, there is limit to the dimensional accuracy of the achieved diameter of the fabricated OMC.

3.4 Polarization effects

Polarization effects have a significant influence on the performance of optical fibre devices, particularly fibre optic sensors, and are frequently a key limitation of many optical fibre sensors. It is well known that the light coupling of conventional fused fibre couplers can be significantly influenced by changes in the polarization state of the input light [128]. Due to the structural similarity between conventional fused couplers and the OMCs, it is reasonable to assume that OMCs should inherit the polarization properties of the conventional fused fibre couplers. A frequent source of polarization state changes for

input light is also common to both OMCs and conventional optical fibre couplers. Specifically where standard single mode fibres are used to interconnect to the coupler, any perturbation by external mechanical stress of the interconnecting input fibre can change the polarization state of the light entering the coupler [129]. The coupling behaviour of an OMC can be influenced by the polarization state of the input light due to the difference in the coupling coefficients of the two orthogonal polarized modes [122]. Overall therefore it is necessary to experimentally study the polarization dependency of an OMC device in order to ensure that sensing accuracy is not compromised.

The polarization effect on the transmission spectra of an OMC was studied. The OMC had the same geometry (as shown in Fig. 3.5) as the one used for RI sensing in the previous section. The schematic of the experimental setup is shown in Fig. 3.9. Light from a broadband source (BBS) (SLD-6597, COVEGA) covering the wavelength range from 1450 to 1630 nm was launched into port P1. A manual linear polarizer (FB51, Thorlabs) was placed in between the light source and the OMC to manipulate the angle of linear polarization of the input light. The output light from port P4 was analyzed using an optical spectrum analyzer (OSA) (Q8384, ADVANTEST). The linear polarization state of the input signal was rotated from 0° to 90° with interval steps of 15°.

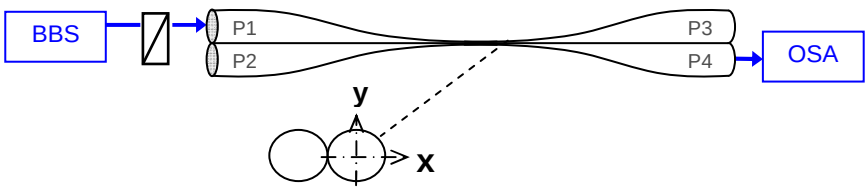

Figure 3.9: Schematic diagram of the setup for the study of the polarization effects of the OMC sensor.

The transmission spectrum corresponding to each linear input polarization state was recorded and shown in Fig. 3.10 (a). By rotating the polarizer from 0º to 90º the input light changed from x-polarized to y-polarized (Fig. 3.9). It is found that the resulting transmission spectra experienced variations in both free spectral range (FSR) and extinction ratio. Due to the variation in both the intensity domain and the wavelength domain, the spectra exhibit repeatable wavelength dependent change as the polarization state changes. For example, the spectra show significant peak wavelength shifts and in turn intensity variations around 1550 nm (wavelength range A). In comparison, the variations become much less prominent around 1615 nm (wavelength range B).

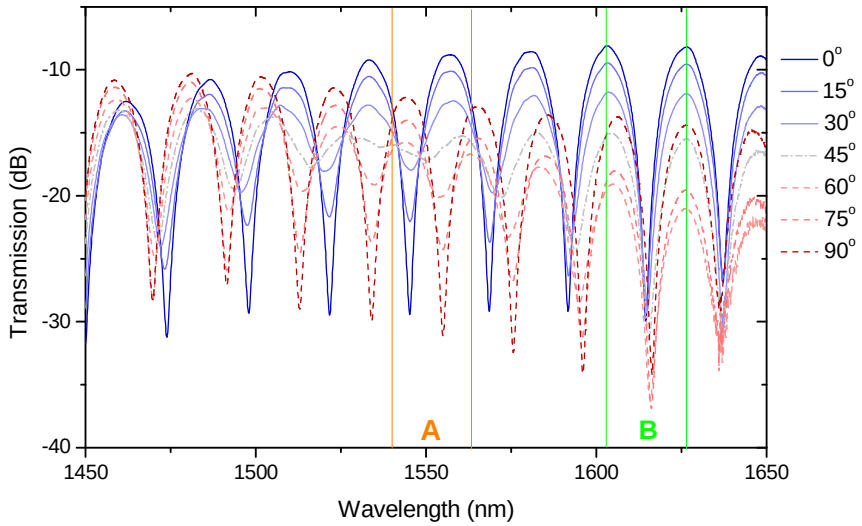

Figure 3.10: Output spectra of the OMC with various input linear polarization states.

One of the objectives of this research was to develop OMC based wavelength-domain sensors which could be interrogated by detecting peak wavelength shifts in the transmission spectra. This is because wavelength domain sensors show several advantages compared with pure intensity-domain sensors. Specifically, an intensity domain sensor which works by detecting the variations in the output intensity only in response to a measurand of interest can be easily affected by random power fluctuations in the system, for example due to optical source power fluctuations. In comparison, a wavelength-domain sensor which works by detecting wavelength shifts of the transmitted spectrum and is relatively immune to power variations, and thus can potentially offer a higher sensing stability.

Figure 3.10 demonstrates that changes in the polarization of the input light is another source of instability in a sensing system both in the case of intensity and wavelength domain interrogation. However, given the focus of this research on wavelength domain interrogation, it is particularly important to investigate the polarization induced peak wavelength shifts. It is also worth paying attention to how polarization may affect the spectral extinction ratio. Larger extinction ratios associated with sharper spectral peaks provide higher detection resolutions and thus are preferred in sensor design. Both the extinction ratio variations and the dip wavelength shifts caused by the changes in the polarization state of the input light for the selected two wavelength ranges marked A and B in Fig. 3.10 were compared. The results are shown in Fig. 3.11 (a–d). In the wavelength range A, the spectra experience significant variation in extinction ratio by first decreasing and then increasing as the polarizer rotates from 0° to 90°. As shown in

Fig. 3.11 (a), the extinction ratio reaches a maximum value of 20.3 dB at 0° (x-polarized) and gradually decreases to 2.07 dB at 45° and then recovers back to 18.58 dB at 90° (y-polarized). The spectral shifts are also large. The spectral peak (where the outputs have minimum values) shifts to the longer wavelengths as the polarization changes from 0° to 90°. The total shift value is approximately 10 nm which is almost half the FSR. The relationship between the peak wavelength shift and the polarization state is shown in Fig. 3.11 (b). In the wavelength range B, as shown in Fig. 3.11 (c and d), the spectra experience similar trends but much less prominent changes in both extinction ratio and peak wavelength. The maximum extinction ratio variation and spectral shift caused by polarization changes are 5.8 dB and 1.9 nm respectively.

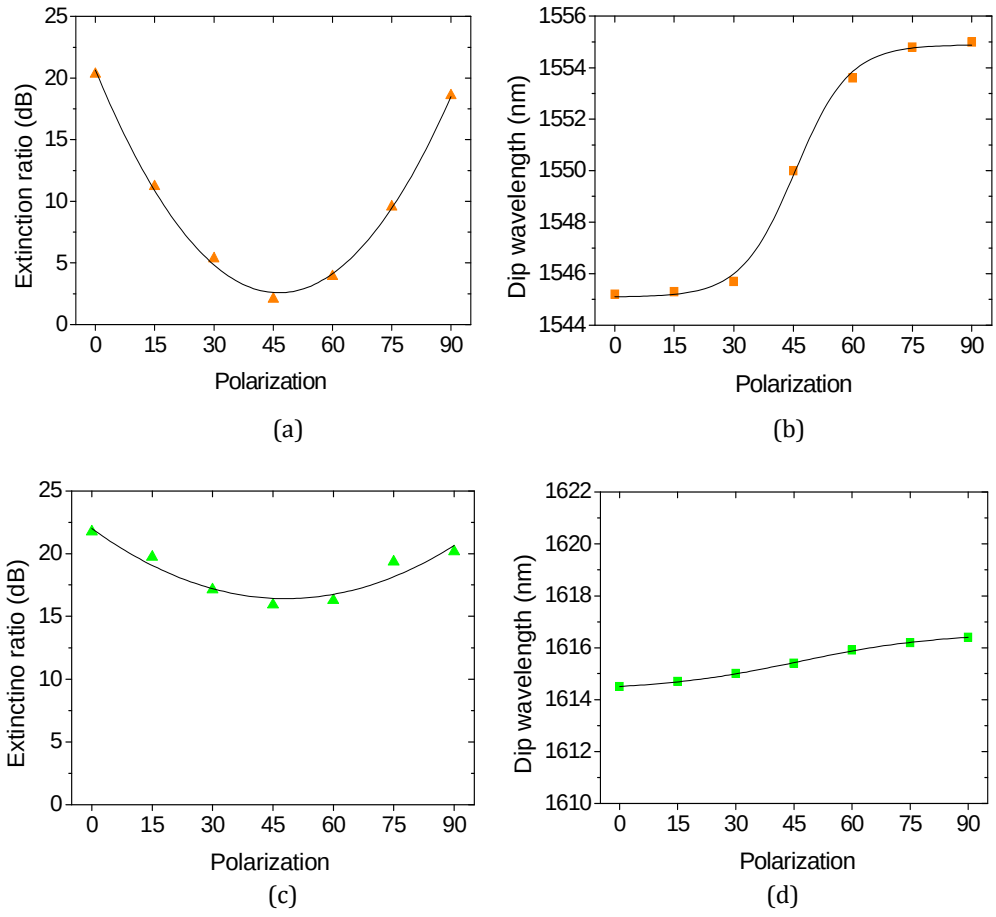

Figure 3.11: (a) (c) Spectral extinction ratio vs. linear polarization angle for wavelength ranges A and B respectively. (b) (d) Dip wavelength vs. linear polarization angle for wavelength ranges A and B respectively.

Based on the results demonstrated in Fig. 3.10 and 3.11, a number of useful conclusions can be drawn on the design of an OMC based sensor. Firstly, both the FSRs and the

extinction ratios of the transmission spectra of an OMC are polarization dependent. Therefore it is necessary to control the polarization states of the input light with a polarization controller to achieve transmission spectra of high extinction ratios and preferred FSRs of the OMC sample. Secondly, polarization-maintaining optical fibres (PMF) can be considered in developing OMC based sensors. Jung. et al [130] experimentally verified that a tapered optical microfibre based on a PMF exhibits good capability in maintaining linear polarization even when the diameter of the PMF is reduced to 1 μm. Thus it is possible to develop PMF based OMC sensors to minimize the polarization induced measurement error. However, PMFs are expensive and accurate alignment of the input polarization state with the PMF axis is required in practice which can significantly increase cost and complexity. Finally the polarization dependency of an OMC is itself wavelength dependent, as shown in Fig. 3.11. This indicates that it is also possible to reduce the polarization induced error by selecting appropriate operating wavelength range during sensing experiments.

3.5 Temperature dependence

Temperature fluctuation during experiments can be another source of instability and measurement errors for an OMC sensor. Thus the temperature dependency of an OMC which had the same geometry (as shown in Fig. 3.5) as the one used in the previous sections was measured to provide information on controlling temperature cross-sensitivity for an OMC based RI sensor.

The temperature dependence was measured using a similar setup to the one used for the RI sensing experiment. The schematic diagram of the setup is shown in Fig. 3.12. The BBS and the OSA used were the same as the ones used for RI sensing. The transmission spectra of the OMC were measured at different temperatures for the OMC waist region ranging from 100 °C to 1000 °C. The high temperature environment was provided by the ceramic microheater used to fabricate the OMC. The uniform waist region of the OMC was inserted into the center of the slot of the microheater and transmission spectra were recorded at different temperatures. The microheater temperature was increased by increasing the current flowing into the microheater from 1.1 A to 4.8 A with intervals of circa 0.4 A. The measurements were taken every 5 minutes to ensure a stable temperature distribution in the heater.

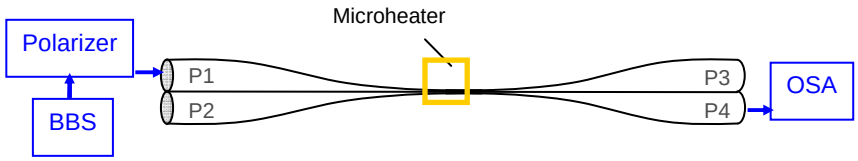

Figure 3.12: Schematic diagram of the experimental setup for measuring the temperature dependence of the OMC structure.

Figure 3.13 shows the spectral dip wavelength shift as the temperature increases from 100 °C to 1000 °C. It can be estimated that the typical temperature dependence of this OMC is circa 18.9 pm/°C. As demonstrated previously, the wavelength shifts occurred in the RI sensing experiment for the OMC are in the order of nanometres. Therefore, when considering temperature as a source of error in a RI sensing experiment, the fluctuation in temperature (such as in room temperature conditions) should have a minute effect on the sensing results. However temperature compensation can be applied if significant temperature variation occurs. It should be noted that the RI of a liquid is, on its own, a temperature dependent parameter. Thus the detected signal may still vary with room temperature during experiment, even if the sensor is temperature compensated.

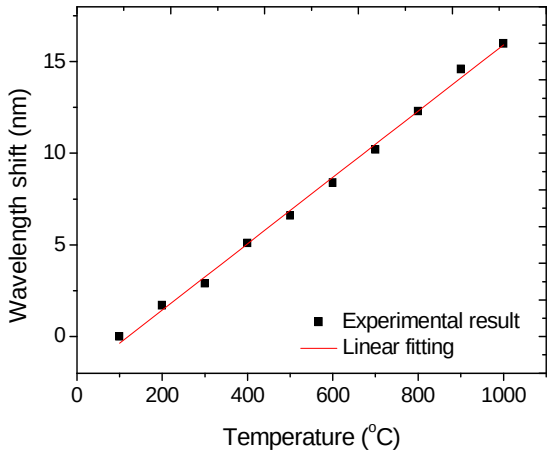

Figure 3.13: Dip wavelength shift vs. temperature variation from 100 °C to 1000 °C.

3.6 Humidity dependence

Environmental humidity can be another factor which affects the stability and lifetime of an optical fibre structure. Research has shown that humidity can accelerate crack

growth in an optical fibre and affect the performance of the fibre device [131][132]. Tapered optical microfibres with small diameters were also shown to degrade in air because of the formation of cracks on the silica fibre surface due to moisture absorption [133]. However related research on the humidity dependence of tapered optical microfibres is not extensive. Thus it is worthwhile to study the humidity dependence of the OMC structure to better understand the impact of humidity variations on sensor performance. An experiment was carried out to measure the humidity dependence of an OMC sample and the results are presented in this section.

Humidity refers to the presence of water in a gaseous state in the environment. A common way to determine the humidity is by measuring relative humidity (RH) which is defined as the ratio of the partial pressure of water vapour in an air-water mixture to the saturated vapor pressure of water at a prescribed temperature [134]. The humidity dependence of a bare OMC device was investigated using a controlled environment chamber (5503-00 with Package F, Electro Tech Systems). The chamber can create environments with various RH values while maintaining a stable temperature.

An OMC sample with a diameter of approximately 2 μm (the diameter for each fused microfibre), which had the same geometry as the samples used in previous experiments, was fabricated. The OMC was pulled straight and the two ends of the fabricated OMC were fixed on two polydimethylsiloxane (PDMS) cubes on a microscope slide using a UV curable polymer adhesive (Efiron PC363), as shown in Fig. 3.14. The waist section was straight and suspended in the humidity controlled environment. This fixing method ensures the mechanical stability of the sensor while maintaining maximum interaction of the OMC with the environment.

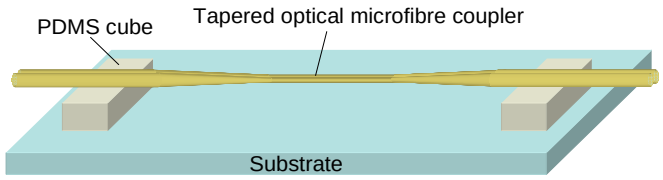

Figure 3.14: Two ends of the straight OMC are fixed on PDMS cubes leaving the waist and transition regions suspended above the substrate.

The prepared OMC sample along with the substrate was placed inside the humidity chamber. As shown in Fig. 3.15, light from a broadband source (BBS) (SLD 6593, Covega) was launched into the input port of the OMC. The output signal from the coupled port of the OMC was analyzed using an optical spectrum analyzer (OSA) (Q8384, Advantest).

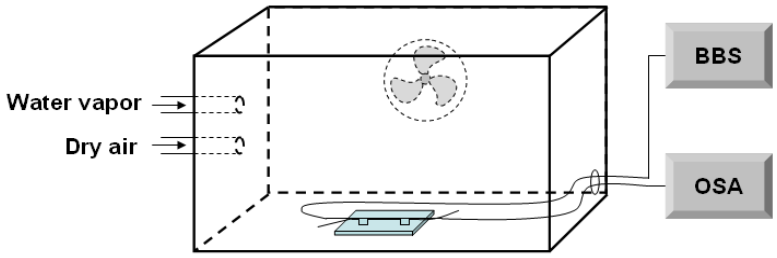

Figure 3.15: Schematic diagram of the setup for humidity measurement. The OMC sample is placed in the humidity chamber and connected with a light source and a detector.

Using the environment chamber, the RH was changed for a range of values from 37% to 97% and the corresponding transmission spectra were recorded. Examples of the spectra when the RH was 48.0%, 62.0%, 94.6% and 95.8% are shown in Fig. 3.16. The temperature inside the chamber was maintained constant at approximately 24 °C during the experiments.

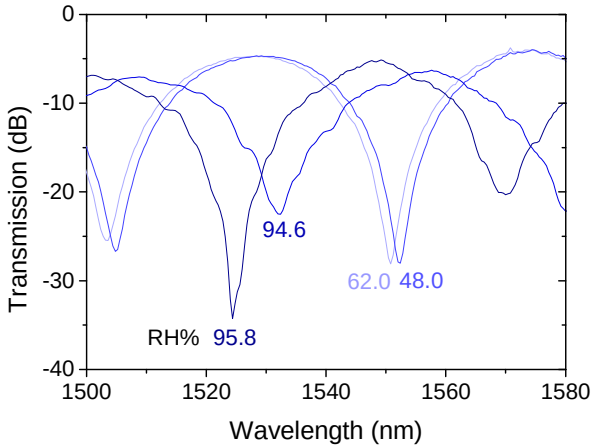

Figure 3.16: Examples of spectral responses of the OMC when the environmental RH is 48.0%, 62.0%, 94.6% and 95.8%. The resonance wavelength shifts to the shorter wavelength range as the humidity increases.

The humidity dependent wavelength shifts for the selected wavelength dip are shown in the upper section in Fig. 3.17. The transmission spectrum of the OMC remains relatively unchanged when the RH is lower than 89.5%. As the RH increases over 89.5%, the

spectra start to blueshift until the RH reaches 95.8%. The shift value within this RH range (89.5%–95.8%) is 32.6 nm, giving an average slope of 2.0 nm/RH%. For even higher RH levels in the range of 95.8%–96.5%, the spectra show large redshifts with an average slope of 53.1 nm/%RH. The extinction ratios of the detected spectra also vary with the humidity. The relationship between the spectral extinction ratio and the humidity is shown in the lower section of Fig. 3.17.

The results of the humidity test showed that RH levels below 89.5% have a very small impact on the performance of the OMC (in a constant temperature condition). RH levels higher than 89.5% can introduce large spectral shifts and in turn large measurement errors. The shifts were found to be nonreversible during the experiment. This nonreversible spectral shifts could be a result of the failure of the sensor due to (1) the formation of dew on the OMC surface [135] and (2) humidity accelerated surface degradation as explained in the first paragraph in this section[136].

It should be noted that the formation of dew is a combined effect of humidity and temperature. In this experiment, temperature was kept constant so dew could only form at very high humidity levels. If the sensor operates in an environment with variable temperature, dew can form at relatively low humidity levels. Similarly the humidity induced degradation of the microfibre surface is also more pronounced in a high temperature environment.

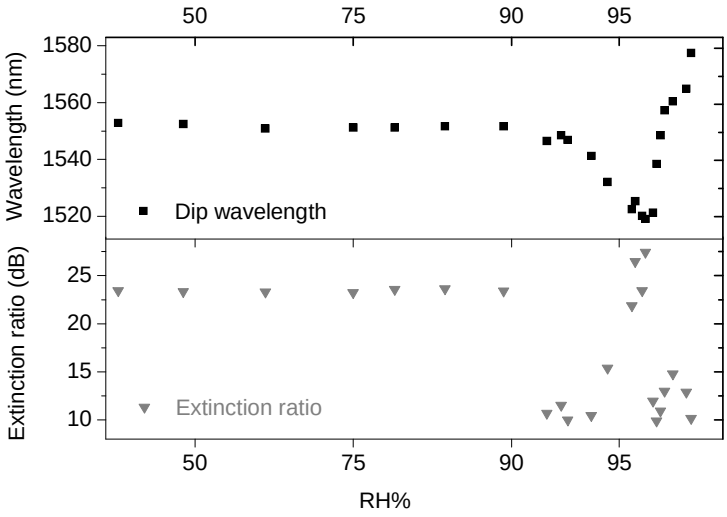

Figure 3.17: Spectral dip wavelength vs. RH (upper section) and spectral extinction ratio vs. RH (lower section).

3.7 A novel humidity sensor based on a polyethylene oxide coated OMC structure

In the previous section, it was shown that changing humidity can cause a large spectral shift, particularly at high humidity levels with dew formation, for an OMC based sensor. However with the aid of a humidity sensitive coating, where the RI of the coating is a function of the local humidity level, an OMC based humidity sensor can be developed. A wide variety of applications such as healthcare, agriculture, food processing and meteorology require fast and accurate measurement of humidity. Conventional techniques for measuring humidity include mechanical hygrometers, chilled mirror hygrometers, wet and dry bulb psychrometers and infrared optical absorption hygrometers [137]. Each of the techniques shows advantages and can be used for humidity measurements in certain applications. However none of them can provide a comprehensive solution with fast response and compact size, coupled to the potential for low sensor cost. Optical fibres present a new versatile platform for humidity sensing to meet the standards.

3.7.1 Principles of operation

In general, optical fibre based humidity sensors require a means by which the evanescent field at the core of the fibre is influenced in a measurable way by changes in the surrounding water vapour level. There are two prerequisites for this:

- **Gaining access to the evanescent field at the core.** For this, fibre cladding can be removed using conventional methods such as either chemical etching or physical polishing. However residual surface roughness can be a problem with these techniques so using tapered optical microfibres is a better approach to gain access to the evanescent field. A number of humidity sensors have been proposed using various structures based on tapered optical fibres or microfibres [138] [139] [140]. OMC was shown, in Section 3.2, to be a simpler structure to provide highly efficient interactions between evanescent field and surrounding environment which makes it a potential candidate for developing humidity sensors.

- **Converting a humidity change to a RI change at the fibre surface**. Most often this is achieved with the aid of a humidity sensitive coating, where the coating RI is a

function of the local humidity level. Many humidity sensitive polymer coatings have been used to develop optical fibre humidity sensors. Among them, Polyethylene oxide (PEO) is well-known as a strongly hydrophilic material and it has been proved that the RI of a thin PEO layer can be modified by water vapour by a number of authors, such as [141][142][143]. PEO has high adhesion on silica surfaces [144] and thus can be easily coated on optical fibres for sensor development.

The following subsections demonstrate a novel humidity sensor based on such a configuration.

3.7.2 Sensor fabrication

An OMC was first fabricated using the same fibre tapering setup and method as demonstrated in Chapter 2. The fabricated OMC had a total length of 25 mm which included a 3 mm long uniform waist region in the center and two 11 mm long transition regions at each end. The OMC was weakly fused since weakly fused couplers are more sensitive to environmental RI changes than strongly fused couplers [10]. The waist diameter was approximately 4 μm for each fused fibre which was wider than the OMC samples used in the RI sensing experiment. This slightly thicker OMC was used in this work for the following reasons. Based on the results of preliminary experiments it was established that application of the PEO coating on the OMC surface tends to significantly decrease the FSRs of the OMC spectrum. Thicker OMCs which exhibit transmission spectra with larger FSR can compensate for this reduction in FSR and produce spectra with suitable FSR values after being coated with PEO. Two identical OMC samples (referred to as sample 1 and sample 2) were fabricated for humidity sensing experiments to demonstrate the feasibility and repeatability of the sensor.

The PEO coating process can be described as follows. The OMC samples were kept in place on the fabrication setup when the fabrication process ended. A glass slide was fixed on a vertical translation stage and placed below the OMC. A few drops of PEO (Sigma Aldrich) in water solution (1 wt %) were placed on the glass slide which was slowly moved up to allow the OMC to be fully immersed in the PEO solution. The OMC was immersed in the PEO solution for 20 seconds and then the PEO solution was removed from the OMC by lowering the vertical translation stage. A thin layer of PEO was thus deposited on the surface of the coupler and formed a configuration as shown in

Fig. 3.18. The PEO coated OMC was then fixed on to a second glass slide in the same way as illustrated previously in Fig. 3.14.

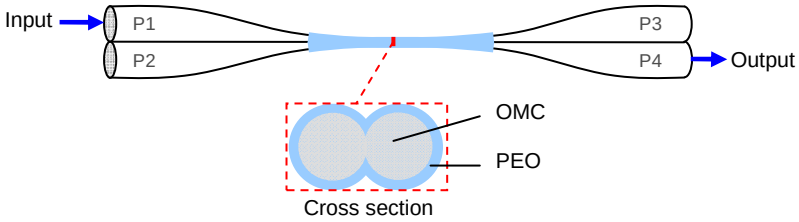

Figure 3.18: Schematic diagram of the humidity sensor configuration showing a weakly fused OMC coated with a layer of PEO.

The sample was kept overnight at room temperature to allow the PEO coating to partially dehydrate and reach a hydration equilibrium with the ambient room humidity. The transmission spectra of the OMC before and after it was coated with PEO were measured and are shown in Fig. 3.19. The OMC with the PEO coating shows a transmission spectrum with significantly smaller FSRs and extinction ratios compared with the bare OMC due to the change of the RI profile around the OMC.

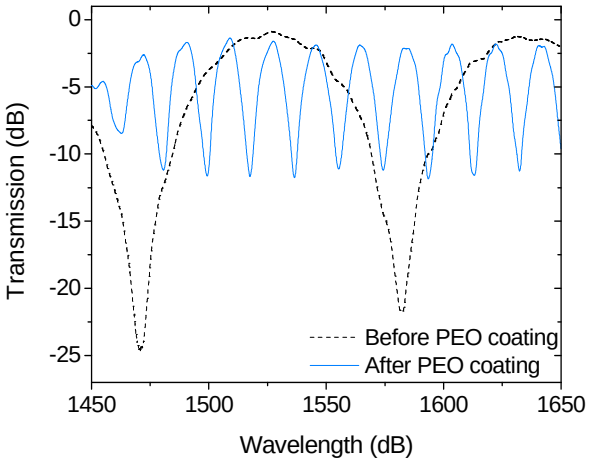

Figure 3.19: Transmission spectra of the OMC before and after its coating with PEO.

3.7.3 Humidity sensing experiment, results and discussion

The same controlled environment chamber as the one used in section 3.6 was used to create an environment with controllable RH values while maintaining a stable temperature. The sensor was placed inside the chamber. Light from a broadband source (BBS) (SLD 6593, Covega) was launched into the input port of the OMC. The output

signal from the coupled port was detected using an optical spectrum analyzer (OSA) (Q8384, Advantest). Using the environment chamber the RH was changed for a range of values from 25% to 85% and the corresponding transmission spectra were recorded. In order to gauge repeatability the experiment was repeated with sample 2 which had the same dimensions as sample 1. The temperature inside the chamber was kept constant at approximately 24±1 °C during the experiments.

Figure 3.20 shows the results obtained in the humidity sensing experiment. As the RH inside the chamber increases the PEO coating absorbs water molecules and its RI decreases. The decrease in the RI of the PEO coating changes the coupling coefficient of the OMC and as a result modifies the spectral response. Figure 3.20 (a) shows the examples of the transmission spectra of sample 1 when the RH is 73.3%, 76.4% and 77.8%. One can see that the resonance dip wavelength experiences a redshift as the RH increases. The dip wavelengths for various RH values ranging from 25% to 85% were measured and the relationships between the RH and the dip wavelength for sample 1 and sample 2 are shown in Fig. 3.20 (b).

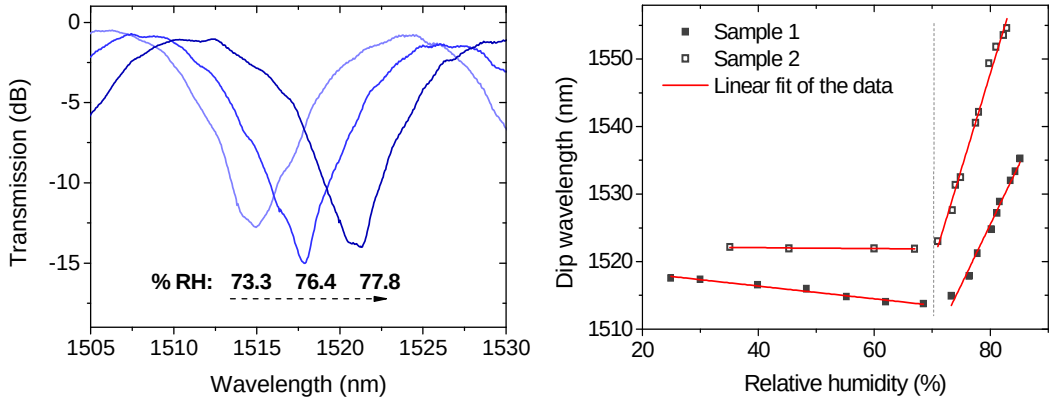

Figure 3.20: (a) Examples of spectral responses of the sensor (sample 1) when the environmental RH is 73.3%, 76.4% and 77.8%. The resonance wavelength shifts to the longer wavelength range as the humidity increases. (b) Resonance wavelength vs. RH for the two samples.

The results for both samples show similar RH responses. Both samples demonstrate two humidity sensing regimes throughout the entire RH range (25%–85%). For the RH range from 25% to 70%, the sensor is relatively insensitive. Small linear blueshifts in the dip wavelength were observed with a sensitivity of -0.095 nm/%RH for sample 1 and -0.005 nm/%RH for sample 2. Once the RH increases over 70%, relatively large redshifts in the

resonance wavelength occur. The RH and the resonance wavelength also show linear correlation with a sensitivity of 1.71 nm/%RH for sample 1 and 2.74 nm/%RH for sample 2. The discrepancy in the results between the two samples is most likely caused by small physical fabrication differences between the two samples which mainly originated from the difficulty in controlling the thickness and uniformity of the coated PEO layer. During experiments, the developed OMC based humidity sensor showed the same or an even faster response than the environment chamber. Therefore the response time of the sensor could not be studied using the same setup. Instead, the response time can be studied by applying a step change in humidity to the sensor with the aid of, for example, human breath exhales. This study of response time requires more investigation.

The difference in the response between the low RH range (25%–70%) and the high RH range (70%–85%) arises because PEO undergoes a phase change from a semi-crystalline to a gel state around 80% RH. The RI of the PEO coating decreases drastically at this phase-transition RH point due to the reduction in the density of the PEO because of an increase in swelling as its water content increases [141]. As a result the sensor showed a high sensitivity in the humidity range which lies above the phase transition RH point.

It is likely that the small blueshift in the low RH range (25%–70%) was a combined result of the RH increase and minute temperature variations. Finally it should be noted that the increase of RH was limited to 85% since higher RH may cause irreversible changes in the PEO coating and render the sensor unusable. However in summary both samples show that the PEO coated OMC proposed here works best as a humidity sensor to detect RH with a high sensitivity of circa 2.23 nm/%RH and a linear response for an RH range from 70% to 85%. This sensitivity is higher than those of other optical fibre based humidity sensors proposed in works such as [142][145] [146][147][148].

3.8 Conclusions

An OMC based RI sensor was demonstrated and the sensor achieved an average sensitivity of 2737 nm/RIU with a maximum sensitivity of 4155 nm/RIU at a RI value of 1.334. Both the theoretical and experimental results indicated that the OMC structure can work as a refractometer with a high sensitivity. The results also indicated that it is

possible to develop a wide range of fibre optic sensors using the OMC structure. Given that the demonstrated OMC based RI sensor showed the highest sensitivity in the range of RIs 1.334–1.335, such a sensor should be particularly suited for biosensing applications as many biological solvents and measurands have RIs in this range. The polarization dependence of the transmission spectra of an OMC was then investigated. The experimental results showed that the transmission spectra of an OMC can be substantially affected by the polarization states of the input light. This suggests that it is feasible to develop OMC based sensors in a wavelength domain with appropriate polarization control of the input light. The temperature and humidity dependencies of the OMC were also investigated. The OMC showed a picometre-scale linear temperature dependency which indicated a limited impact of temperature variations on the RI measurements at room temperature. Studies of the humidity dependence of the OMC showed that high humidity levels and the consequent dew formation on the OMC surface could result in a large RI measurement error.

A novel OMC based humidity sensor with the aid of humidity sensitive PEO coating was proposed and investigated. Experimental results showed that the sensor could detect RH changes in the range from 70% to 85%. A high sensitivity of 2.23 nm/%RH on average was achieved in the above RH range. The sensor has advantages of high sensitivity, compact size and ease of fabrication. Further investigation is needed to improve the performance of the sensor by optimizing the thickness of the PEO coating and incorporating different humidity sensitive coatings, to suit different humidity ranges.

Chapter 4

An Optical Microfibre Coupler Based Biosensor

OMCs can provide higher overall sensitivities than conventional fused couplers. As an example temperature sensors [11][102] and a micro-force sensor [104] have recently been developed based on OMC structures. Biosensors using OMC structures targeted at micro or nano scale entities such as biomolecules and chemical compounds have also attracted researchers' attention [149] given the high sensitivity OMCs can provide as sensors. However, as a newly developed structure, no experimental results have been presented to date to demonstrate the performance of such an OMC based biosensor. This points to strong research potential and hence justification for experimentally developing biosensors using OMCs which the research in this chapter focuses on.

A biosensor is an integrated device which is capable of providing selective quantitative or semi-quantitative analytical information of a target analyte using a biological recognition element [150]. The biological recognition element is called a "receptor". The target analytes could be bioparticles such as DNA, proteins, bacteria, etc. Among various biosensing regimes, immunosensors which measure the presence or the concentration of a molecule in a solution through the use of an antibody as the receptor are of particular interest in this research. Antibodies are proteins produced by plasma cells that act as an immunological response to identify and neutralize foreign objects such as bacteria and viruses. Antibodies work by recognizing a unique part of the foreign objects which is called an antigen. Immunosensors rely on this inherent ability of an antibody to bind to the specific antigen which is similar to a "lock and key" mechanism. Immunosensors are in great demand in hospital testing, life science research and

industry. Examples include clinical diagnostics, environmental control and quality control of food [151][152].

Given the advantages of optical fibre based sensors, such as compact size, high resolution, immunity to electromagnetic interference and the potential for remote operation, several fibre optic immunosensors have previously been developed [153][154][155]. However, the majority of the described sensors require the use of a label which is a molecule (e.g. a fluorophore) chemically attached to aid in the detection of a target analyte. The process of labelling can significantly increase complexity thus label-free detections which do not involve such a labelling process are preferable in many applications. Several label-free immunosensors have recently been demonstrated which consist of simple structures based on nonadiabatic tapered optical fibres [156][157]. Such sensors utilize the evanescent field of the tapered fibre region to enhance the light-biomaterial interaction for biosensing applications. Apart from nonadiabatic tapered fibre structure, a biosensor based on a conventional fused fibre coupler was also proposed by Tazawa et al. in 2007 [101]. In that work the authors demonstrated protein detection by the fibre coupler utilizing an avidin-biotin interaction.

It was previously shown in Chapter 3 that a change in the surrounding RI can strongly influence the OMC transmission spectrum. This points to a possible approach to implement an immunosensor using such an OMC. If a specific antigen is to be sensed or detected, this will be possible if the presence of this antigen in the environment surrounding the OMC alters the RI surrounding the OMC. It is known that antibody-antigen binding can alter local RI [158] and furthermore because binding can take place only for certain antibody-antigen pairing, it is possible to introduce selectivity into the detection of an antigen, by the appropriate selection of an antibody as a so called "receptor" for the antigen. Thus to create an immunosensor, one approach is to arrange for specific antibodies to adhere to the OMC surface due to physical adsorption on the fibre surface, sometimes referred to as "immobilization" of the antibody. The presence of the antibodies allows for the binding of the corresponding antigen and when the specific binding between the antibody and the antigen occurs, the surface RI of the OMC is increased and thus detectable peak wavelength shifts for the transmission spectra occur.

In the experiment demonstrated in this chapter, fibrinogen antigen-antibody pair (so called fibrinogen and anti-fibrinogen) was used as the biosensing element to evaluate the immunosensing performance of the OMC. Fibrinogen is a type of protein that is converted by thrombin through binding with blood platelets in the process of coagulation. Fibrinogen has the advantage that it adheres strongly to silica surfaces [159], and so the need for OMC surface treatment to promote adhesion is avoided with fibrinogen immobilization. For this reason, fibrinogen was used as the receptor to detect anti-fibrinogen for the demonstration of the principle and operation of the immunosensor described here.

A particular challenge in biosensing compared to traditional OMC sensors, such as temperature sensors, is that the sensing process will involve several stages of processing using liquids. Furthermore in biosensing a frequent imperative is that the volume of material or liquid available may be very small (less than a millilitre). For this reason some means to package an OMC sensor in a surrounding structure is needed to minimize the amount of the liquid analytes needed, with the added advantage of providing greater mechanical stability.

Thus in this chapter, an OMC packaging method to improve the performance of the sensing setup is first demonstrated. The performance of the packaged OMC in terms of measurement stability and RI sensitivity is presented and compared with that of the freestanding OMC demonstrated in Chapter 3. Then the capability of the packaged OMC structure to detect thin molecular layers which are deposited onto the OMC surface is demonstrated as a precursor to the biosensing experiment. Finally, the capability of the packaged OMC to detect specific binding between fibrinogen and anti-fibrinogen is presented. Preliminary results on using the sensor to detect human IgG which is more relevant to clinical diagnostics are also presented.

4.1 Packaging an OMC as a preparation for biosensing

A free standing OMC suffers from poor mechanical stability and therefore can be easily affected by environmental influences such as airflow. Necessary experimental processes, such as the application of a liquid onto the surface of the OMC can also disturb the OMC and result in large measurement errors or lack of repeatability. A stable sensing system

is essential in order to achieve accurate sensing results. Thus to improve the system stability during measurements, the OMC was packaged in a surrounding structure using a low RI UV curable polymer (Efiron UVF PC363, Luvantix). The OMC for the biosensing experiment was fabricated using the same setup and method as demonstrated in Section 2.1.2 and Section 3.2. The fabricated OMC sample had a 3–4 mm long uniform waist region and two 13 mm long transition regions on each side. The OMC was weakly fused and the minimum tapered diameter of each fibre was approximately 2 μm.

The polymer packaging technique was similar to that demonstrated in [160][161] with modifications for sensing applications. Briefly, as shown in Fig. 4.1 (a), a microscope slide was first covered with a thin layer of the UV curable polymer. Then two blocks of PDMS were fixed in place in parallel on the polymer surface to create an open-top channel, approximately 3 mm wide. The fabricated OMC was placed into the channel in such a way that the bottom of the coupler adhered to the polymer surface while the rest of the coupler remained exposed to the local environment. Then several drops of the viscous UV curable Efiron polymer were used to seal the two ends of the channel and also to fix the coupler in place. A 20 mm long section in the center of the channel was left uncovered as a sensing window for the biosensing experiments. Then the entire device was cured under UV radiation (CS2010 UV curing LED system, Thorlabs) for 30 seconds. The RI of the cured polymer is approximately 1.36, considerably less than that of silica to ensure low loss.

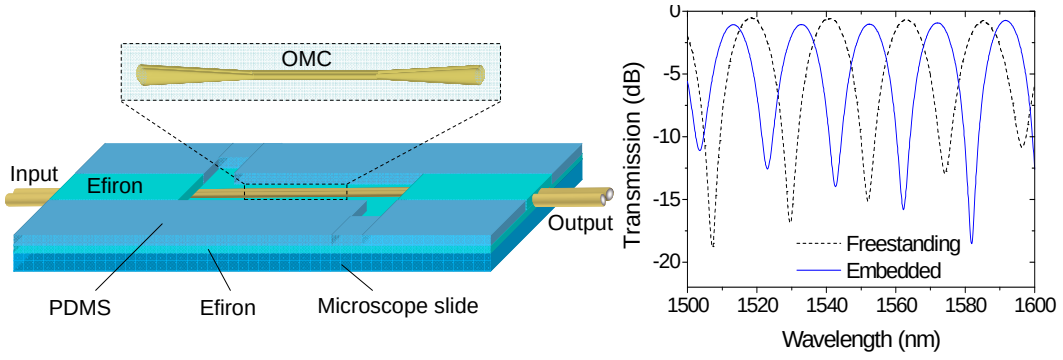

(a) (b)

Figure 4.1: (a) Schematic diagram of a packaged OMC. The uncovered area in the center works as a sensing window. (b) Transmission spectra of an OMC before and after packaging.

During the biosensing experiment, the liquid analyte was placed in and removed from the channel using a pipette. The amount of liquid required is circa 0.2 ml. Examples of

the transmission spectra of an OMC before and after packaging are shown in Fig. 4.1 (b). A large amplitude wavelength shift occurred as the result of the change in the surrounding RI profile induced by the packaging polymer. This shift was expected as it had been previously mentioned in the work described in [161]. A slight decrease in the FSR was also observed.

4.1.1 System stability

The stability of the packaged OMC sensor was tested before conducting the experiment. A small amount of deionized water (circa 0.2 ml) was placed in the sensing window to fully cover the OMC. The transmission spectrum was recorded. The water was then removed and replaced with another 0.2 ml water sample. The transmission spectrum was recorded again. This procedure was repeated 12 times at room temperature to gauge the effectiveness of the polymer structure in providing greater mechanical stability and thus improving repeatability. Changes in the wavelength of the spectral peak are shown in Fig. 4.2. The inset shows an enlarged section of the original recorded transmission spectra overlayed on each other. For an average value of the dip wavelength of 1561.08 nm, a shift of ±0.08 nm was observed during the test indicating good stability and repeatability in measurements for the packaged OMC.

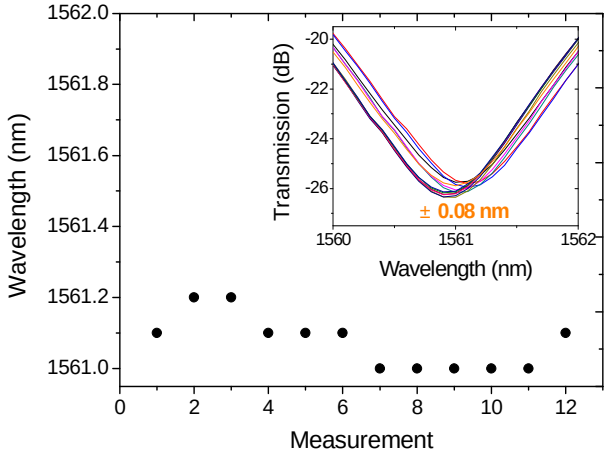

Figure 4.2: Dip wavelength shifts and transmission spectra (inset) recorded during the stability test by repeatedly immersing the OMC sample in and then removing the water sample for 12 times.

4.1.2 RI response

The sensing performance of a packaged OMC might vary from that for a free standing one, so to gain a better understanding of the influence of the packaging process on the RI sensitivity of an OMC, the response of a packaged OMC to changes in the surrounding RI was tested. The experimental procedure was similar to that of the RI sensing experiment demonstrated in Chapter 3. Dimethyl sulfoxide in water solutions with a series of calibrated RIs were placed into the sensing window one after another and the transmission spectra were recorded. Figure 4.3 (a) shows the RI sensing results. The spectral dip shifts exhibit good linearity with a linear coefficient of -0.9996 as the RI changes. The sensitivity is 1837.5 nm/RIU which is lower than the average sensitivity 2723nm/RIU of the free standing OMC demonstrated in Chapter 3. This decrease in sensitivity can be caused by the fact that Efiron polymer reduces the surface contact area of the sensor. Indeed for a packaged OMC, the bottom of the coupler is in direct contact with the Efiron polymer substrate and parts of the transition regions are completely covered by the polymer. Thus such a packaging configuration reduces the contact area between the OMC and the local RI solutions and thus results in a decreased sensitivity.

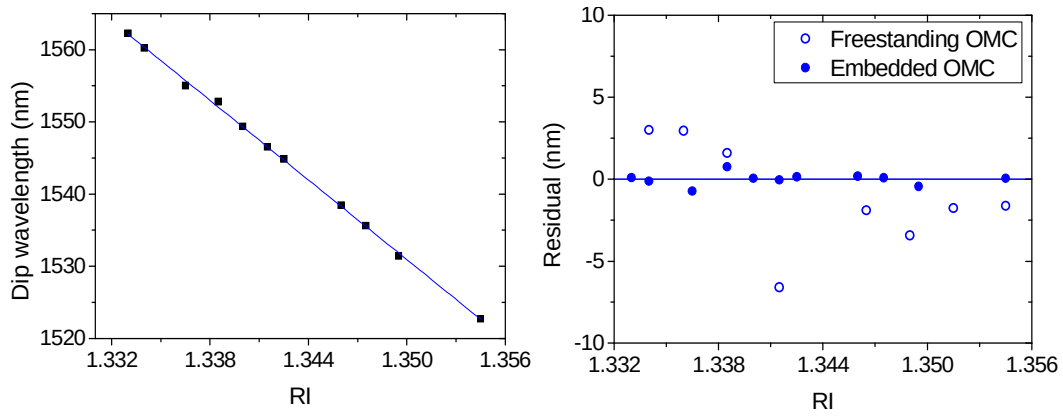

(a) (b)

Figure 4.3: (a) Wavelength shift of the selected spectral peak vs. RI change for the packaged sensor. (b) Error comparison between the RI sensing results for the freestanding OMC and the packaged OMC.

However by comparing the residual (or fitting error) of the measured results for the packaged OMC with those of the freestanding one demonstrated in Section 3.5, as shown in Fig. 4.3 (b) (with the results for the freestanding case drawn from Fig. 3.12 (b)), it is

clear that the residual is much smaller for the packaged OMC which is evidence that the system stability of an OMC based sensor is significantly improved using the packaging process.

4.2 Detection of polyelectrolyte multilayer films

In order to further test the feasibility of the packaged OMC structure to work as a biosensor, the capability of the packaged OMC to detect thin molecular layers that are deposited onto the OMC surface was tested. If the OMC is able to detect RI changes that occur within a few nanometres distance from its surface, the capability of the OMC to work as a biosensor to detect biomolecules with typical sizes of 5–30 nm can be confirmed. This test was performed by depositing polyelectrolyte multilayers (PEM) on the OMC surface using a layer-by-layer self assembly technique [162].

Polyelectrolytes are polymer chains which have charged groups attached to the repeated units. The molecules of a water soluble synthetic polyelectrolyte such as PAH and PSS dissociate and break into polymer chains and counterions. When a substrate is immersed into an oppositely charged polyelectrolyte solution, the polyelectrolyte chains will adsorb onto the surface and rearrange to form a diffusive monolayer. By immersing the substrate into an oppositely charged polyelectrolyte solution, the subsequent polyelectrolyte will adsorb on top of the previous polyelectrolyte due to the electrostatic interactions between the polycations and the polyanions [163]. Unlimited layers of polyelectrolytes can be deposited on the substrate's surface by repeating the same process.

In this experiment, alternate layers of poly (allylamine hydrochloride) (PAH) (cationic) and poly (styrene sulfonate) (PSS) (anionic) were deposited on the OMC surface from their water solutions. The structural formulae of PAH and PSS are shown in Fig. 4.4.

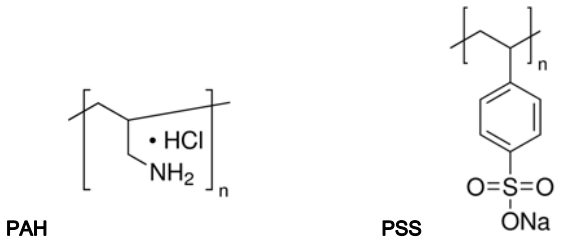

Figure 4.4: Structural formulae of PAH and PSS.

By sequentially depositing the alternately charged PAH and PSS solutions on the surface of the packaged OMC and with a rinse step in between, progressively thicker polymer films can be formed on the OMC surface[164]. The deposition details are as follows (as shown in Fig. 4.5 (a)). Water was placed into the sensing window using a pipette and a baseline spectrum was measured. The water was then removed and replaced with a PAH solution. The PAH was deposited first because silica surfaces are slightly negatively charged under a neutral pH [165]. Thus when solutions which contain positively charged molecules are in contact with the silica surface, the molecules are attracted to the surface and form a diffuse molecular layer. The PAH solution was then left to settle for 15 minutes so the PAH molecules could be immobilized onto the OMC surface. The PAH solution was then rinsed and replaced with water to return the liquid environment to the baseline level. Another spectrum measurement was then taken. The process was repeated with the PSS solution to deposit the negatively charged PSS molecules on top of the previously formed PAH layer. Both the PAH and the PSS solutions had a concentration of 5.5 mg/ml. By repeating the same procedure, PEM can be deposited on the OMC surface. The configuration of the deposited PEM is shown schematically in Fig. 4.5 (b). The thickness of the deposited PEM film can be affected by various factors such as the pH of the solutions and the solvent salt concentration. Typical thickness for a PAH/PSS bilayer assembled at pH 7 is circa 3 nm [166].

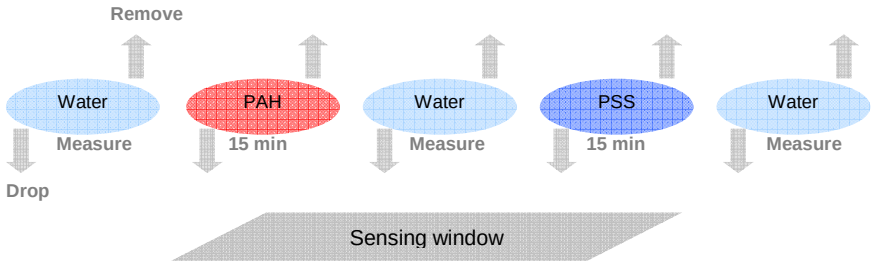

(a)

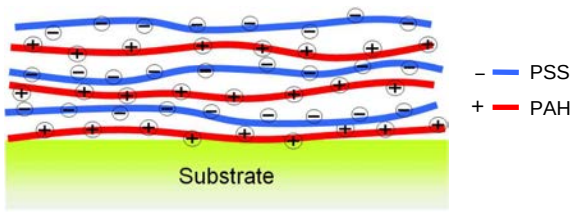

(b)

Figure 4.5: Schematic showing (a) the deposition process and (b) the configuration of the PEM formed by layer-by-layer assembly of positively charged PAH and negatively charged PSS.

Figure 4.6 (a) presents the transmission spectra as various layers of PAH/PSS bilayer were deposited. The spectra show sharp peaks and large extinction ratios of more than 30 dB. Blueshifts are detected corresponding to the formation of each subsequent PAH/PSS bilayer on the OMC surface. The relationship between the spectral shift and the number of the PAH/PSS bilayers is shown in Fig. 4.6 (b). The solid line in the figure is the polynomial fit of the experimental result. An average shift value of 6.24 nm is achieved for each bilayer. Given the typical thickness of a PAH/PSS bilayer of 3 nm [166], the packaged OMC shows a spectral shift of circa 2 nm for every 1 nm thickness of a molecular layer adsorbed on to the OMC surface.

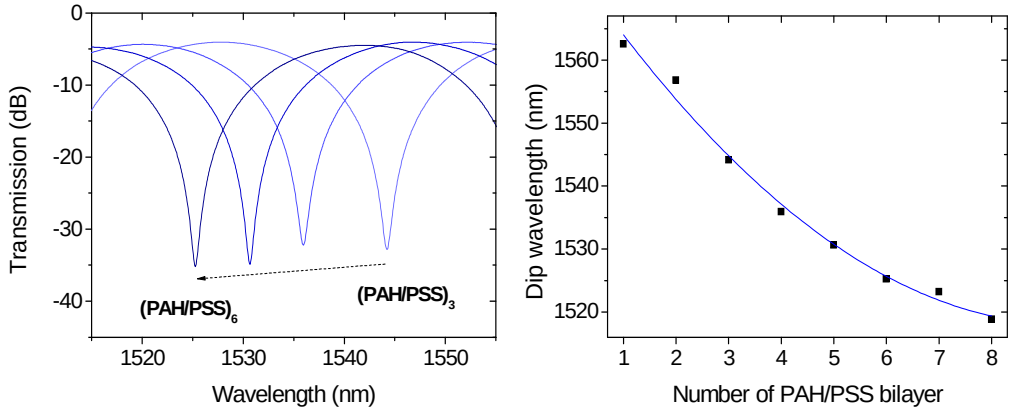

(a) (b)

Figure 4.6: (a) Examples of the spectra corresponding to subsequent deposition of three PAH/PSS bilayers on the OMC surface. (b) Spectral peak wavelength vs. number of deposited PAH/PSS bilayers.

4.3 An OMC based immunosensor

Fibrinogen is a type of protein that is converted by thrombin through binding with platelet in the process of blood coagulation. Fibrinogen is an elongated flexible molecule with a center and 2 identical symmetrical distal regions at its ends [167]. The total length of a fibrinogen molecule is 47.5 ± 2.5 nm. The diameters of the distal regions are in the range of 5 to 7 nm [168]. Due to its particular molecular structure, fibrinogen is flexible and highly adhesive to silica surfaces [169]. As a result, the need for OMC surface treatment to promote protein adhesion is avoided with fibrinogen immobilization. For this reason, fibrinogen was used as the receptor and anti-fibrinogen was used as the analyte to demonstrate the principle and operation of the proposed immunosensor.

4.3.1 Fibrinogen immobilization

An OMC was first fabricated using the same method as previously demonstrated. The fabricated OMC had a 3–4 mm long uniform waist region and two 13 mm long transition regions on each side. The OMC was weakly fused and the minimum tapered diameter of each fibre was approximately 2 μm. Then the OMC was packaged using the method described in Section 4.1.

The human fibrinogen used in the experiments (95% clottable and plasminogen depleted) was purchased from Calbiochem, Merck KGaA. Before immobilizing the fibrinogen, a baseline spectrum of the OMC was measured. For this, the OMC sensing window was fully covered with 0.2 ml phosphate-buffered saline (PBS) and the transmission spectrum was recorded as the baseline and then the PBS was removed. Finally the fibrinogen was immobilized on the surface of the sensing region of the packaged OMC. This was achieved using a fibrinogen solution in a PBS buffer (0.2 ml, 100 μg/ml). The solution was left to settle for 20 minutes so the fibrinogen molecules could fully adsorb onto the bare OMC fibre surface. In order to measure the changes caused by the immobilized fibrinogen only, the sensing window was then rinsed with the PBS buffer several times. The rinse step returned the liquid environment to the baseline level and also removed any loosely bound fibrinogen.

Figure 4.7 (a) schematically illustrates the fibrinogen immobilization on the OMC surface. Figure 4.7 (b) gives a typical example of the transmission spectrum evolution during the fibrinogen immobilization. The evolution in time of the wavelength dip caused by fibrinogen immobilization is also shown in Fig. 4.7 (c). A rapid spectral blueshift occurs in the first 5 minutes, followed by a much slower shift. The shift reaches a plateau within 20 minutes which indicates that the OMC surface has been fully occupied by the fibrinogen molecules. A total blueshift of 13.6 nm was observed for the entire immobilization process.

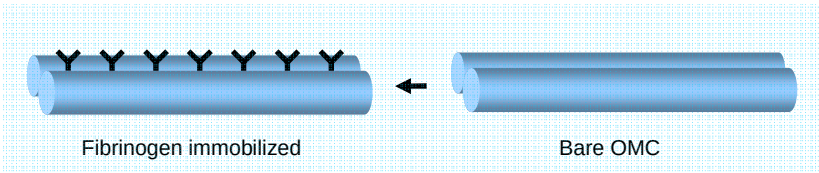

(a)

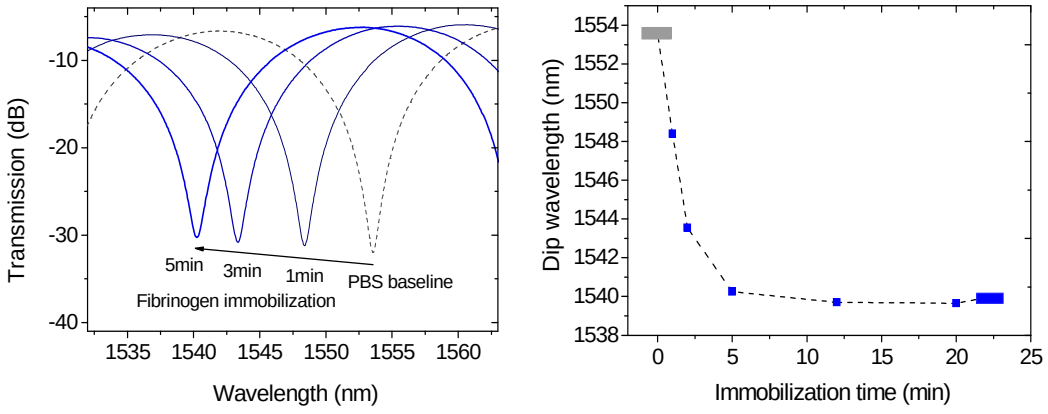

(b) (c)

Figure 4.7: (a) Schematic diagram of fibrinogen immobilization on the OMC surface. (b) Spectral response during the first 5 min of the fibrinogen immobilization. (c) Time dependent wavelength shift for the fibrinogen immobilization.

For the 15 samples studied, the fibrinogen immobilization caused an average blueshift of 12.22 nm with a standard deviation of 1.51 nm, as shown in the lower section of Fig. 4.8. The discrepancy in the fibrinogen immobilization among the samples was believed to mainly result from the limited precision in the OMC fabrication. For example, the tapered diameter and the coupling length for each OMC sample may vary. This is suggested by the variation in the FSR among the fabricated samples, as shown in the upper section of Fig. 4.8. Based on the experience in OMC characterization acquired in this research, even very small variations in the OMC diameters and coupling lengths can lead to relatively substantial variations in the spectral FSR and in the relationship between wavelength shift and local RI change

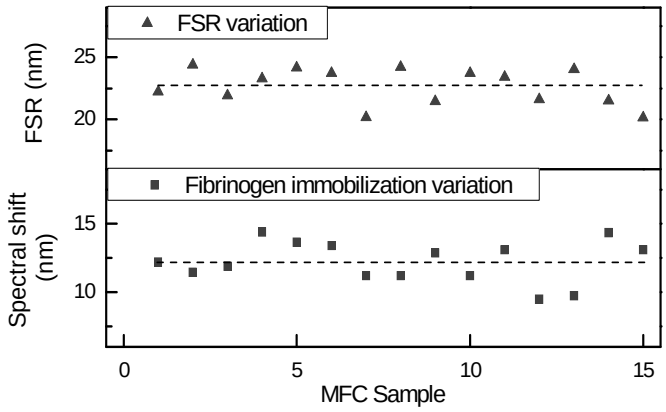

Figure 4.8: Spectral differences observed for the 15 studied OMC samples during the fibrinogen immobilization.

4.3.2 Anti-fibrinogen detection

Fibrinogen was used as the recognition element (receptor) to detect anti-fibrinogen as mentioned previously. Once the fibrinogen was immobilized on the OMC surface, rabbit anti-fibrinogen solution (Calbiochem, Merck, KGaA) in a PBS buffer (0.2 ml, 100 µg/ml) was applied to the sensor. The anti-fibrinogen solution was left to settle for 60 min and the measurement was taken during the binding and after the rinse step. In order to verify the selectivity of the sensor for anti-fibrinogen among unspecific antibodies, a negative control was performed using Immunoglobulin G antibody (goat anti-human IgG, Sigma Aldrich). The control was performed with the same procedure above using an anti-IgG solution in PBS buffer (0.2 ml, 100 µg/ml).

Figure 4.9 (a) schematically illustrates the anti-fibrinogen binding with the immobilized fibrinogen. The typical behaviour of the sensor in distinguishing between the anti-fibrinogen and the anti-IgG is shown in Fig. 4.9 (b) and (c).

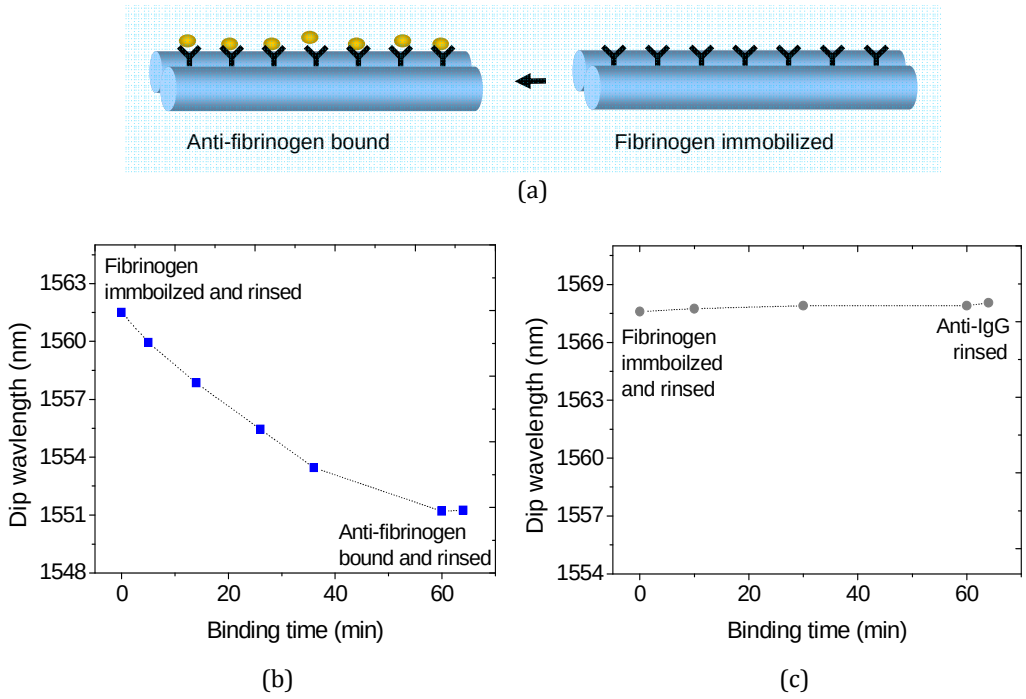

Figure 4.9: (a) Schematic diagram showing anti-fibrinogen binding with fibrinogen. Dip wavelength shift with time for (b) anti-fibrinogen binding experiment and (c) anti-IgG control experiment.

The binding between the anti-fibrinogen and the fibrinogen occurs gradually over a period of 60 minutes. After this period, a PBS rinse is used to remove any loose anti-

fibrinogen, the presence of which might impact on the measured shift. Following the rinse, the total blueshift caused by the bound layer of anti-fibrinogen molecules was mesasured as 10.35 nm. In comparison, the anti-IgG control caused a post-rinse 0.45 nm redshift over the same length of time. This is because the fibrinogen does not specifically interact with the anti-IgG and thus the anti-IgG can not be captured by fibrinogen. The significant difference between the two results in spectral shift indicates that the sensor is capable of distinguishing between specific anti-fibrinogen and non-specific anti-IgG. The relatively small redshift caused by the anti-IgG is most likely a result of measurement error. It should be noted that although it took over 60 minutes for the sensor to reach a plateau when detecting anti-fibrinogen, the sensor started to show a significant shifts of over 1.5 nm within the first five minutes of reaction.

The sequence of experimental steps above is summarized in Fig. 4.10. This sequence was repeated using anti-fibrinogen solutions with various concentrations ranging from 25μg/ml to 100 μg/ml. Since the binding of fibrinogen is nonreversible and the cost of fabricating new sensors is low, for each concentration the starting point was a new OMC. The concentration of the fibrinogen solution used with each OMC remained constant at 100 μg/ml.

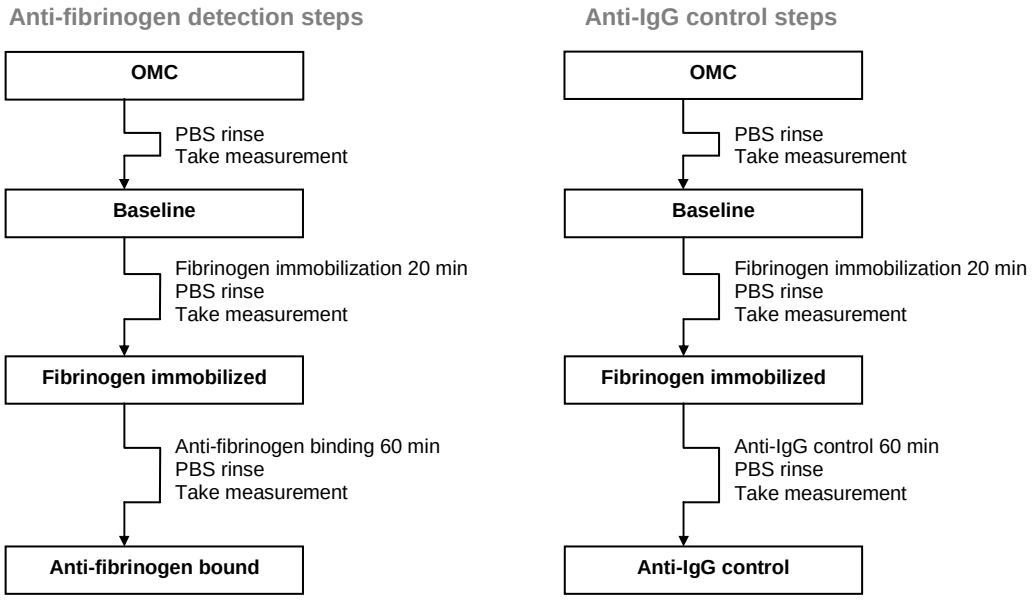

(a) (b)

Figure 4.10: Diagrams showing the experimental steps for conducting (a) anti-fibrinogen detection and (b) anti-IgG control experiments respectively.

The anti-fibrinogen sensing results are shown in Fig. 4.11. The detected signal increases with the increasing concentration of the anti-fibrinogen solution. This indicates that the detected signal for the sensor increases with the amount of the anti-fibrinogen present in the system. The results for the control anti-IgG are consistent and demonstrate the selectivity of the sensor between the specific and the non-specific analytes. In order to gauge reproducibility, the experiment was repeated three times for each concentration, as mentioned previously each repetition was of necessity performed on a newly fabricated sensor. The control experiment with anti-IgG was also repeated several times. In Fig. 4.11 the solid line is the polynomial fitting of the mean of the anti-fibrinogen detection results.

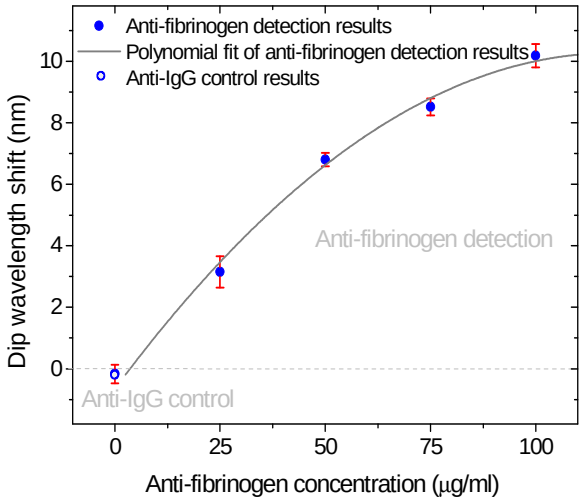

Figure 4.11: Variations in the spectral shift caused by anti-fibrinogen with the anti-fibrinogen solution concentrations (25 μg/ml, 50 μg/ml, 75 μg/ml and 100 μg/ml). The experiment was repeated 3 times for each concentration. All the repetitions were performed individually on newly fabricated sensors. The solid line is the polynomial fitting of the mean of the anti-fibrinogen detection results.

By taking a slope of the fitted curve, the sensitivity of the sensor for detecting anti-fibrinogen with a concentration of 25 μg/ml is calculated to be approximately 0.14 nm• ml/μg. The error bars in Fig 4.11 represent the standard deviation of the repeated measurement results at each concentration and confirm the repeatbility of the sensor. The most likely reason for the errors are small physical differences among the OMC samples, as previously mentioned in relation to Fig. 4.8. Temperature fluctuations may also be a contributing factor. The mechanisms behind the protein adsorption and binding regimes are beyond the scope of this thesis.

Finally it is worth mentioning that in the experiment above, an OSA was used to measure wavelength shift, but in a practical sensor system the use of an OSA would add considerable expense to the overall system. In order to reduce the cost of the interrogation system, the sensor can also be operated in an intensity domain at a fixed wavelength. For this, the BBS and the OSA can be replaced with a laser diode, an edge filter and a photodiode based optical power meter [170]. As an example of intensity domain operation, Figure 4.12 shows the transmission spectra and the corresponding output power variation for a studied sample to detect the specific binding between fibrinogen and anti-fibrinogen (with a concentration of 50 µg/ml).

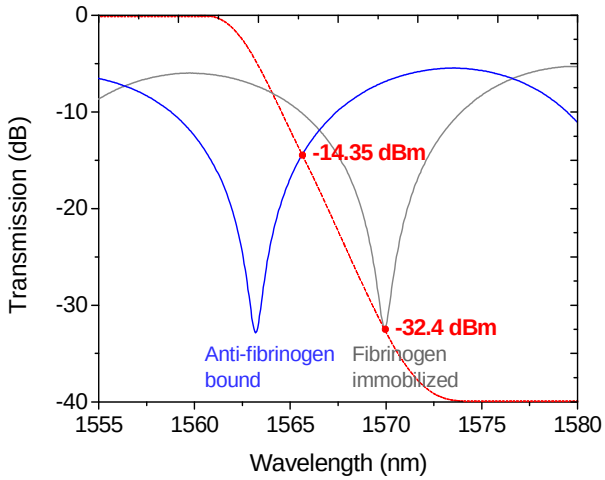

Figure 4.12: Transmission spectra and corresponding power variation with an edge filter (red dashed line) before and after anti-fibrinogen (50µg/ml) binding with fibrinogen for a studied sample.

Given a 0 dBm input power, the detected output power for the sensor (with fibrinogen immobilized) is -32.4 dBm at a 1570 nm wavelength. After the anti-fibrinogen binding step, the detected output power along the edge filter (red dashed line) is -14.4 dBm at 1566 nm wavelength which is 18.0 dB larger than the sensor's initial output power. This difference in the detected output power confirms that the sensor has the capability to work in the intensity domain with a non-OSA based interrogation system, based on a low cost edge filter.

4.4 An immunosensor for detecting IgG

The capability of the packaged OMC to work as an immunosensor using fibrinogen and anti-fibrinogen was demonstrated in the last section. However while the use of a fibrinogen antibody-antigen pairing is useful to determine if the sensor works, in practice the detection of anti-fibrinogen lacks clinical relevance in real applications. Thus in this section proof-of-principle results on the sensor's performance in detecting more clinically relevant IgG are demonstrated. IgG is the most abundant type of antibody found in all human body fluids and protects against bacterial and viral infections. Detecting the presence and the level of IgG in human blood can be used to help diagnose a wide variety of diseases and immunodeficiencies.

Human IgG is a type of antibody. When injecting human IgG into a host of a different species, such as goat or rabbit, human IgG works as an antigen to trigger the immune system of the host animal to generate anti-human IgG which is a type of secondary antibody. Thus human IgG can be detected using anti-human IgG raised in animals based on the high affinity between the two. In this experiment, goat anti-human IgG (anti-IgG) (Fab specific, Sigma) was used as the receptor to detect human IgG (IgG) (Thermo Scientific Pierce).

4.4.1 Sensor fabrication

An OMC with the same geometry as the one used in Section 4.3 was fabricated using the same microheater brushing technique. The sensor preparation process was similar to the process demonstrated in Section 4.3.1. Before immobilizing the anti-IgG, the OMC was immersed in PBS and the transmission was recorded as a baseline spectrum. Then the PBS buffer was removed and replaced with the anti-IgG in a PBS solution (50 μg/ml). The solution was left to settle for 30 min for the anti-IgG to adsorb on the OMC surface. The sensing region was then rinsed with the PBS buffer. The transmission spectra before and after the anti-IgG immobilization are shown in Fig. 4.13, with a total blueshift of 7.2 nm. The blueshift showed that the anti-IgG was immobilized on the OMC.

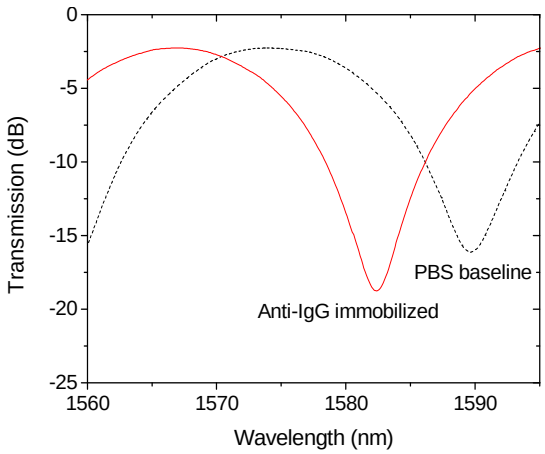

Figure 4.13: Transmission spectra before and after anti-IgG immobilization on the OMC surface.

4.4.2 IgG detection

In order to verify the selectivity of the sensor to IgG among other nonspecific proteins, a control step was performed using Protein A. Protein A in PBS solution with a concentration of 50 μg/ml was applied and left to settle for 30 min. A measurement was taken after rinsing the OMC with PBS. Following the Protein A control step and rinse, the IgG binding step was performed. The human IgG in PBS solution had the same concentration as that of the Protein A solution (50 μg/ml). The sensing results are shown in Fig. 4.14.

A small blueshift of 0.2 nm was observed after the Protein A control step. In comparison, the IgG binding step caused a large blueshift of 12.2 nm. The significant shift indicates that the specific binding between the IgG and the anti-IgG occurred and as a result the IgG formed another biomolecular layer on top of the anti-IgG layer. The small shift caused by the Protein A could be a result of measurement error or a small amount of Protein A molecules adsorbing on the unoccupied sites on the fibre surface. The significant difference in the spectral shifts indicates that the sensor was able to distinguish between the matched IgG and the un-matched Protein A in the wavelength domain.

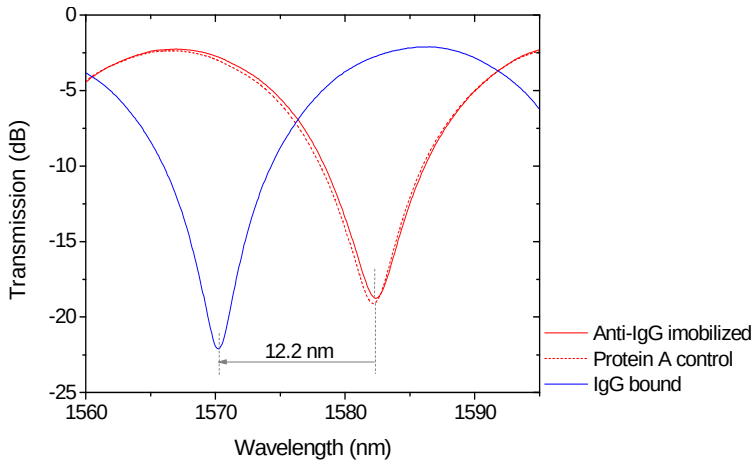

Figure 4.14: Transmission spectra for Protein A control and IgG detection. The binding IgG and anti-IgG caused a blueshift of 12.2 nm while the Protein A control only caused a 0.2 nm blueshift.

While this experiment proves in principle that the more clinically relevant binding of IgG and anti-IgG can be detected, it is recognized that in practice further development of such a sensor would require functional coatings on the silica surface prior to anti-IgG immobilization. This is because the anti-IgG immobilization on silica is not stable [171] as in the fibrinogen case, due to the relatively weak physical adsorption known to exist between anti-IgG and a silica fibre surface. In practice the immobilization of anti-IgG could be improved by creating suitable functional groups on the OMC surface. For example, by adding silanol functional groups to the OMC surface through glass hydroxylation to assist anti-IgG immobilization.

4.5 Conclusions

The mechanical stability of an OMC based sensor was improved by packaging the OMC in a UV curable polymer with low RI. The sensitivity of the packaged OMC was lower than that of a freestanding one. However the stability during experiments was significantly improved. The capability of such a packaged OMC to detect surface deposited thin PEM films showed the feasibility of the OMC to work as a biosensor. A label-free immunosensor based on the packaged OMC structure was experimentally demonstrated using a fibrinogen antigen-antibody pair. The sensor was fabricated by immobilizing fibrinogen on the sensing surface of the packaged OMC. The performance of the sensor in identifying anti-fibrinogen in the wavelength domain was evaluated. Results showed

that the OMC based immunosensor is capable of detecting anti-fibrinogen and that the detected signal is proportional to the concentration of the anti-fibrinogen solution. For a more clinically relevant immunosensing application, an IgG sensor was developed by immobilizing anti-IgG on the surface of the OMC sensing region. In principle it was shown that the sensor could detect the specific binding between the anti-IgG and IgG. Given the advantages such as label-free detection, fast response relatively easy and low-cost fabrication, an OMC based biosensor offers a reliable, compact, simple solution to the need for immunosensors. The binding between antibody and antigen is not reversible. Using tapered OMC to fabricate the immunosensor is very low cost and thus can support disposable applications of the sensor.

Chapter 5

Optical Microfibre Sensors incorporating Gold-silver Alloy Nanoparticles

For microfibres with diameters which are large compared with the wavelength of the transmitted light, only a small proportion of the light energy is present within the evanescent field, as explained in Chapter 2. Thus while a large diameter microfibre is more mechanically robust, the capability of such a microfibre to detect changes in the surrounding environment is limited, resulting in an undesirable tradeoff between mechanical stability and sensitivity for the sensor, as explained in Chapter 1. To mitigate this tradeoff, when the surface of a relatively wide diameter microfibre is coated with conductive nanoparticles, the electrons of the nanoparticles surrounded by the evanescent field can be excited into an oscillatory motion [172], as shown in Fig. 5.1. This electron oscillation results in an enhanced electromagnetic field at certain resonance wavelengths which are highly localized at the nanoparticle-environment interface. Such a collective electron oscillation on the surface of conductive nanoparticles caused by incident electromagnetic radiation is called localized surface plasmon resonance (LSPR).

LSPR has the potential to deliver strong light-matter interaction. An LSPR field has a very high spatial resolution in that it exhibits a high intensity and this occurs over a very short decay distance for the resonance field. Typical decay distances of LSPR are within a range of 5–30 nm [173]. Light-environment interactions can be enhanced by coupling the light transmitted through a microfibre into the LSPR of the nanoparticles via the evanescent field of the microfibre. The intensity and frequency of the LSPR are highly dependent on factors such as the nanoparticles' composition, size, shape, and the

dielectric properties of the medium [174]. Small changes occurring on the nanoparticles' surface such as trapped biochemical molecules can interact with the LSPR and in turn efficiently modify the light transmission along the microfibre. Therefore a microfibre-nanoparticle facilitated LSPR structure is a promising approach for developing sensors with improved sensitivity [175] which can mitigate the mechanical stability-sensitivity tradeoff discussed above.

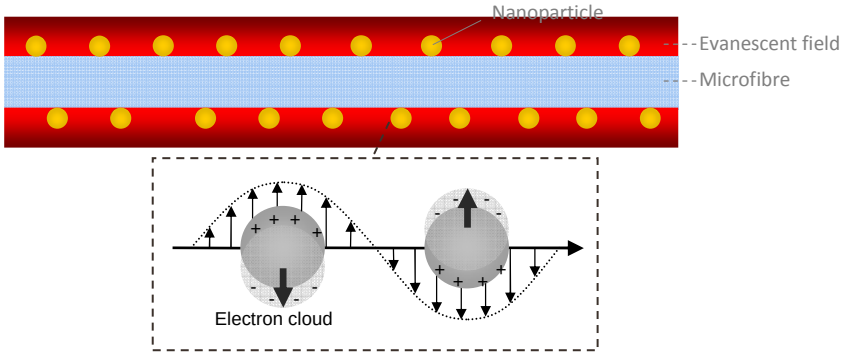

Figure 5.1: Schematic diagram showing nanoparticles deposited on the microfibre surface. The enlarged image shows that the evanescent field of the microfibre works as the source to generate LSPR on the nanoparticles' surface.

Nanoparticles made of noble metals such as gold or silver are often used to generate LSPR for sensing applications, but each material has different advantages and disadvantage. For example, silver has a larger magnitude for the real component of the dielectric function compared with gold. Thus a silver nanoparticle has more polarized charges when excited by incident light and shows stronger plasmon effects than a gold nanoparticle with the same geometry [15]. However silver nanoparticles are relatively cytotoxic with bio tissues and can be easily oxidized. Gold nanoparticles, on the other hand, are chemically stable and easy for biomolecules to immobilize with the help of surface functionalization [176]. To incorporate the advantages of both materials, gold-silver (Au-Ag) alloy nanoparticles, which inherit properties from both gold and silver, can be used to develop highly effective LSPR sensors with improved performance and tunable physicochemical properties by controlling the Au-Ag composition ratio [177].

Much work has been published on the study of the optical and biological properties of Au-Ag alloy [178][179][180] or bimetallic Au-Ag shell structures [181][182][183]. However combining Au-Ag alloy nanoparticles with optical fibres to develop fibre optic

LSPR sensors have received little attention and only a small amount of work has been published [184][176]. In 2005, Sharma et al. [184] demonstrated the principle of a surface plasmon resonance (SPR) sensor by forming an Au-Ag nanoparticle film on the surface of a short section of an exposed fibre core. The performance of the proposed sensor with various Au-Ag compositions and the thicknesses of the nanoparticle film were also studied theoretically. In 2013, Tu et al. [176] experimentally demonstrated an optical fibre based LSPR sensor fabricated by immobilizing Au-Ag alloy nanoparticles on the surface of a cladding-removed optical fibre. In that paper, the effects of Au-Ag ratios and the sizes of the nanoparticles on the performance of the sensors in detecting local RIs were demonstrated.

Tapered optical microfibres have many advantages (as explained in Chapter 1) over conventional mechanically polished or chemically etched optical fibres. Alloy nanoparticles have the advantage that they offer tunable physicochemical properties (as will be explained in the next section) over nanoparticles with a single composition. Thus a unique sensing configuration is possible by combining tapered optical microfibres with Au-Ag alloy nanoparticles which can combine the advantages of the two to develop sensing applications with improved biosensitivities, miniaturized sizes, ease of fabrication, ease of interconnection and tunable physicochemical properties.

In this chapter, a sensor based on a tapered optical microfibre which incorporates Au-Ag alloy nanoparticles is experimentally demonstrated. The LSPR effects of the microfibre sensor incorporating Au-Ag nanoparticle with different alloy formulations are compared and analyzed. The performance of the sensor in detecting surrounding RI changes and adsorbed polyelectrolyte multilayers (PEM) is presented. A novel pH sensor based on a microfibre coated with a composite PEM-nanoparticle-PEM (PEM-NP-PEM) nanostructure is demonstrated.

5.1 Fabrication of the LSPR based microfibre sensor

This section describes the fabrication process for a microfibre-nanoparticle based LSPR structure. The fabrication involves three steps: (1) nanoparticle synthesis; (2) microfibre fabrication and (3) nanoparticle immobilization on the microfibre surface.

5.1.1 Nanoparticle synthesis

The alloy nanoparticles were fabricated using the method described in [10]. Taking as an example the synthesis of alloy nanoparticles which contain 50% gold and 50% silver (50%Au50%Ag) (as a molar ratio), the process is briefly as follows. In a 250 ml round bottom flask, 95 ml of 0.126 mM gold(III) chloride trihydrate ($HAuCl_4$, Sigma) (4.71 mg) and 0.127 mM silver nitrate ($AgNO_3$, Sigma) (2.04 mg) was left to boil until reflux occurred with vigorous stirring. While in the reflux state, 5 ml of 34 mM sodium citrate tribasic dihydrate ($HOC(COONa)(CH_2COONa)_2 \bullet 2H_2O$, Sigma) (50 mg) was added and reflux was maintained for 15 minutes with vigorous stirring. After this, the colloidal solution, containing the synthesized nanoparticles, was left to cool down to room temperature. Subsequently, the colloidal solution was centrifuged at 233×g for 20 minutes in order to remove any unwanted silver precipitate that may have formed.

The synthesized nanoparticles were then coated with a layer of poly(ethylene oxide) (PEO) using the method described in [185] to increase the chemical stability of the nanoparticles. Briefly, 10 nM of the nanoparticles solution were mixed with 0.02 mg/ml of a commercial hetero-functional PEO ($C_{15}H_{32}O_7S$, 356.48 Da, Sigma) in an aqueous solution of sodium dodecyl sulphate (SDS) (0.028%, Sigma). NaOH with a concentration of 25 mM was then added to the mixture. The mixture was incubated for 16 hours at room temperature. Excess PEO was removed by centrifugation (21.460 ×g, 30 minutes at 4 °C).

Alloy nanoparticles with different Au-Ag formulations were prepared using the same method by using different ratios of $HAuCl_4$ and $AgNO_3$. The Au-Ag formulations were determined by inductively coupled plasma (ICP) and energy-dispersive X-ray spectroscopy (EDX). Au-Ag nanoparticles with three alloy formulations (25%Au75%Ag, 50%Au50%Ag and 75%Au25%Ag) were synthesized for the later experiments. Figure 5.2 shows photographs and the absorption spectra (normalized to the highest measured absorbance value among the three nanoparticle samples) of the synthesized alloy nanoparticle colloids. The spectra were measured using a UV-Vis spectrophotometer.

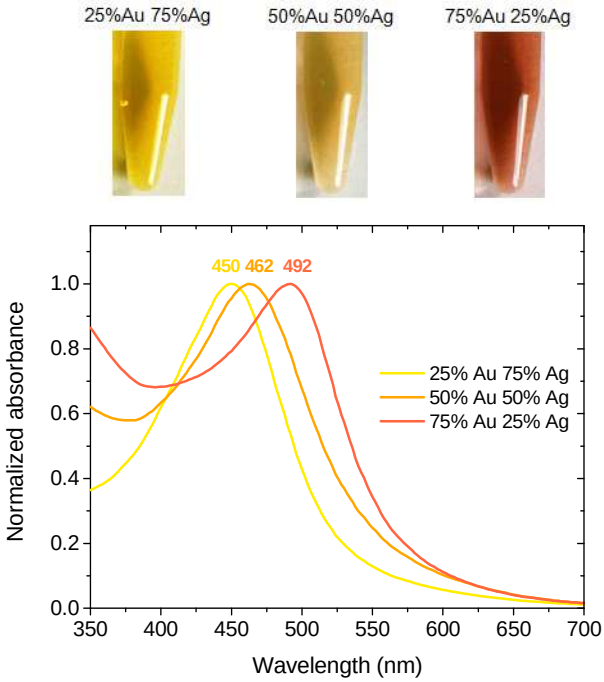

Figure 5.2: Photographs of the synthesized colloidal nanoparticles and their absorption spectra (normalized to 1).

Figure 5.3 shows the transmission electron microscope (TEM) images of the fabricated alloy nanoparticles and their size distributions analyzed using ImageJ software. Alloy nanoparticles fabricated by the method described above vary in size. For example from Fig 5.3 (a) it is clear that for the 25%Au75%Ag case, there are a range of nanoparticle sizes. However between different alloy formulations the average nanoparticle size is reasonably similar (within circa 12% of each other). The effects associated with this difference in nanoparticle sizes as a function of alloy formulation are small compared with those caused by the difference in particle composition as discussed in [176] [186] and thus are not discussed further in this thesis.

(a)

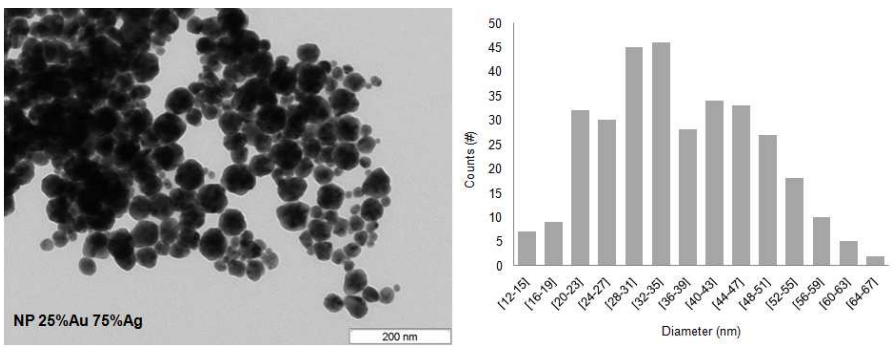

(b)

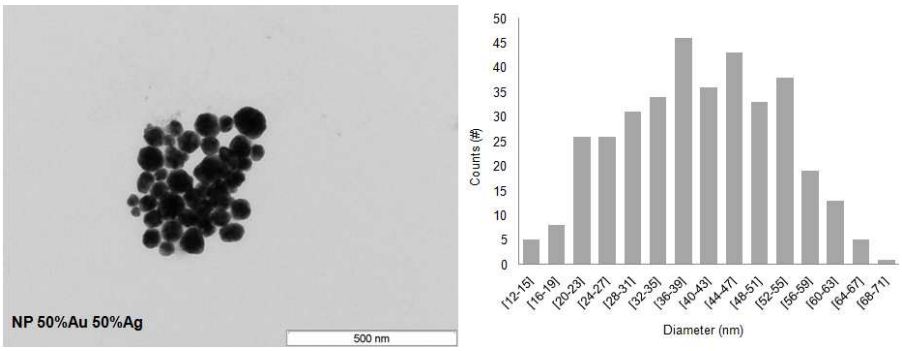

(c)

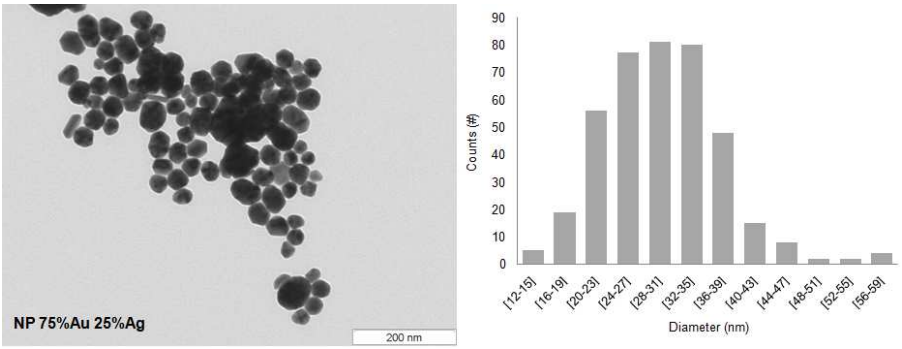

Figure 5.3: TEM images and size distributions of the nanoparticles with (a) 25%Au75%Ag, (b) 50%Au50%Ag and (c) 75%Au25%Ag alloy formulations.

5.1.2 Microfibre fabrication

An optical microfibre with a diameter of 5 μm (the diameter of the uniform waist region) was fabricated by tapering a standard single mode optical fibre (SMF-28, Corning) using the same fabrication method as described in Section 2.1.2. The fabricated microfibre was bent into a U-shape to form a dipping probe as shown in Fig. 5.4, with a radius of curvature of 1.3–1.4 mm.

Several U-shaped probes were prepared with microfibres with different diameters to test the bend loss and structural stability. It was found that there was a tradeoff between the microfibre diameter and the bend loss of the U-shaped probe. Probes fabricated from microfibres with smaller diameters between 2–4 μm suffered from significant mechanical instability and this induced significant measurement errors in the system. They were also more likely to break when being immersed into the analyte solutions. Microfibres with larger diameters of 6–10 μm suffered from large bend loss when bent into the U-shape. The most suitable waist diameter was found to be circa 5 μm and this

diameter was selected to form the U-shaped probe to mitigate the tradeoff between instability and high bend loss.

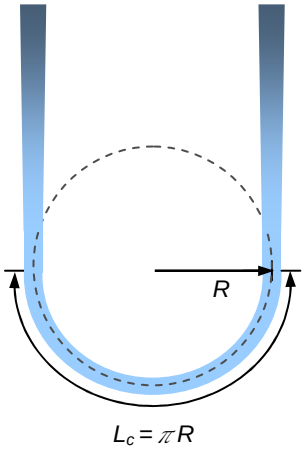

Figure 5.4: Schematic diagram of the U-shaped microfibre probe.

The length of the uniform waist region was controlled to be 4 mm by adjusting the microheater brushing length (as explained in Section 2.1.2). The length of the two transition regions was approximately 4.5 mm on each side. The fabricated microfibre was bent into a U-shape as shown in Fig. 5.4. The bend radius R was controlled to be circa 1.3–1.4 mm during experiments. Such a bend radius could ensure: (1) the curvature occurred within the uniform waist region of the microfibre. The length of the curved microfibre $L_c = \pi R$ and was calculated to be 4.08 mm for a bend radius of 1.3 mm. This value roughly equates to the length of the waist region of the microfibre (4 mm); (2) curvature induced bend loss was insignificant based on the discussion presented in [187] [188]. To experimentally confirm that this U-shaped microfibre configuration had a negligible bend loss, the transmission of the microfibre before and after it was bent was measured and was found to be negligible (less than 0.05 dB).

5.1.3 Nanoparticle immobilization

The U-shaped microfibre was fixed onto a vertical translation stage and immersed in a piranha solution for 1 hour to clean and also hydroxylate the microfibre surface. The piranha solution promotes the availability of hydroxyl surface functionality in the form of silanols on the microfibre surface. The piranha solution was prepared by mixing concentrated sulphuric acid and 30% hydrogen peroxide (v/v = 7:3). The sample was then rinsed with pure water. The next step was a silanization step, whereby the

inorganic fibre surface was coupled with organic PAH moieties. Silanol functional groups can be in the deprotonated state at neutral pH (reaction solvent water is approximately neutral) forming negatively charged anions (~SiO-). These form a strong electrostatic bond with the positive ammonium nitrogen cation in PAH, resulting in strong immobilization of PAH on the microfibre surface. In order to achieve a functionalized surface with more consistent coverage, PEM consisting of a (PAH/PSS)PAH trilayer instead of a PAH monolayer was deposited on the microfibre surface. This was achieved by immersing the hydroxylated microfibre subsequently in the aqueous PAH solution, PSS solution, and again PAH solution for 15 minutes. Both the PAH solution and the PSS solution had a concentration of 1 mg/ml. The average molecular weights of the PAH and the PSS were 65 kDa and 75 kDa respectively. The sample was rinsed with pure water in between these steps to remove the loosely bound PAH or PSS molecules.

Following the PEM treatment, the sample was immersed in an alloy nanoparticle colloid with a concentration of 1.28×10^{11} particles/ml. The nanoparticles which had a net negative charge adhered to the positively charged PAH top layer of the PEM during the immersion. The setup used for the microfibre hydroxylation, the PEM deposition and the nanoparticle immobilization was the same and is shown in Fig. 5.5. The inset magnified figure shows schematically the PEM-nanoparticle structure on the surface of the optical microfibre.

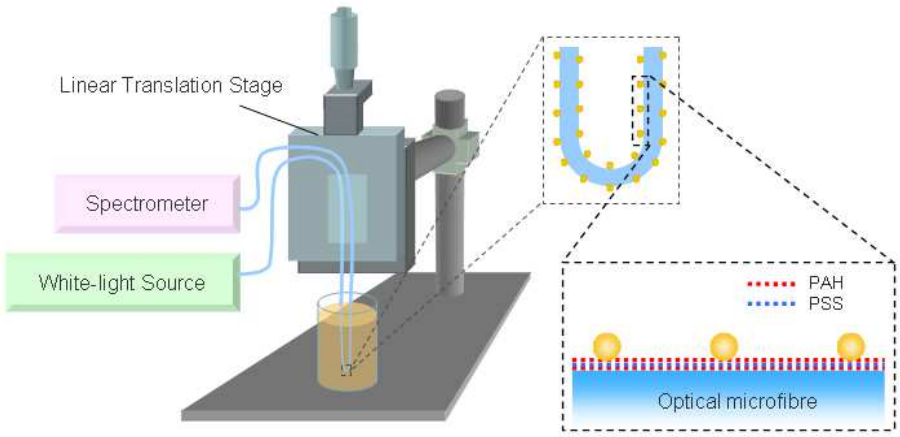

Figure 5.5: Schematic diagram of the setup for immobilizing nanoparticles. The U-shaped microfibre probe is fixed on a vertical translation stage and immersed in the colloidal nanoparticle solution.

The transmission spectra during the nanoparticle immobilization process were recorded. After nanoparticle immobilization, the sample was rinsed with deionized water and dried in air. Figure 5.6 shows an example of the absorption spectra of a 5 μm microfibre during the immobilization of 50%Au50%Ag nanoparticles. The unit of absorbance is absorbance unit (AU).

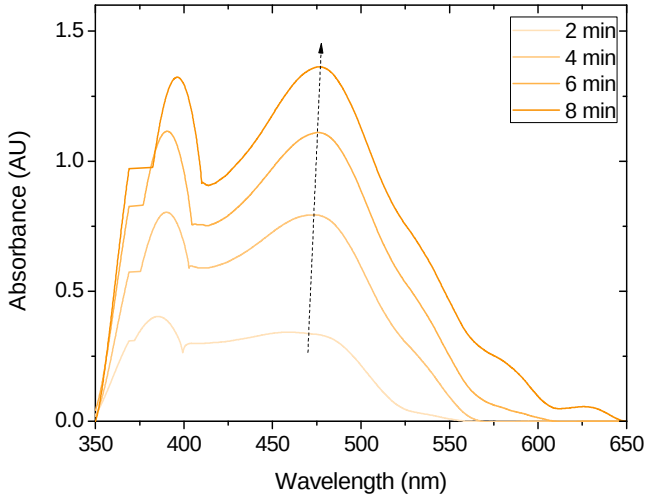

Figure 5.6: Absorption spectra recorded during an example of 50%Au50%Ag alloy nanoparticle immobilization. As the immobilization time increases, the absorbance increases and the LSPR peak becomes sharper.

The spectra are normalized to the (PAH/PSS)PAH modified microfibre (measured in water, without incorporating any nanoparticles). The spectra were measured by connecting the input and output ports of the microfibre to a tungsten-halogen white-light source (SLS201, Thorlabs) and a spectrometer (CCS100, Thorlabs) respectively. The absorbance increases and the LSPR band becomes sharper with the increase in the immobilization time due to the increasing surface density of the nanoparticles on the microfibre. The maximum absorbance occurred at the wavelength of approximately 476 nm.

5.2 LSPR effect in the presence of Au-Ag alloy nanoparticles

A series of 15 separate microfibre samples, each formed as a U-shaped probe, with immobilized 25%Au75%Ag, 50%Au50%Ag and 75%Au25%Ag nanoparticles were characterized using a field emission scanning electron microscope (FE-SEM) (SU6600,

Hitachi). Images were taken in a variable-pressure mode using back-scattered electron (BSE) detectors. Figure 5.7 shows the SEM images of surfaces of three selected microfibre samples individually immobilized with nanoparticles with different alloy formulations. The samples are labelled as A, B and C and correspond to microfibres immobilized with alloy nanoparticles with 25%Au75%Ag, 50%Au50%Ag and 75%Au25%Ag formulations respectively. The selection was based on samples that had similar levels of nanoparticle surface densities (analyzed using ImageJ software (NIH, USA)).

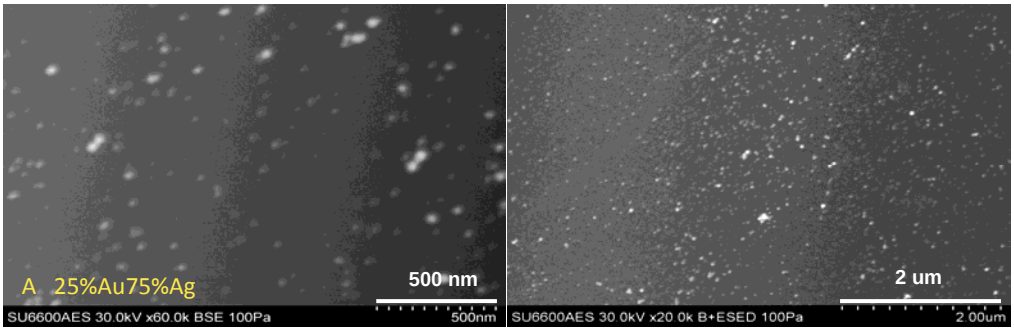

(a)

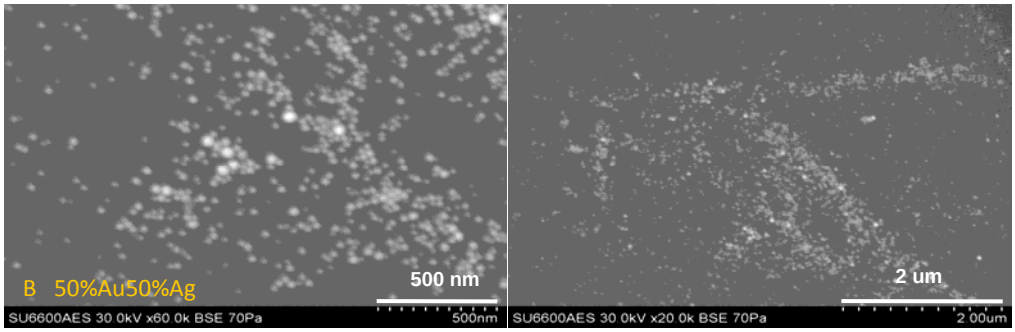

(b)

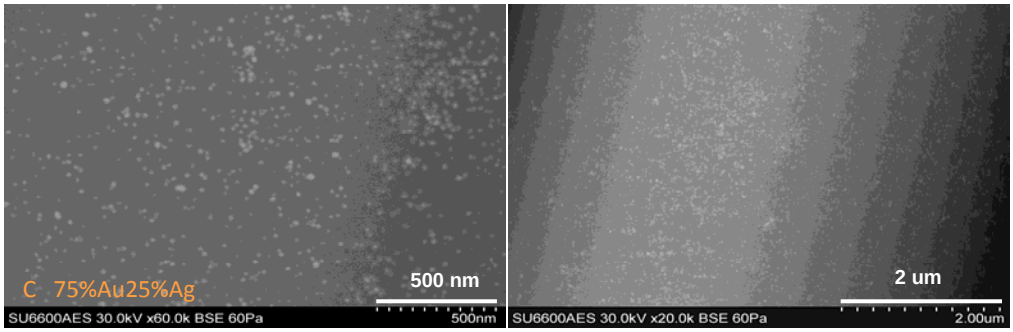

(c)

Figure. 5.7: FE-SEM images of microfibre surfaces with immobilized (a) 25%Au75%Ag, (b) 50%Au50%Ag and (c) 75%Au25%Ag nanoparticles.

Specifically, as listed in Table 5.1, sample A has the smallest value of surface density at 6.114%, followed by sample B at 7.737% and sample C at 8.52%. The images on the left side were taken at a magnification of 60000x and with an accelerating voltage of 30 kV. The images on the right side were taken at a magnification of 20000x and with an accelerating voltage of 20 kV. From the images in Fig. 5.7, it can be seen that nanoparticles are generally dispersed over the microfibre surface with few aggregations. However the nanoparticles show inhomogeneous distributions in some areas for sample B. This might be caused by an over charge of amine cation by the deposited PAH layer in these areas.

Table 5.1: Surface densities of the immobilized nanoparticles for the three studied samples.

Sample	Alloy formulation	Surface density (%)
A	25%Au75%Ag	6.1±2.6
B	50%Au50%Ag	7.7±4.0
C	75%Au25%Ag	8.5±2.6

5.2.1 LSPR wavelength

The absorption spectra for sample A, B and C were recorded using the same setup as demonstrated in Section 5.1.3 and are shown in Fig. 5.8. The wavelengths at which maximum absorbance occurred (referred to as LSPR wavelength) for sample A, B and C are approximately 456 nm, 463 nm and 492 nm respectively.

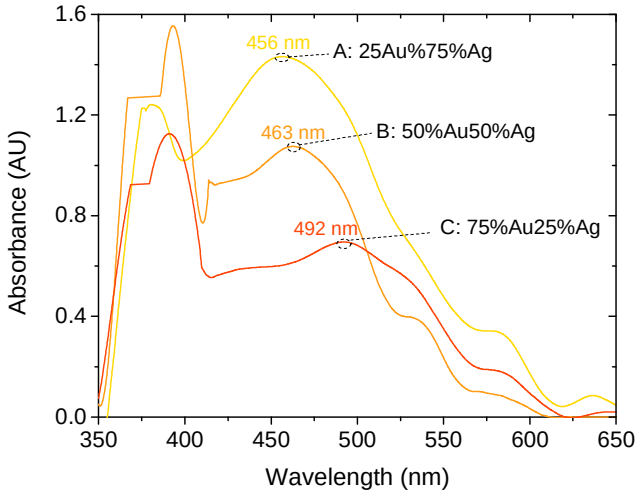

Figure 5.8: Absorption spectra for samples A, B and C with immobilized 25%Au75%Ag, 50%Au50%Ag and 75%Au25%Ag alloy nanoparticles.

One can see that the maximum absorbance wavelengths for the samples increase with an increase of Au content in the composition of the immobilized alloy nanoparticles. This result is in a good agreement with the spectra measured for bulk colloidal nanoparticles shown in Fig. 5.2. However the LSPR wavelengths observed for the immobilized alloy nanoparticles show slight redshifts compared with the bulk colloidal solutions. This could be caused by changes in the RI profile of the surrounding medium based on Equation 5.1. The spectra have relatively wide LSPR bands. For example the full width at half maximum (FWHM) for the spectrum of sample A is circa 65.5 nm.

5.2.2 LSPR absorption

Apart from different LSPR wavelengths, the three samples also show different LSPR absorption levels as shown in Fig. 5.8. The absorption spectra were measured immediately after the nanoparticle immobilization step while the sensor was surrounded by a water environment. This peak absorbance in water was measured for sample A, B and C and the results are listed in the Table 5.2.

Table 5.2: LSPR peak absorbances for the three studied samples. With similar surface densities, the three samples show alloy formulation dependent LSPR intensities represented by their peak absorbances.

Sample	Alloy formulation	Surface density (%)	LSPR peak absorbance (AU)
A	25%Au75%Ag	6.114±2.648	1.433
B	50%Au50%Ag	7.737±4.027	1.075
C	75%Au25%Ag	8.527±2.550	0.696

The three samples have similar levels of nanoparticle surface densities as previously shown in Table 5.1. However the LSPR intensity levels are different. Sample A (25%Au75%Ag alloy formulation) exhibits the highest LSPR intensity by showing the largest peak absorbance of 1.433 AU. In comparison, sample C (75%Au25%Ag alloy formulation) exhibits the lowest LSPR intensity by showing the smallest peak absorbance of 0.696 AU. Sample B (50%Au50%Ag alloy formulation) shows a medium level for both the nanoparticle surface density and the absorbance. One can see that samples with immobilized alloy nanoparticles which contain higher Ag content (lower

Au content) show stronger LSPR intensities and vice versa. The results are consistent with the well-known plasmonic phenomenon that silver nanoparticles show higher LSPR intensities than gold nanoparticles with the same geometry [15].

5.3 Sensing using microfibre with Au-Ag alloy nanoparticles

Many LSPR sensors are based on detecting RI variations caused by analytes in the vicinity of the nanoparticle surface. Therefore an important step is to determine the response to RI changes occurring in the local environment for a microfibre facilitated LSPR sensor. In this section, the sensitivities at detecting both bulk RI and surface RI changes are investigated and the results are compared for microfibres incorporating nanoparticles with different Au-Ag alloy formulations.

The term bulk RI refers to the RI of the aqueous medium surrounding the sensor probe. The LSPR fields of the nanoparticles are fully immersed in this bulk RI medium and any change in the bulk RI has an impact over the entire LSPR fields. In comparison, the term surface RI (as will be measured in the next subsection) refers to the RI of a nanometre-scale thin film (e.g. a molecular layer) formed on the surface of the nanoparticles. The thickness of this film is smaller than the decay distance of the LSPR fields. Thus changes in the surface RI mainly modify the LSPR field within a few nanometres of the nanoparticles' surface.

Since the LSPR fields generated by different alloy nanoparticles not only show differences in the total field power but also in the intensity distribution of the field, it is necessary to compare both the bulk and the surface RI responses for the proposed sensor.

5.3.1 Bulk RI sensing

In order to determine whether incorporating alloy nanoparticles on the surface of the microfibre increases the sensitivity of the sensor in detecting local RIs, the RI response of a bare optical microfibre without incorporating any nanoparticles was first measured. The microfibre was formed as a U-shaped probe as described in Section 5.2.2. The experimental setup for RI sensing is also the same as the setup used for nanoparticle

immobilization in Section 5.2.3. The U-shaped bare microfibre was immersed in a series of solutions of dimethyl sulfoxide in water with various calibrated RIs (1.333, 1.340, and 1.350). The absorption spectra of the bare microfibre probe were measured and normalized to the spectrum of the microfibre in water (RI = 1.333 @ 589 nm) and are shown in Fig. 5.9. The magnified regions of the spectra for the wavelength range of 450–500 nm are shown in the inset of the figure. The increase in the surrounding RI causes a general increase in the absorbance across the entire wavelength range. The sensitivity of the absorbance to the RI changes was calculated at a wavelength of 475 nm for the case without nanoparticles. The estimated sensitivity of such a bare microfibre in detecting surrounding RI changes was 1.19 AU/RIU.

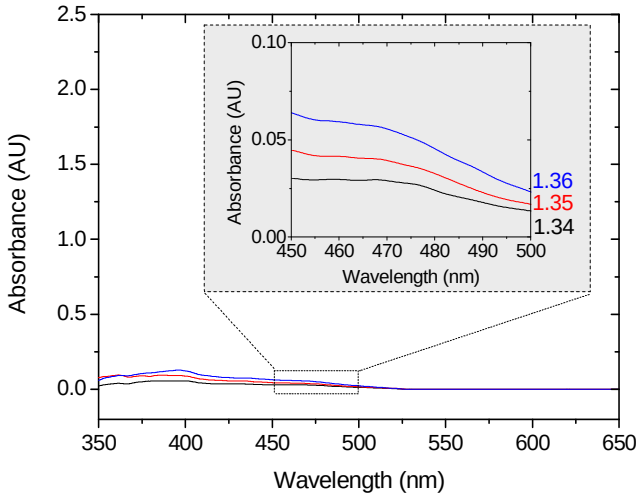

Figure 5.9: RI response for the microfibre without incorporating any nanoparticles on the surface.

The RI responses of microfibres incorporated with nanoparticles were then tested. In order to compare the sensitivities of the sensors with immobilized alloy nanoparticles of the same surface density but with different Au-Ag alloy formulations, three samples (labelled as sample A', B' and C') were prepared to have roughly the same absorbances as the samples A, B and C studied in Section 5.3. Thus it could be assumed that the three samples had similar surface densities of the immobilized nanoparticles. The RI responses of the samples were then measured using the same method as described in the first paragraph of this section. The maximum absorbances were controlled below circa 2.5 AU during the experiment since larger absorbances can result in poor signal-to-noise ratios.

The RI sensor results are shown in Fig. 5.10 (a) and (b) which presents the intensity changes and the spectral shifts respectively as the functions of surrounding RI. The solid lines are the linear fit of the mean of the measurements. The error bars in the figures represent the standard deviation of the repeated measurement results at each RI value. The discrepancies may be caused by the physical disturbance of the microfibre and the temperature fluctuation during the experiment. However the results still show a good repeatability of the samples in detecting local RI changes.

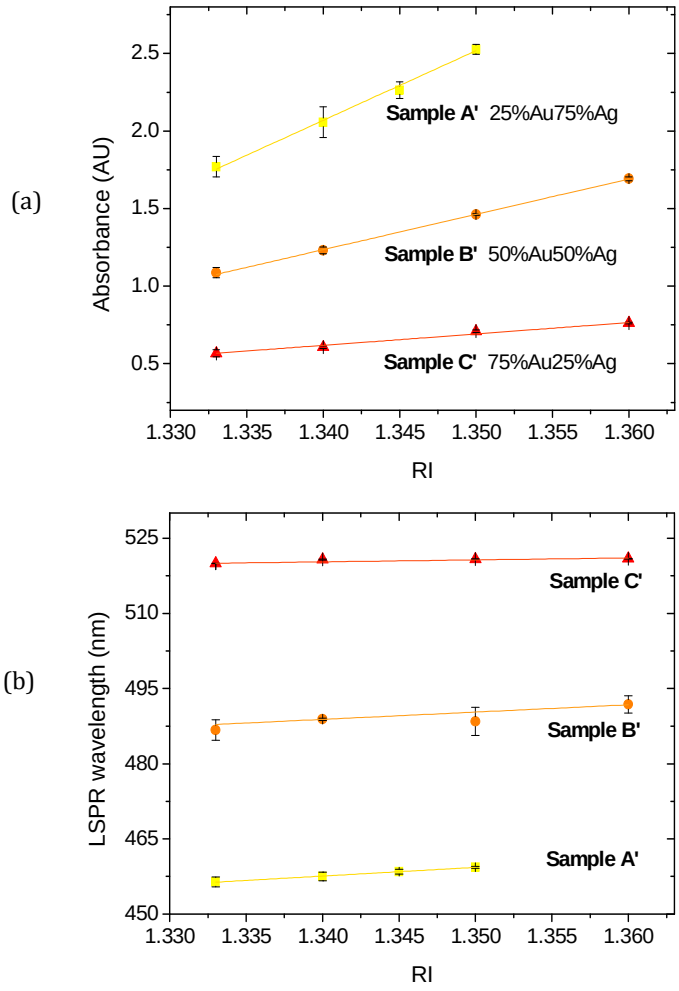

Figure 5.10: (a) LSPR peak absorbance vs. RI and (b) LSPR wavelength vs. RI for sample A', B' and C' which incorporates alloy nanoparticles with 25%Au75%Ag, 50%Au50%Ag and 75%Au25%Ag formulations respectively.

As shown in Fig. 5.10, all the three samples show increases in both absorbance and LSPR wavelength as RI increases. The sensitivities estimated from the experimental results in both the intensity and the wavelength domains are listed in Table 5.3. The samples with

higher Ag content exhibit higher sensitivities to RI and vice versa. This was expected since nanoparticles with higher Ag content are associated with stronger LSPR intensities by exhibiting larger peak absorbances as shown in Table 5.2. The highest sensitivities of 44.918 AU/RIU in the intensity domain and 173.6 nm/RIU in the wavelength domain were achieved for sample A' which had the highest Ag content.

Table 5.3: Sensitivities in detecting RI changes in the local aqueous environment for samples A', B' and C' in both the intensity and the wavelength domains. The three samples have similar nanoparticle surface densities. The RI sensitivity of the previously demonstrated bare microfibre is also provided for comparison.

Sample	Alloy formulation	LSPR peak absorbance (AU)	Sensitivity (AU/RIU)	Sensitivity (nm/RIU)
A'	25%Au75%Ag	1.696	44.918	173.600
B'	50%Au50%Ag	1.052	22.781	145.120
C'	75%Au25%Ag	0.540	7.357	38.639
Bare microfibre	N/A	N/A	1.19	N/A

As shown in the last row in the table, the studied bare microfibre showed a sensitivity of 1.19 AU/RIU in detecting local surrounding RI changes. This sensitivity is much lower than that of the samples which incorporated nanoparticles. This comparison of the RI sensitivity between the microfibres with and without alloy nanoparticles further confirmed that the light which originally propagated along the microfibre was coupled into the LSPR close to the nanoparticles' surface. Such an excitation of LSPR can significantly increase the sensitivity of the microfibre to the surrounding RI changes. It is worth noting that while in principle the sensitivity in the intensity domain achieved by the microfibre facilitated LSPR structures was a combined result of both the LSPR field of the nanoparticles and the evanescent field of the microfibres, in reality the LSPR played the dominant role since the sensitivity achieved by the evanescent field in detection was negligible.

5.3.2 Surface RI detection

In order to show the potential of the microfibre facilitated LSPR structure to work as a biochemical sensor, the sensitivity of the structure in detecting small surface RI changes

was also tested. This was done by altering the RI on the surface of the nanoparticles with the aid of additional adsorbed PEM. For this, a microfibre with immobilized alloy nanoparticles was immersed alternately in the PAH and PSS solutions for 15 minutes. The first layer of the cationic PAH molecules are most likely adsorbed onto the negatively charged nanoparticles' surface, thus encasing the nanoparticles and forming a monolayer due to the electrostatic attraction between the two. Then the anionic PSS molecules adsorb on to the PAH layer to cover the entire surface of the structure. PEM with required number of layers can be deposited on the surface of the structure by alternately repeating the deposition process using the PAH and PSS solutions. This molecular interaction mechanism resulted in a PEM-NP-PEM microstructure formed on the microfibre surface as shown in Fig. 5.11.

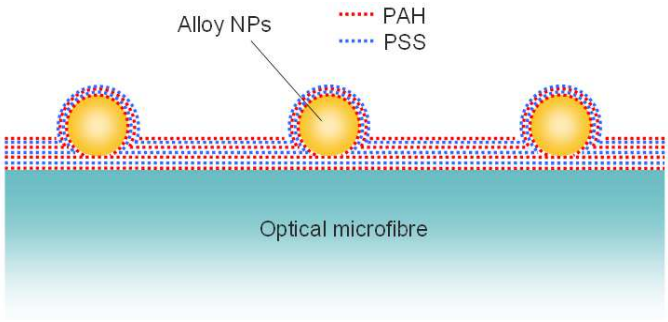

Figure 5.11: Schematic diagram showing the micro-configuration of the nanoparticles and the PEM on the microfibre surface. The nanoparticles were first immobilized on the (PAH/PSS)PAH modified microfibre surface. The nanoparticles were then alternately covered with PAH and PSS layers to test the surface RI sensitivity of the structure.

The absorption spectra of samples A', B' and C' after the deposition of each polyelectrolyte layer were measured. The analyzed results are shown in Fig. 5.12. The solid lines are the linear fits of the experimental data. The sensitivities in the intensity and the wavelength domains for the three samples are listed in Table 5.4.

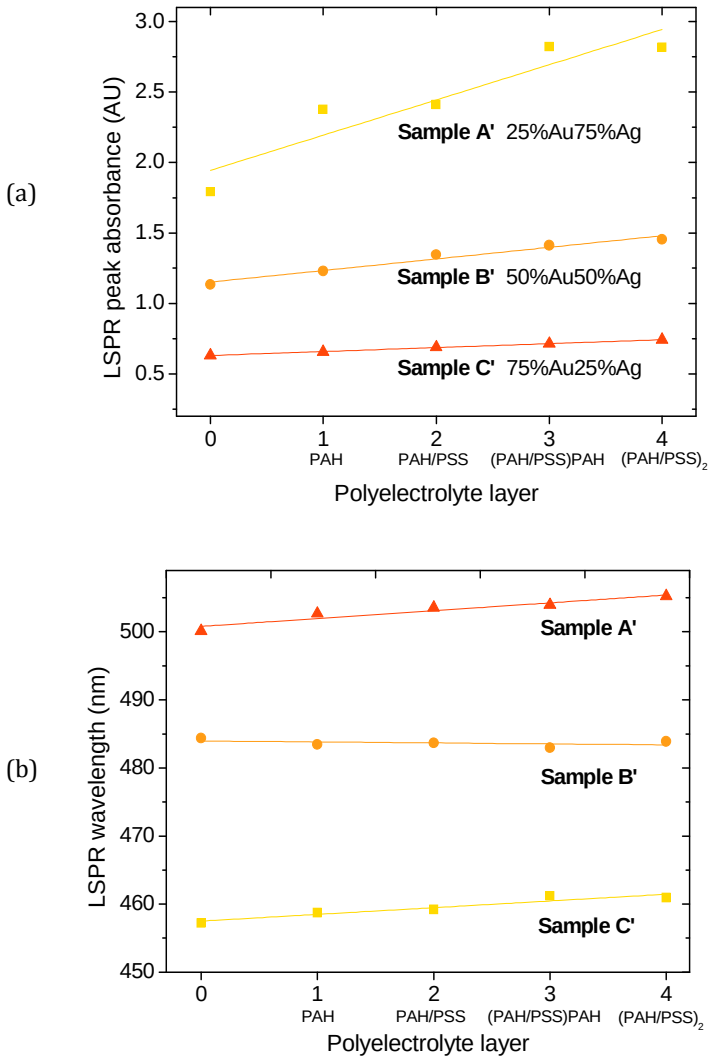

Figure 5.12: (a) LSPR peak absorbance vs. number of polyelectrolyte layer and (b) LSPR wavelength vs. number of polyelectrolyte layer for samples A', B' and C' which incorporate alloy nanoparticles with 25%Au75%Ag, 50%Au50%Ag and 75%Au25%Ag formulations respectively.

In the intensity domain, increases in the number of adsorbed polyelectrolyte layers increases the absorbance with a slope of 0.250, 0.082 and 0.028 AU/layer for samples A', B' and C' respectively. In terms of the influence of nanoparticles' alloy formulation, the results agree well with those achieved in the bulk RI sensing experiment by exhibiting an increasing sensitivity for the alloy nanoparticles with higher Ag (lower Au) content. However the wavelength domain sensitivities failed to show any clear correlation with the nanoparticles' composition. Sample B' even shows blueshifts in the absorption spectra with increasing RI which conflicts with established LSPR theory. The unexpected blueshifts might result from the poor signal-to-noise ratio associated with the

wavelength domain detection and thus errors can obscure the true analyte induced spectral shifts. For example, typical LSPR spectral peaks are broad (FWHM> 65 nm as demonstrated in Section 5.2.1) compared with spectral shifts caused by the presence of each subsequent polyelectrolyte layer (circa 1 nm as shown in Table 5.3). Therefore measurement of small surface RI changes based on the detection of absorbance variations rather than wavelength shifts using the studied microfibre facilitated LSPR structure is a more accurate and reliable method.

Table 5.4: Sensitivities in detecting PEM deposited on the surface of the nanoparticles for samples A', B' and C' in both the intensity and the wavelength domains. The three samples have similar nanoparticle surface density.

Sample	Alloy formulation	Sensitivity (AU/ layer)	Sensitivity (nm/ layer)
A'	25%Au75%Ag	0.250	0.988
B'	50%Au50%Ag	0.082	-0.140
C'	75%Au25%Ag	0.028	1.152

The typical thickness of a PAH/PSS bilayer is in the range of 0.5–2 nm depending on factors such as concentration and pH of the PAH and PSS solutions [189]. Thus the microfibre facilitated LSPR structure using alloy nanoparticles should be able to work as a biosensor in the intensity domain. The structure should be able to detect biochemical molecules captured onto the nanoparticles' surface given the fact that the sizes of most biomolecules are larger than 2 nm.

5.3.3 General comparison of RI sensing results

In the last two sections, the RI responses for microfibres incorporated with nanoparticles which have roughly the same surface densities but different Au-Ag compositions were compared. The results showed that samples with immobilized alloy nanoparticles containing higher Ag (lower Au) content generate LSPR with higher intensities. Such samples with higher Ag-content also showed higher sensitivities in detecting surrounding RI changes. In this section, the sensitivities of microfibre facilitated LSPR sensors incorporating nanoparticles with different Au-Ag formulations are compared in a more comprehensive way. For each type of nanoparticle, several samples which achieved different peak LSPR intensities were compared in terms of their

sensitivities to local RI changes. The LSPR peak intensities of the samples are reflected by their peak absorbances measured in a water environment. For each alloy composition, three or four samples prepared with different peak absorbances were used to measure local RI changes. The sensitivities achieved by the samples were evaluated and then plotted against the samples' LSPR peak absorbances. Due to the poor quality of results in the wavelength domain achieved in the previous RI sensing experiments, only the intensity domain measurements were analyzed in this experiment.

The results are shown in Fig. 5.13 (a). The zero absorbance data corresponds to the bare microfibre's sensitivity at detecting RIs (as shown in Table 5.3). One can see that for all three alloy compositions, the sensitivity in detection increases with the sample's LSPR peak absorbance measured in water. This means, that with all other parameters fixed, higher LSPR intensities result in higher sensitivities to RI changes. Also, as demonstrated earlier, alloy nanoparticles with a higher Ag content show higher sensitivity when the surface densities are the same. However, when samples with different alloy formulations of nanoparticles achieve similar peak absorbance levels, samples incorporating nanoparticles with a higher Au content (which essentially means those samples have much higher nanoparticle surface densities than the samples incorporating alloy nanoparticles with a higher Ag content) are associated with higher sensitivities.

A similar investigation was carried using the same methodology to compare the sensitivities in detecting PEM deposition on the nanoparticles' surface. The results are shown in Fig. 5.13 (b). Compared with detecting bulk RI changes, the sensor showed a similar alloy formulation dependent sensitivity in detecting surface RI changes. However, samples which incorporated 75%Au25%Ag alloy nanoparticles showed a trend towards a more drastic increase in sensitivity with the increase in peak absorbance compared with the other two alloy formulations. One possible explanation is that when achieving similar peak absorbance levels, samples with 75%Au25%Ag alloy nanoparticles essentially need to have higher surface densities than samples with the other two alloy formulations of nanoparticles. As a result, a larger amount of the PAH molecules (positively charged) can be attracted by nanoparticles (negatively charged) onto their surfaces and result in a larger increase in the local surface RI.

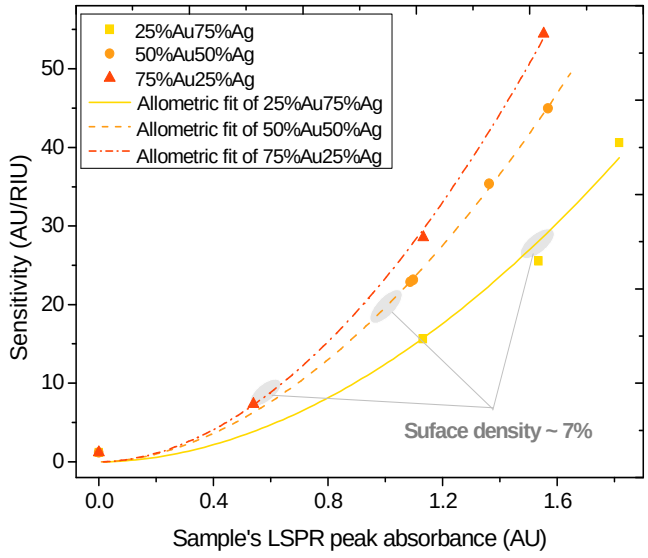

(a)

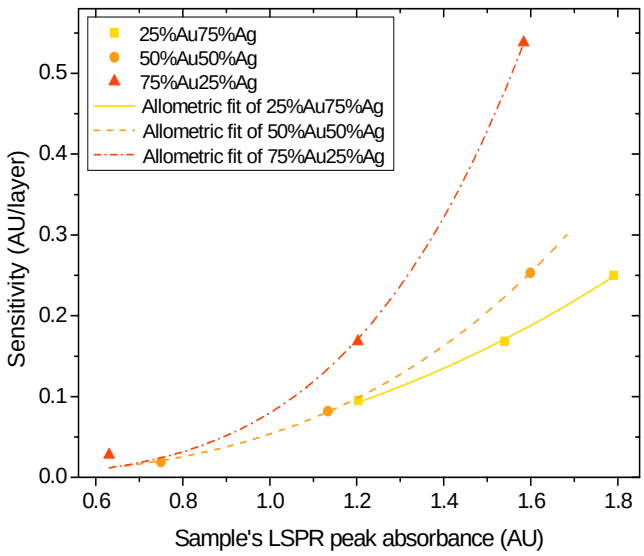

(b)

Figure 5.13: (a) Sample's LSPR peak absorbance (measured when the sample is in water environment) vs. sensitivity at detecting (a) bulk RI changes and (b) PEM deposited on the nanoparticles' surface.

5.4 The effect of microfibre diameter

Based on the results presented so far, it was found that the sensitivities achieved by the microfibre facilitated LSPR structure which incorporates Au-Ag alloy nanoparticles are competitive with the existing optical fibre facilitated LSPR sensors [116][190]. However

the microfibre facilitated LSPR sensors can potentially provide an extra advantage compared with the conventional optical fibres (e.g. conventional decladded optical fibre) facilitated LSPR sensors. The nanoparticle surface densities required for a microfibre facilitated LSPR sensor are also smaller than those required for covering the surface of a conventional optical fibre in order to achieve a similar level of LSPR intensity. This is because the evanescent fields which work as the incident light to generate LSPR are larger for microfibres than those for conventional decladded optical fibres. Given the fact that the intensity of the excited LSPR is proportional to that of the incident light [191], the LSPR generated by each nanoparticle immobilized on a microfibre should be stronger than that generated by each nanoparticle immobilized on a conventional decladded optical fibre.

This low nanoparticle surface density requirement for microfibre facilitated LSPR sensor can be potentially useful in biosensing. For a typical LSPR biosensor, the target analyte is recognized by the specific receptors functionalized on the surface of nanoparticles. The number of the receptors immobilized on the surface of each nanoparticle is limited. In addition, the concentration of the target analyte is usually small. Thus only a limited number of target molecules can be captured by the receptors and in turn modify the LSPR field. To illustrate this consider the case where two single target molecules are separately captured by a microfibre LSPR sensor and a conventional optical fibre LSPR sensor. The microfibre LSPR sensor should be able to detect the molecule with a higher sensitivity since the LSPR modified by the molecule is more substantial compared with the conventional optical fibre LSPR sensor.

This potential advantage can be further enhanced by reducing the diameter of the microfibre. The diameters of the microfibres used to facilitate LSPR in the experiments reported earlier in this chapter are 5 μm which is relatively large. If the diameter is reduced to smaller values, the nanoparticle surface density required to achieve the same level of LSPR intensities should be even smaller. As an example, a microfibre sample which had a diameter of 2.5 μm and was immobilized with 50%Au50%Ag alloy nanoparticles was studied. The sample had an in-water-absorbance of circa 1.2. The surface of the microfibre incorporating nanoparticles was characterized using the FE-SEM and the image is shown in Fig. 5.14.

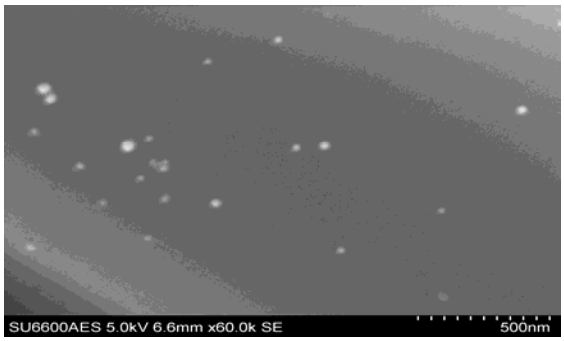

Figure 5.14: FE-SEM image showing 50%Au50%Ag alloy nanoparticles immobilized on the surface of a microfibre with a diameter of 2.5 μm. The nanoparticle surface density is roughly 1.6 %. The in-water-absorbance was 1.2 AU.

The nanoparticles were analyzed using ImageJ. The nanoparticle surface density and the corresponding peak absorbance of this sample (labelled as D) are compared with sample B studied in Section 5.3. The corresponding results are listed in Table 5.5 for comparison. The sample D has a slightly higher peak absorbance than sample B. However the nanoparticle surface density of sample D is only one fifth of that of sample B. This comparison shows that the efficiency at generating LSPR can be improved by reducing the diameters of the engaged microfibres. As pointed out in the first two paragraph in this section, the disadvantage of using microfibres with smaller diameters is that the fabricated sensors can suffer from poor mechanical strength and stability. For this reason microfibres with a relatively large diameter of 5 μm have been used for the investigation described in this thesis.

Table 5.5: Comparison between nanoparticle surface densities required to achieve similar levels of LSPR intensities by two microfibre samples with different diameters.

Sample	Alloy formulation	Microfibre diameter (μm)	Peak absorbance (AU)	Surface density (%)
B	50%Au50%Ag	5	1.075	7.737±4.027
D	50%Au50%Ag	2.5	1.2	1.604±0.429

5.5 pH sensing using microfibre facilitated LSPR structure

Applications in numerous fields such as biomedical research, clinical analysis, environmental monitoring and food processing require fast and accurate detection of pH.

Several optical fibre pH sensors have been developed by coating pH sensitive polymers such as hydrogels [192], sol-gels [193] and self-assembled PEM [194] onto the surface of optical fibres. In recent years, pH sensors have also been demonstrated using tapered optical fibres with the intention of achieving detection with a higher sensitivity and a faster response [195][196]. Very recently, a pH sensor based on optical fibre facilitated LSPR effects was developed by Tou et al [197]. The optical fibre structure consisted of a section of photonic crystal fibre (PCF) spliced in between two multimode fibres (MMF). By incorporating a coating of gold nanoparticles, followed by a coating of PEM on the fibre surface, the structure was able to detect a pH range of 6.5–8.0.

It has been shown in previous sections that using tapered optical microfibres to facilitate the generation of LSPR can show enhanced sensitivities in detecting surface RI changes. Since PEM can be pH sensitive, the previously introduced PEM-NP-PEM nanostructure formed on the surface of a microfibre can be utilized for pH sensing. Such a pH sensing configuration which embraces the advantages of optical microfibre, LSPR and PEM has the potential to achieve better performance than the existing polymer based optical fibre pH sensors. In this section, the potential for the microfibre facilitated LSPR structure to work as a novel pH sensor is experimentally demonstrated by forming a PEM-NP-PEM nanostructure on the surface of a 5 μm diameter microfibre.

5.5.1 pH-induced swelling of PEM

The mechanism of the forming of layer-by-layer (LbL) self-assembly PEM was introduced previously in Section 4.2 and is not repeated here. The thickness of the formed PEM depends on the charge density of each polyelectrolyte layer. Higher charge densities result in stronger electrostatic interactions between the polyelectrolyte layers and thus the PEM become thinner, and vice versa. This results in an increase in the local RI and thus the absorption of the nanoparticles. Many factors can affect the charge density, such as salt concentration and the pH of the surrounding solution [198]. For example, PAH/PSS multilayers normally hold the highest charge density around a neutral pH and thus are the thinnest [193]. As the pH increases or decreases the PEM expands and become thicker. As the pH returns back to neutral, the PEM shrinks and recover to its original thickness. The operating principle of a PEM based pH sensor relies on this pH induced charge density variation and the consequent reversible swelling and shrinking behaviour of the polyelectrolytes.

It should be noted that the use of PEM as the pH-sensitive polymer is essential in this work. Although many polymers such as hydrogels and sol-gels [199], are also pH sensitive and can be deposited on the sensing structures using conventional coating methods such as radiation or chemical induced attachment of films, it is difficult to precisely control the thickness and evenness of the film. Precise control over the thickness and evenness of the pH-sensitive polymer films is essential for a microfibre and nanoparticle facilitated LSPR sensing configuration. This is because the LSPR fields of nanoparticles decay rapidly within a distance of tens of nanometres. Thus the pH-sensitive polymer film formed on the nanoparticles' surface needs to be highly confined (of nanometre thickness) and uniform in thickness for the sensor to work. Layer control is also important to ensure repeatable sensor performance. The LbL technique used in this thesis is a versatile and convenient approach to form such highly uniform PEM films on substrates with precisely controlled thicknesses. The substrates can be non-flat surfaces of any shape which makes this technique even more suitable to form self-assembled PEM on the spherical surfaces of the nanoparticles, which themselves are deposited on the curved surface of the microfibre.

5.5.2 pH sensing experiment and results

The pH sensing structure is very similar to the microfibre-PEM-NP-PEM configuration shown in Fig. 5.11. The experimental detail of preparing the configuration is the same as demonstrated in Section 5.3.2 and thus is not repeated here. For simplicity only the median alloy formulation of 50%Au50%Ag nanoparticles was used to demonstrate the pH sensor. The nanoparticles were immobilized on the (PAH/PSS)PAH modified microfibre surface to achieve a peak absorbance of circa 1.0 AU. Then three layers of PAH/PSS bilayers were deposited on top of the nanoparticles to form a NP$(PAH/PSS)_3$ multilayer system. After the deposition of PEM the sensor had a peak absorbance of 2.40 RU at 492.65 nm.

The experimental procedure involved the fabricated sensor being dipped into aqueous solutions with various calibrated pH values ranging from 2.0 to 10.0. The pH solutions were prepared by mixing HCl or NaOH with pure water with various concentrations. Only a very small amount of HCl or NaOH is required to achieve a large pH difference of the solution. One possible concern was that the different liquid formulations of HCl or

NaOH and water could have different RIs that might confuse results when trying to measure the pH of the liquids. To eliminate this concern the RIs of the calibrated pH solutions were measured using an Abbe refractometer (ABBE5, Bellingham+Stanley). The RI difference between the highest HCl (or NaOH) solution and pure water was only 0.001. This suggests that the effect of RI variations during the pH measurements can be neglected.

The LSPR absorption spectra of the sensor in various pH solutions were measured and analyzed using the same setup as described in previous sections. The absorption peak of the sensor was located at circa 496.25 nm. The absorbances at this wavelength when the sensor was immersed into different pH solutions were measured. For each measurement, the sensor was immersed in the pH solutions for 1 minute before the absorption spectrum was recorded. This allowed the PEM to fully swell/shrink and thus to achieve a stabilized absorption spectrum. Each measurement was repeated three times. The pH induced swelling and shrinking process is reversible. Therefore the repeated measurements were carried out using the same sensor sample. The relationships between the measured absorbance at 492.65 nm and the pH are shown in Fig. 5.15.

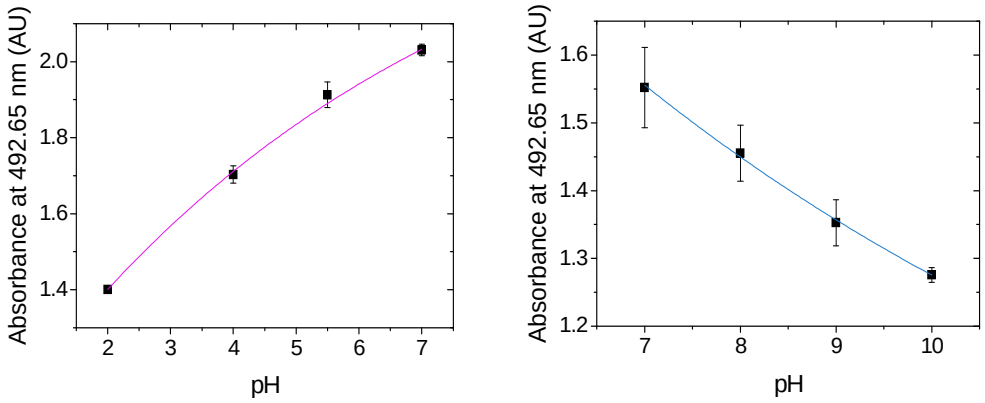

Figure 5.15: pH response of the microfibre-PEM-NP-PEM structure for (a) acidic pH range and (b) alkaline pH range. The absorbance was measured at 492.65 nm. The error bars represent the standard deviation of the measurements. The solid lines are the exponential fit of the mean of the measurements.

As shown in Fig. 5.15 (a), the absorbance of the sensor decreases for the more acidic pH values for the surrounding aqueous environment. On the contrary, the absorbance

decreases with increasing pH in an alkaline environment as shown in Fig. 5.15 (b). The results correspond well with the fact that PAH/PSS multilayers are strongly charged at neutral pH and where the PEM are the densest with the highest RI.

There is a large intensity mismatch between the original peak absorbance and the absorbance when the surrounding aqueous environment is returned to the neutral pH from the alkaline environment. This could be caused by the incomplete shrinking of the PEM. The kinetics behind the pH related mobility and swelling behaviour of the PEM are complex and is outside the scope of this thesis and are not discussed further.

In general, the proposed structure shows a pH dependent absorption in both the acidic and alkaline aqueous environments. Based on the higher sensitivity available, the structure is more suitable for detection of pH changes in an acidic to neutral range environment from 2 to 7. The average pH sensitivity was circa 2.6 AU/pH within this pH range. As a proof of principle only the structure based on alloy nanoparticles with a composition of 50%Au50%Ag was studied in this work. However the properties and performance of such a potential pH sensor can be easily tuned by incorporating Au-Ag alloy nanoparticles with other formulations based on the results shown in Sections 5.3 and 5.4.

5.6 Conclusions

In this chapter, a microfibre facilitated LSPR sensing configuration which incorporates Au-Ag alloy nanoparticles was experimentally demonstrated. The sensor was fabricated by immobilizing alloy nanoparticles on a (PAH/PSS)PAH modified microfibre surface. The LSPR effects and sensing performances of a range of samples incorporating nanoparticles with a certain Au-Ag composition were compared. The comparison of the LSPR effects showed that, with roughly the same nanoparticle surface density, nanoparticles with different alloy formulations result in different LSPR intensities and resonance wavelengths. Nanoparticles with higher Ag content showed shorter resonance wavelengths and stronger LSPR intensities and vice versa.

Next, the performance of the microfibre facilitated LSPR structure at detecting surrounding RI changes for nanoparticles with different alloy formulations was compared. Both the bulk and the surface RI sensing results showed that with similar

nanoparticle surface densities, nanoparticles with higher Ag content were more sensitive in both the intensity and wavelength domains. However the wavelength domain resolution was low which suggested that the sensor was more suitable to work in an intensity domain. When comparing the sensitivities of samples which incorporated different alloy nanoparticles but with similar LSPR intensities, samples with higher Au content show higher sensitivities. The achieved sensitivities are comparable with the existing optical fibre based LSPR sensors. However the nanoparticle surface densities required for a microfibre facilitated LSPR sensor are smaller than those required for covering the surface of a conventional optical fibre in order to achieve a similar level of LSPR intensity. This advantage can be further enhance by using microfibres with even smaller diameters. However the use of thinner microfibres is limited by their mechanical instability.

Finally the potential for the microfibre facilitated LSPR structure to work as a pH sensor was demonstrated by depositing PEM on top of the immobilized nanoparticles. The sensor showed different pH-dependent LSPR responses in acidic and alkaline environments. The sensor is more sensitive for the detection of pH within the range of pH 2–7.

Chapter 6

Conclusions

Tapered optical microfibres have large and easily accessible evanescent fields to facilitate strong light environment interactions. Optical microfibres also have highly confined mode distribution and small diameters to form compact structures with low bend loss. As a result, tapered optical microfibres have the potential for developing sensors with high sensitivity, fast response, small size and low cost. This thesis explored the sensing potential of tapered optical microfibre based structures in several application fields. This chapter briefly summarizes the output of the research reported in this thesis and draws a number of specific conclusions and furthermore proposes several potential research directions into which the current work can be extended.

6.1 Summary and conclusions

This section summarizes the main contributions and conclusions of the research work reported in this thesis. A complete microfibre fabrication setup was first designed and implemented as a key prerequisite to carry out the research. Both single microfibre and OMC tapered structures were investigated as the basis of sensors such as an RI sensor, a biosensor, a humidity sensor and a pH sensor. Specific contributions include:

- **A microfibre fabrication setup.** A microfibre fabrication setup was designed and developed as a key prerequisite for the research and this was described in Chapter 2. The fabrication setup involved using a ceramic microheater to heat the optical fibre and two motorized translation stages to stretch the fibre. A tapering motion control

program for a PC was developed to automate the fibre tapering process and to allow a user to precisely control the shape and diameter of the fabricated optical microfibres. The developed setup allows for the fabrication of microfibres with an acceptable level of taper diameter control and good repeatability. The discrepancy between the predicted diameters and the actual diameters was less than 10%. The setup could also be adapted to fabricate OMC structures.

- **An OMC based RI sensor.** Chapter 3 demonstrated a RI sensor using an OMC structure. An OMC was chosen as the tapered fibre structure as it offers the advantages that it can be interrogated in the wavelength domain and is relatively easy to fabricate. An OMC with a diameter circa 2 μm (that is the diameter of each microfibre) was fabricated using the fibre tapering setup developed and described in Chapter 2. The fabricated OMC exhibited a multi-peak interference spectrum with a maximum extinction ratio of over 25 dB. When used for detecting the RI of the surrounding aqueous environment, the OMC achieved an average sensitivity of 2737 nm/RIU with a maximum sensitivity of 4155 nm/RIU for a RI value close to 1.334. However the OMC showed strong spectral dependence on the polarization state of the input light. Therefore it is concluded that a polarization controller would need to be incorporated in a usable sensing system to control the input polarization state to achieve higher sensing resolution and to minimize the polarization induced measurement error (e.g. due to bending induced polarization disturbance of fibre cables during experiments). The temperature and humidity dependences of the OMC were also studied. The OMC showed a limited linear temperature dependence in the order of a picometre scale wavelength shift per degree. It was also found that high humidity levels of over 90% RH could significantly affect the coupling behaviour of the OMC, leading to increased measurement errors. The sensor is thus best suited to relatively low humidity environments to avoid the need for humidity compensation.

- **An OMC based humidity sensor.** Chapter 3 also described an experimental demonstration of a humidity sensor based on the OMC structure. The sensor was fabricated by coating an OMC with a layer of humidity sensitive PEO material. The sensor could detect RH changes in the range from 70% RH to 85% RH with an average sensitivity of 2.23 nm/%RH. This sensitivity is comparable with the existing fibre optic based humidity sensors. Since the described humidity sensor showed significant spectra shifts and thus large optical intensity variations within 70% – 85%

RH range, the sensor can be used as a humidity dependent optical switch to limit RH to levels below or above this RH range. Such humidity switches are useful in many agricultural, cosmetic and clinical applications.

- **An OMC based label-free immunosensor.** Chapter 4 experimentally demonstrated a label-free immunosensor based on a packaged OMC structure. A key prerequisite was that the OMC is packaged in a low RI UV curable polymer to achieve good mechanical stability of the structure during measurement. The principle and operation of the immunosensor was demonstrated using fibrinogen antigen-antibody pairing. The results showed that such an OMC based immunosensor was capable of detecting the specific binding between the fibrinogen and the anti-fibrinogen. It was found that the detected signal was proportional to the concentration of the anti-fibrinogen solution. Chapter 4 also included a description of a more clinically relevant IgG sensor by immobilizing anti-IgG on the surface of the OMC sensing region. The results showed that the sensor could also detect the specific binding between anti-IgG and the IgG. The demonstrated OMC based biosensor offers a reliable, compact and simple solution for implementing current immunoassays.

- **A microfibre based LSPR sensor incorporating Au-Ag alloy nanoparticles.** Chapter 5 included a description of the experimental demonstration of a microfibre based LSPR sensor which incorporated Au-Ag alloy nanoparticles. The sensor was fabricated by immobilizing Au-Ag alloy nanoparticles on a (PAH/PSS)PAH modified tapered single microfibre surface. The LSPR effects and the sensing performance of several sensor samples incorporating nanoparticles with different Au-Ag formulations were compared. It was concluded that the sensors which incorporated nanoparticles with a higher Ag (lower Au) content showed stronger LSPR intensities and higher sensitivities in detecting bulk and surface RIs in both the intensity and the wavelength domains. It was also concluded that when the samples with a different nanoparticle alloy formulation exhibited similar LSPR intensities, samples with a higher Au content (which essentially means that those samples have higher nanoparticle surface densities) showed a higher sensitivity in detection. A further conclusion was that the sensors were more suitable for operating in the intensity domain since the achievable resolution in the wavelength domain was low. Based on the results, the performance of the microfibre based LSPR based sensor could be potentially tuned by varying the Au-Ag formulation of the nanoparticles. The

biochemical properties of the sensor could also be tuned based on the well-known physicochemical differences between Au and Ag for potential applications in antibacterial biomedications, drug-delivery, and tumour thermotherapy.

- **A pH sensor**. As an example of a practical sensor, Chapter 5 also demonstrated the potential for microfibre based LSPR structure to work as a pH sensor. The sensor was fabricated by depositing PEM on top of the 50%Au50%Ag alloy nanoparticles that were immobilized on a microfibre surface. The formed PEM-NP-PEM nanostructure on the microfibre surface showed pH dependent swelling and shrinking behaviour which in turn modified the detected LSPR intensity of the sensor. The LSPR absorbance of the sensor increased with the pH in an acidic environment and decreased with the pH in an alkaline environment. Thus the sensor could be used to detect the pH level of either an acidic solution or an alkaline solution. However the sensor showed a higher sensitivity and a smaller measurement error in the acidic situation. It was concluded that this microfibre based LSPR pH sensor was better suited to detect pH levels of 2–7, achieving an average sensitivity of 2.6 AU/pH.

6.2 Global conclusions

Beyond the specific conclusions mentioned above, there are several global conclusions of the research reported in this thesis that are worth highlighting:

- An OMC is a relatively simple and efficient microfibre structure for developing sensors with potential high performance given its easily accessible evanescent fields and RI dependent coupling coefficients. The wavelength dependent multi-peak transmission spectra of the OMC structure can facilitate wavelength domain interrogation for detection which overcomes the necessity of using overly thin microfibres in order to achieve the strong light-environment interaction needed for intensity domain detection. The tradeoff is that fabricating an OMC requires fusing two tapered optical microfibres together to form the coupling structure, but on a positive note because the fusing of the two fibres in an OMC occurs at the same time as tapering, as mentioned in Section 3.2. Therefore the actual real increase in fabrication complexity and time consumed in doing so is modest and is worthwhile in many applications which would benefit from wavelength domain interrogation.

- Utilizing the potential high sensitivity in detecting surrounding RI changes for the OMC structure, OMCs can be successfully adapted to form the basis of a wide variety of sensors for a diverse range of measurands. As examples, a humidity sensor and a label-free immunosensor were developed by functionalizing an OMC surface with a humidity sensitive coating and with bioreceptors respectively. The diversity demonstrated suggests that OMCs offer a means to implement a range of other evanescent field sensors, provided that suitable functionalization can be implemented.

- The sensitivity in detection for a single microfibre with a relatively large diameter , which has the benefit of being more mechanically robust, can be enhanced by incorporating conductive nanoparticles on the microfibre surface. The evanescent fields of the microfibre can be efficiently coupled into LSPRs of the nanoparticles to facilitate biochemical sensing applications. The improvement in sensitivity is at the expense of a more complex surface functionalization. Whether this added complexity is worthwhile will depend on the sensitivity and application required and on the level of mechanical robustness demanded by the application.

- Using Au-Ag alloy nanoparticles which contain different alloy formulations show different LSPR effects and sensing performance. Thus sensors with potentially tunable characterization can be developed. The alloy nanoparticles also provide extra advantages of combining the merits of both gold and silver allowing one to potentially tailor the physicochemical properties of the sensor. However the tuning is not dynamic,since the tuning arises from an alloy formulation which can altered to tune the sensor during design and fabrication but not when the sensor is in use.

6.3 Future work

While this thesis explored the potential of microfibres for sensing applications, there remain a number of unanswered research questions and challenges which point to promising directions that current work could be extended into.

- **OMC based sensors using polarization maintaining optical fibres.** An OMC structure is sensitive to polarization state of the input light as demonstrated in

Chapter 3. A tapered polarization maintaining (PM) optical microfibre fabricated by adiabatically tapering a conventional PM optical fibre was shown by Jung. et al. [130] to be capable of maintaining linear polarization states. Thus using PM optical fibres instead of standard single-mode optical fibres to develop OMC based sensors points to a possible approach to minimize polarization induced system instability and related sensing errors.

- **Biosensors using microfibre based LSPR effects.** In Chapter 5 it was shown that a microfibre based LSPR sensor could surface RI changes caused by adsorbed PEM. It was also demonstrated that by incorporating alloy nanoparticles with higher Ag content or using microfibres with smaller diameters, the sensor could exhibit high intensity LSPR with relatively small nanoparticle surface densities. This effect was exploited to enhance the biosensitivity in detecting very small concentrations of a target analyte captured by a limited number of receptors immobilized on the nanoparticles, as explained in Section 5.5. It is of clinical significance to investigate the performance of such a microfibre based LSPR biosensor using high-Ag content alloy nanoparticles and small-diameter microfibres. For example, by immobilizing alloy nanoparticles that are functionalized with anti-epidermal growth factor receptor (anti-EGFR) antibody onto the microfibre surface, the sensor can detect EGFR and provide useful information for cancer diagnostics.

- **OMC based LSPR sensor.** An OMC exhibiting a wavelength dependent multi-peak transmission spectrum was described in Chapter 3. The spectrum showed high RI sensitivity and a capability for biosensing with wavelength domain interrogation, as demonstrated in Chapter 4. In comparison with the OMC's wavelength domain detection, a microfibre based LSPR sensor showed a strong intensity dependence but a relatively small wavelength dependence on environmental changes as demonstrated in Chapter 5. A key question is what if the mode-coupling of an OMC structure is combined with nanoparticles' LSPR effects? Is it possible to develop sensors with new potentials such as to simultaneously detect two environmental changes with low cross sensitivity? One possible example is a sensor which can simultaneously detect RIs and pH levels of a solution, by combining the principles demonstrated in the sections related to the OMC RI sensor (Section 3.3) and the microfibre LSPR pH sensor (Section 5.6.2). Apart from the potential of multi-analyte detection, such a sensor combing the two principles may also provide a two-

parameter detection when measuring a single environmental change or analyte. For example, by measuring both the coupled spectral shift and the LSPR intensity variation caused by the analyte may provide a more reliable and accurate sensing result.

- **New microfibre packaging techniques.** The sensing capability of a microfibre based sensor relies on its efficient light-environment interactions facilitated by the evanescent fields. A wavelength comparable diameter or sometimes a subwavelength diameter of the microfibre can be essential for many sensing applications. Microfibres with such small diameters are mechanically weak and easy contaminated. Thus many microfibre based devices require a robust fibre packaging technique to ensure the performance of the devices during experiments as well as over time, but must allow for the ingress and egress of a target analyte. Several packaging techniques such as packaging with low-RI polymers [160], supporting with substrates [76] and integration with microfluidics devices [157] have been investigated. However these packaging techniques have many disadvantages such as poor reproducibility and long-term instability. Many packaging techniques also sacrifice the microfibre's sensitivity in detection to achieve the required robustness (e.g. by partially or fully covering the microfibre and thus weakening the light-environment interactions). The lack of high-performance microfibre packaging techniques has limited microfibre sensors to laboratory sensing experiments. Therefore it is crucial to investigate new materials and methods such as microfluidics and 3D printing technologies for the development of new packaging techniques for microfibre based sensors, if such sensors are to be made robust enough and with sufficient reliability for real world applications.

References

[1] J. M. Senior and M. Y. Jamro, *Optical Fiber Communications: Principles and Practice*. Pearson Education, 2009.

[2] E. Udd, *Fiber Optic Sensors: an Introduction for Engineers and Scientists*. John Wiley & Sons, 2011.

[3] G. Brambilla, F. Xu, P. Horak, Y. Jung, F. Koizumi, N. P. Sessions, E. Koukharenko, X. Feng, G. S. Murugan, J. S. Wilkinson, and D. J. Richardson, "Optical fiber nanowires and microwires: fabrication and applications," *Adv. Opt. Photonics*, vol. 1, no. 1, pp. 107 – 161, Jan. 2009.

[4] J. Lou, Y. Wang, and L. Tong, "Microfiber optical sensors: a review," *Sensors*, vol. 14, no. 4, pp. 5823 – 5844, 2014.

[5] J. D. Love and C. Durniak, "Bend Loss, tapering, and cladding-Mode coupling in single-mode fibers," *IEEE Photonics Technol. Lett.*, vol. 19, no. 16, pp. 1257 – 1259, Aug. 2007.

[6] L. Tong and M. Sumetsky, *Subwavelength and Nanometer Diameter Optical Fibers*. Zhejiang University Press and Springer Press, 2009.

[7] Y. Cui, P. P. Shum, G. Wang, H. Chang, X. Q. Dinh, M. Jiang, and G. Humbert, "Size effect of gold nanoparticles on optical microfiber refractive index sensors," in *2011 IEEE Sensors*, 2011, pp. 371 – 374.

[8] S. J. Zalyubovskiy, M. Bogdanova, A. Deinega, Y. Lozovik, A. D. Pris, K. H. An, W. P. Hall, and R. A. Potyrailo, "Theoretical limit of localized surface plasmon resonance sensitivity to local refractive index change and its comparison to conventional surface plasmon resonance sensor," *J. Opt. Soc. Am. A*, vol. 29, no. 6, pp. 994 – 1002, Jun. 2012.

[9] Y. Jung, G. Brambilla, and D. J. Richardson, "Optical microfiber coupler for broadband single-mode operation," *Opt. Express*, vol. 17, no. 7, pp. 5273 – 5278, Mar. 2009.

[10] R. G. Lamont, D. C. Johnson, and K. O. Hill, "Power transfer in fused biconical-taper single-mode fiber couplers: dependence on external refractive index," *Appl. Opt.*, vol. 24, no. 3, p. 327, Feb. 1985.

[11] P. Wang, M. Ding, G. Bramilla, Y. Semenova, Q. Wu, and G. Farrell, "High temperature performance of an optical microfibre coupler and its potential use as a sensor," *Articles*, Jan. 2012.

[12] A. J. Haes and R. P. Van Duyne, "A unified view of propagating and localized surface plasmon resonance biosensors," *Anal. Bioanal. Chem.*, vol. 379, no. 7 – 8, pp. 920 – 930, Aug. 2004.

[13] K. Li, G. Liu, Y. Wu, P. Hao, W. Zhou, and Z. Zhang, "Gold nanoparticle amplified optical microfiber evanescent wave absorption biosensor for cancer biomarker detection in serum," *Talanta*, vol. 120, pp. 419 – 424, Mar. 2014.

[14] H. Y. Lin, C. H. Huang, G. L. Cheng, N. K. Chen, and H. C. Chui, "Tapered optical fiber sensor based on localized surface plasmon resonance," *Opt. Express*, vol. 20, no. 19, pp. 21693 – 21701, Sep. 2012.

[15] K. Jia, M. Y. Khaywah, Y. Li, J. L. Bijeon, P. M. Adam, R. Déturche, B. Guelorget, M. François, G. Louarn, and R. E. Ionescu, "Strong improvements of localized surface plasmon resonance sensitivity by using Au/Ag bimetallic nanostructures modified with polydopamine films," *ACS Appl. Mater. Interfaces*, vol. 6, no. 1, pp. 219 – 227, Jan. 2014.

[16] L. Tong, L. Hu, J. Zhang, J. Qiu, Q. Yang, J. Lou, Y. Shen, J. He, and Z. Ye, "Photonic nanowires directly drawn from bulk glasses," *Opt. Express*, vol. 14, no. 1, pp. 82 – 87, Jan. 2006.

[17] E. J. Zhang, W. D. Sacher, and J. K. S. Poon, "Hydrofluoric acid flow etching of low-loss subwavelength-diameter biconical fiber tapers," *Opt. Express*, vol. 18, no. 21, pp. 22593 – 22598, Oct. 2010.

[18] M. Naqshbandi, J. Canning, M. Nash, and M. J. Crossley, "Controlling the fabrication of self-assembled microwires from silica nanoparticles," in *Proc. SPIE 8424*, 2012, vol. 8421.

[19] G. Brambilla, V. Finazzi, and D. Richardson, "Ultra-low-loss optical fiber nanotapers," *Opt. Express*, vol. 12, no. 10, pp. 2258 – 2263, May 2004.

[20] A. W. Snyder, "Coupling of modes on a tapered dielectric cylinder," *IEEE Trans. Microw. Theory Tech.*, vol. 18, no. 7, pp. 383 – 392, Jul. 1970.

[21] J. D. Love and W. M. Henry, "Quantifying loss minimisation in single-mode fibre tapers," *Electron. Lett.*, vol. 22, no. 17, pp. 912 – 914, Aug. 1986.

[22] S. Lacroix, R. Bourbonnais, F. Gonthier, and J. Bures, "Tapered monomode optical fibers: understanding large power transfer," *Appl. Opt.*, vol. 25, no. 23, pp. 4421 – 4425, Dec. 1986.

[23] F. Gonthier, J. Lapierre, C. Veilleux, S. Lacroix, and J. Bures, "Investigation of power oscillations along tapered monomode fibers," *Appl. Opt.*, vol. 26, no. 3, pp. 444 – 449, Feb. 1987.

[24] A. J. Fielding, K. Edinger, and C. C. Davis, "Experimental observation of mode evolution in single-mode tapered optical fibers," *J. Light. Technol.*, vol. 17, no. 9, pp. 1649 – 1656, Sep. 1999.

[25] S. Lacroix, F. Gonthier, and J. Bures, "All-fiber wavelength filter from successive biconical tapers," *Opt. Lett.*, vol. 11, no. 10, pp. 671 – 673, Oct. 1986.

[26] H. S. MacKenzie and F. P. Payne, "Evanescent field amplification in a tapered single-mode optical fibre," *Electron. Lett.*, vol. 26, no. 2, pp. 130 – 132, Jan. 1990.

[27] T. A. Birks, W. J. Wadsworth, and P. S. J. Russell, "Supercontinuum generation in tapered fibers," *Opt. Lett.*, vol. 25, no. 19, pp. 1415 – 1417, Oct. 2000.

[28] Z. M. Hale and F. P. Payne, "Demonstration of an optimised evanescent field optical fibre sensor," *Anal. Chim. Acta*, vol. 293, no. 1 – 2, pp. 49 – 54, Jul. 1994.

[29] L. C. Bobb, P. M. Shankar, and H. D. Krumboltz, "Bending effects in biconically tapered single-mode fibers," *J. Light. Technol.*, vol. 8, no. 7, pp. 1084 – 1090, Jul. 1990.

[30] P. N. Moar, S. T. Huntington, J. Katsifolis, L. W. Cahill, A. Roberts, and K. A. Nugent, "Fabrication, modeling, and direct evanescent field measurement of tapered optical fiber sensors," *J. Appl. Phys.*, vol. 85, no. 7, pp. 3395 – 3398, Apr. 1999.

[31] J. Bures and R. Ghosh, "Power density of the evanescent field in the vicinity of a tapered fiber," *J. Opt. Soc. Am. A*, vol. 16, no. 8, pp. 1992 – 1996, Aug. 1999.

[32] L. Tong, R. R. Gattass, J. B. Ashcom, S. He, J. Lou, M. Shen, I. Maxwell, and E. Mazur, "Subwavelength-diameter silica wires for low-loss optical wave guiding," *Nature*, vol. 426, no. 6968, pp. 816 – 819, Dec. 2003.

[33] G. Sagué, E. Vetsch, W. Alt, D. Meschede, and A. Rauschenbeutel, "Cold-atom physics using ultrathin optical fibers: light-induced dipole forces and surface interactions," *Phys. Rev. Lett.*, vol. 99, no. 16, p. 163602, Oct. 2007.

[34] V. Balykin, K. Hakuta, F. Le Kien, J. Liang, and M. Morinaga, "Atom trapping and guiding with a subwavelength-diameter optical fiber," *Phys. Rev. A*, vol. 70, no. 1, p. 011401, Jul. 2004.

[35] V. G. Minogin and S. N. Chormaic, "Manifestation of the van der Waals surface interaction in the spontaneous emission of atoms into an optical nanofiber," *Laser Phys.*, vol. 20, no. 1, pp. 32 – 37, Jan. 2010.

[36] A. M. Armani, R. P. Kulkarni, S. E. Fraser, R. C. Flagan, and K. J. Vahala, "Label-free, single-molecule detection with optical microcavities," *Science*, vol. 317, no. 5839, pp. 783 – 787, Aug. 2007.

[37] J. D. Love, W. M. Henry, W. J. Stewart, R. J. Black, S. Lacroix, and F. Gonthier, "Tapered single-mode fibres and devices. I. Adiabaticity criteria," *Optoelectron. IEE Proc. J*, vol. 138, no. 5, pp. 343 – 354, Oct. 1991.

[38] A. W. Snyder and J. Love, *Optical Waveguide Theory*. Springer Science & Business Media, 1983.

[39] T. Lee, "Nonlinear properties of optical microfibres," Ph.D., University of Southampton, 2013.

[40] T. A. Birks and Y. W. Li, "The shape of fiber tapers," *J. Light. Technol.*, vol. 10, no. 4, pp. 432 – 438, Apr. 1992.

[41] G. Brambilla, Y. Jung, and F. Renna, "Optical fiber microwires and nanowires manufactured by modified flame brushing technique: properties and applications," *Front. Optoelectron. China*, vol. 3, no. 1, pp. 61 – 66, Mar. 2010.

[42] J. C. Graf, S. A. Teston, P. V. de Barba, J. Dallmann, J. A. S. Lima, H. J. Kalinowski, and A. S. Paterno, "Fiber taper rig using a simplified heat source and the flame-brush technique," in *Microwave and Optoelectronics Conference (IMOC), 2009 SBMO/IEEE MTT-S International*, 2009, pp. 621 – 624.

[43] L. Tong, F. Zi, X. Guo, and J. Lou, "Optical microfibers and nanofibers: A tutorial," *Opt. Commun.*, vol. 285, no. 23, pp. 4641 – 4647, Oct. 2012.

[44] M. C. Frawley, A. Petcu-Colan, V. G. Truong, and S. Nic Chormaic, "Higher order mode propagation in an optical nanofiber," *Opt. Commun.*, vol. 285, no. 23, pp. 4648 – 4654, Oct. 2012.

[45] P. Polynkin, A. Polynkin, N. Peyghambarian, and M. Mansuripur, "Evanescent field-based optical fiber sensing device for measuring the refractive index of liquids in microfluidic channels," *Opt. Lett.*, vol. 30, no. 11, pp. 1273 – 1275, Jun. 2005.

[46] J. Villatoro and D. Monzón-Hernández, "Fast detection of hydrogen with nano fiber tapers coated with ultra thin palladium layers," *Opt. Express*, vol. 13, no. 13, pp. 5087 – 5092, Jun. 2005.

[47] F. Warken, E. Vetsch, D. Meschede, M. Sokolowski, and A. Rauschenbeutel, "Ultra-sensitive surface absorption spectroscopy using sub-wavelength diameter optical fibers," *Opt. Express*, vol. 15, no. 19, pp. 11952 – 11958, Sep. 2007.

[48] L. Zhang, P. Wang, Y. Xiao, H. Yu, and L. Tong, "Ultra-sensitive microfibre absorption detection in a microfluidic chip," *Lab. Chip*, vol. 11, no. 21, pp. 3720 – 3724, Nov. 2011.

[49] D. T. Cassidy, D. C. Johnson, and K. O. Hill, "Wavelength-dependent transmission of monomode optical fibertapers," *Appl. Opt.*, vol. 24, no. 7, pp. 945 – 950, Apr. 1985.

[50] S. Lacroix, R. J. Black, C. Veilleux, and J. Lapierre, "Tapered single-mode fibers: external refractive-index dependence," *Appl. Opt.*, vol. 25, no. 15, pp. 2468 – 2469, Aug. 1986.

[51] S. Lacroix, R. Bourbonnais, F. Gonthier, and J. Bures, "Tapered monomode optical fibers: understanding large power transfer," *Appl. Opt.*, vol. 25, no. 23, pp. 4421 – 4425, Dec. 1986.

[52] S. Lacroix, F. Gonthier, R. J. Black, and J. Bures, "Tapered-fiber interferometric wavelength response: the achromatic fringe," *Opt. Lett.*, vol. 13, no. 5, pp. 395 – 397, May 1988.

[53] H. Latifi, M. I. Zibaii, S. M. Hosseini, and P. Jorge, "Nonadiabatic tapered optical fiber for biosensor applications," *Photonic Sens.*, vol. 2, no. 4, pp. 340 – 356, Dec. 2012.

[54] W. B. Ji, H. H. Liu, S. C. Tjin, K. K. Chow, and A. Lim, "Ultrahigh sensitivity refractive index sensor based on optical microfiber," *IEEE Photonics Technol. Lett.*, vol. 24, no. 20, pp. 1872 – 1874, Oct. 2012.

[55] J. Lou, L. Tong, and Z. Ye, "Modeling of silica nanowires for optical sensing," *Opt. Express*, vol. 13, no. 6, pp. 2135 – 2140, Mar. 2005.

[56] J. Wo, G. Wang, Y. Cui, Q. Sun, R. Liang, P. P. Shum, and D. Liu, "Refractive index sensor using microfiber-based Mach Zehnder interferometer," *Opt. Lett.*, vol. 37, no. 1, pp. 67 – 69, Jan. 2012.

[57] Z. Tian, S. S.-H. Yam, and H.-P. Loock, "Refractive index sensor based on an abrupt taper Michelson interferometer in a single-mode fiber," *Opt. Lett.*, vol. 33, no. 10, pp. 1105 – 1107, May 2008.

[58] Z. Tian, S. S.-H. Yam, J. Barnes, W. Bock, P. Greig, J. M. Fraser, H. Loock, and R. D. Oleschuk, "Refractive index sensing with Mach Zehnder interferometer based on concatenating two single-mode fiber tapers," *IEEE Photonics Technol. Lett.*, vol. 20, no. 8, pp. 626 – 628, Apr. 2008.

[59] J.-M. Hsu, C.-L. Lee, H.-P. Chang, W. C. Shih, and C.-M. Li, "Highly sensitive tapered fiber Mach Zehnder interferometer for liquid level sensing," *IEEE Photonics Technol. Lett.*, vol. 25, no. 14, pp. 1354 – 1357, Jul. 2013.

[60] Q. Wang and G. Farrell, "All-fiber multimode-interference-based refractometer sensor: proposal and design," *Opt. Lett.*, vol. 31, no. 3, pp. 317 – 319, Feb. 2006.

[61] P. Wang, G. Brambilla, M. Ding, Y. Semenova, Q. Wu, and G. Farrell, "High-sensitivity, evanescent field refractometric sensor based on a tapered, multimode fiber interference," *Opt. Lett.*, vol. 36, no. 12, pp. 2233 – 2235, Jun. 2011.

[62] Y. Zhang, B. Lin, S. C. Tjin, H. Zhang, G. Wang, P. Shum, and X. Zhang, "Refractive index sensing based on higher-order mode reflection of a microfiber Bragg grating," *Opt. Express*, vol. 18, no. 25, pp. 26345 – 26350, Dec. 2010.

[63] X. Fang, C. R. Liao, and D. N. Wang, "Femtosecond laser fabricated fiber Bragg grating in microfiber for refractive index sensing," *Opt. Lett.*, vol. 35, no. 7, pp. 1007 – 1009, Apr. 2010.

[64] Y. Liu, C. Meng, A. P. Zhang, Y. Xiao, H. Yu, and L. Tong, "Compact microfiber Bragg gratings with high-index contrast," *Opt. Lett.*, vol. 36, no. 16, pp. 3115 – 3117, Aug. 2011.

[65] Y. Ran, Y.-N. Tan, L.-P. Sun, S. Gao, J. Li, L. Jin, and B.-O. Guan, "193nm excimer laser inscribed Bragg gratings in microfibers for refractive index sensing," *Opt. Express*, vol. 19, no. 19, pp. 18577 – 18583, Sep. 2011.

[66] J. Kou, S. Qiu, F. Xu, and Y. Lu, "Demonstration of a compact temperature sensor based on first-order Bragg grating in a tapered fiber probe," *Opt. Express*, vol. 19, no. 19, pp. 18452 – 18457, Sep. 2011.

[67] T. Wieduwilt, S. Brückner, and H. Bartelt, "High force measurement sensitivity with fiber Bragg gratings fabricated in uniform-waist fiber tapers," *Meas. Sci. Technol.*, vol. 22, no. 7, p. 075201, Jul. 2011.

[68] K. Ni, C. C. Chan, X. Dong, and L. Li, "Temperature-independent accelerometer using a fiber Bragg grating incorporating a biconical taper," *Opt. Fiber Technol.*, vol. 19, no. 5, pp. 410 – 413, Oct. 2013.

[69] O. Frazão, S. F. O. Silva, A. Guerreiro, J. L. Santos, L. A. Ferreira, and F. M. Araújo, "Strain sensitivity control of fiber Bragg grating structures with fused tapers," *Appl. Opt.*, vol. 46, no. 36, pp. 8578 – 8582, Dec. 2007.

[70] H. Xuan, W. Jin, and M. Zhang, "CO2 laser induced long period gratings in optical microfibers," *Opt. Express*, vol. 17, no. 24, pp. 21882 – 21890, Nov. 2009.

[71] C. Caspar and E.-J. Bachus, "Fibre-optic micro-ring-resonator with 2 mm diameter," *Electron. Lett.*, vol. 25, no. 22, pp. 1506 – 1508, Oct. 1989.

[72] X. Wu and L. Tong, "Optical microfibers and nanofibers," *Nanophotonics*, vol. 2, no. 5 – 6, pp. 407 – 428, 2013.

[73] M. Sumetsky, Y. Dulashko, J. M. Fini, and A. Hale, "Optical microfiber loop resonator," in *Conference on Lasers and Electro-Optics, 2005. (CLEO)*, 2005, vol. 1, pp. 432 – 433.

[74] M. Sumetsky, Y. Dulashko, J. M. Fini, A. Hale, and D. J. DiGiovanni, "The microfiber loop resonator: theory, experiment, and application," *J. Light. Technol.*, vol. 24, no. 1, pp. 242 – 250, Jan. 2006.

[75] X. Y. Shi Lei, "Simulation of optical microfiber loop resonators for ambient refractive index sensing," *Sensors*, 2007.

[76] X. Guo and L. Tong, "Supported microfiber loops for optical sensing," *Opt. Express*, vol. 16, no. 19, pp. 14429 – 14434, Sep. 2008.

[77] P. Pal and W. H. Knox, "Fabrication and characterization of fused microfiber resonators," *IEEE Photonics Technol. Lett.*, vol. 21, no. 12, pp. 766 – 768, Jun. 2009.

[78] G. Vienne, Y. Li, and L. Tong, "Effect of host polymer on microfiber resonator," *IEEE Photonics Technol. Lett.*, vol. 19, no. 18, pp. 1386 – 1388, Sep. 2007.

[79] F. Xu, V. Pruneri, V. Finazzi, and G. Brambilla, "High sensitivity refractometric sensor based on embedded optical microfiber loop resonator," in *Conference on Lasers and Electro-Optics and Conference on Quantum Electronics and Laser Science*, 2008, pp. 1 – 2.

[80] X. Jiang, L. Tong, G. Vienne, X. Guo, A. Tsao, Q. Yang, and D. Yang, "Demonstration of optical microfiber knot resonators," *Appl. Phys. Lett.*, vol. 88, no. 22, p. 223501, May 2006.

[81] Y. Wu, Y.-J. Rao, Y.-H. Chen, and Y. Gong, "Miniature fiber-optic temperature sensors based on silica/polymer microfiber knot resonators," *Opt. Express*, vol. 17, no. 20, pp. 18142 – 18147, Sep. 2009.

[82] Y. Wu, T. Zhang, Y. Rao, and Y. Gong, "Miniature interferometric humidity sensors based on silica/polymer microfiber knot resonators," *Sens. Actuators B Chem.*, vol. 155, no. 1, pp. 258 – 263, Jul. 2011.

[83] C. Hou, Y. Wu, X. Zeng, S. Zhao, Q. Zhou, and G. Yang, "Novel high sensitivity accelerometer based on a microfiber loop resonator," *Opt. Eng.*, vol. 49, no. 1, pp. 014402 – 014402 – 6, 2010.

[84] K. S. Lim, S. W. Harun, S. S. A. Damanhuri, A. A. Jasim, C. K. Tio, and H. Ahmad, "Current sensor based on microfiber knot resonator," *Sens. Actuators Phys.*, vol. 167, no. 1, pp. 60 – 62, May 2011.

[85] X. Li and H. Ding, "All-fiber magnetic-field sensor based on microfiber knot resonator and magnetic fluid," *Opt. Lett.*, vol. 37, no. 24, pp. 5187 – 5189, Dec. 2012.

[86] A. Sulaiman, M. Z. Muhammad, S. W. Harun, H. Arof, and H. Ahmad, "Demonstration of acoustic vibration sensor based on microfiber knot resonator," *Microw. Opt. Technol. Lett.*, vol. 55, no. 5, pp. 1138 – 1141, May 2013.

[87] H. Yu, L. Xiong, Z. Chen, Q. Li, X. Yi, Y. Ding, F. Wang, H. Lv, and Y. Ding, "Solution concentration and refractive index sensing based on polymer microfiber knot resonator," *Appl. Phys. Express*, vol. 7, no. 2, p. 022501, Feb. 2014.

[88] X. Li and H. Ding, "A stable evanescent field-Based microfiber knot resonator refractive index sensor," *IEEE Photonics Technol. Lett.*, vol. 26, no. 16, pp. 1625 – 1628, Aug. 2014.

[89] M. Sumetsky, "Optical fiber microcoil resonators," *Opt. Express*, vol. 12, no. 10, pp. 2303 – 2316, May 2004.

[90] M. Sumetsky, "Uniform coil optical resonator and waveguide: transmission spectrum, eigenmodes, and dispersion relation," *Opt. Express*, vol. 13, no. 11, pp. 4331 – 4340, May 2005.

[91] F. Xu, P. Horak, and G. Brambilla, "Conical and biconical ultra-high-Q optical-fiber nanowire microcoil resonator," *Appl. Opt.*, vol. 46, no. 4, pp. 570 – 573, Feb. 2007.

[92] F. Xu, P. Horak, and G. Brambilla, "Optimized design of microcoil resonators," *J. Light. Technol.*, vol. 25, no. 6, pp. 1561 – 1567, Jun. 2007.

[93] F. Xu and G. Brambilla, "Embedding optical microfiber coil resonators in Teflon," *Opt. Lett.*, vol. 32, no. 15, pp. 2164 – 2166, Aug. 2007.

[94] F. Xu, G. Brambilla, J. Feng, and Y. Lu, "Mathematical model for manufacturing microfiber coil resonators," *Opt. Eng.*, vol. 49, no. 4, pp. 044001 – 044001 – 4, 2010.

[95] F. Xu, P. Horak, and G. Brambilla, "Optical microfiber coil resonator refractometric sensor," *Opt. Express*, vol. 15, no. 12, pp. 7888 – 7893, Jun. 2007.

[96] Y. Jung, G. Senthil Murugan, G. Brambilla, and D. J. Richardson, "Embedded optical microfiber coil resonator with enhanced high-Q," *IEEE Photonics Technol. Lett.*, vol. 22, no. 22, pp. 1638 – 1640, Nov. 2010.

[97] R. Ismaeel, T. Lee, F. Al-Saab, Y. Jung, and G. Brambilla, "A self-coupling multi-port microcoil resonator," *Opt. Express*, vol. 20, no. 8, pp. 8568 – 8574, Apr. 2012.

[98] M. Digonnet and H. J. Shaw, "Wavelength multiplexing in single-mode fiber couplers," *Appl. Opt.*, vol. 22, no. 3, pp. 484 – 491, Feb. 1983.

[99] F. de Fornel, C. M. Ragdale, and R. J. Mears, "Analysis of single-mode fused tapered fibre couplers," *Microw. Opt. Antennas IEE Proc. H*, vol. 131, no. 4, pp. 221 – 227, Aug. 1984.

[100] R. G. Lamont, D. C. Johnson, and K. O. Hill, "Power transfer in fused biconical-taper single-mode fiber couplers: dependence on external refractive index," *Appl. Opt.*, vol. 24, no. 3, pp. 327 – 332, Feb. 1985.

[101] H. Tazawa, T. Kanie, and M. Katayama, "Fiber-optic coupler based refractive index sensor and its application to biosensing," *Appl. Phys. Lett.*, vol. 91, no. 11, p. 113901, Sep. 2007.

[102] M. Ding, P. Wang, and G. Brambilla, "A microfiber coupler tip thermometer," *Opt. Express*, vol. 20, no. 5, pp. 5402 – 5408, Feb. 2012.

[103] R. Ismaeel, T. Lee, T. Melvin, and G. Brambilla, "Sensitive optical microfiber-based biosensors for DNA detection," in *Advanced Photonics*, 2014, p. JM5A.67.

[104] Y. Chen, S. Yan, X. Zheng, F. Xu, and Y. Lu, "A miniature reflective micro-force sensor based on a microfiber coupler," *Opt. Express*, vol. 22, no. 3, pp. 2443 – 2450, Feb. 2014.

[105] G. Kakarantzas, T. E. Dimmick, T. A. Birks, R. Le Roux, and P. S. J. Russell, "Miniature all-fiber devices based on CO2 laser microstructuring of tapered fibers," *Opt. Lett.*, vol. 26, no. 15, pp. 1137 – 1139, Aug. 2001.

[106] L. Tong, L. Hu, J. Zhang, J. Qiu, Q. Yang, J. Lou, Y. Shen, J. He, and Z. Ye, "Photonic nanowires directly drawn from bulk glasses," *Opt. Express*, vol. 14, no. 1, pp. 82 – 87, Jan. 2006.

[107] C. R. Liao, D. N. Wang, X. He, and M. W. Yang, "Twisted optical microfibers for refractive index sensing," *IEEE Photonics Technol. Lett.*, vol. 23, no. 13, pp. 848 – 850, Jul. 2011.

[108] F. Vollmer and S. Arnold, "Whispering-gallery-mode biosensing: label-free detection down to single molecules," *Nat. Methods*, vol. 5, no. 7, pp. 591 – 596, Jul. 2008.

[109] I. M. White, H. Oveys, and X. Fan, "Liquid-core optical ring-resonator sensors," *Opt. Lett.*, vol. 31, no. 9, pp. 1319 – 1321, May 2006.

[110] H. Jeong, S. Lee, G. Yong Sung, and J. H. Shin, "Design and fabrication of Tb3+ -doped silicon oxy-nitride microdisk for biosensor applications," *IEEE Photonics Technol. Lett.*, vol. 23, no. 2, pp. 88 – 90, Jan. 2011.

[111]T. Teranishi, M. Eguchi, M. Kanehara, and S. Gwo, "Controlled localized surface plasmon resonance wavelength for conductive nanoparticles over the ultraviolet to near-infrared region," *J. Mater. Chem.*, vol. 21, no. 28, pp. 10238 – 10242, Jul. 2011.

[112]J. Conde, o, J. Rosa, o, J. Lima, O. C, and P. V. Baptista, "Nanophotonics for molecular diagnostics and therapy applications," *Int. J. Photoenergy*, vol. 2012, Sep. 2011.

[113]J. Luo, J. Yao, Y. Lu, W. Ma, and X. Zhuang, "A silver nanoparticle-modified evanescent field optical fiber sensor for methylene blue detection," *Sensors*, vol. 13, no. 3, pp. 3986 – 3997, Mar. 2013.

[114]M. Wan, P. Luo, J. Jin, J. Xing, Z. Wang, and S. T. C. Wong, "Fabrication of localized surface plasmon resonance fiber probes using ionic self-assembled gold nanoparticles," *Sensors*, vol. 10, no. 7, pp. 6477 – 6487, Jul. 2010.

[115]K. Mitsui, Y. Handa, and K. Kajikawa, "Optical fiber affinity biosensor based on localized surface plasmon resonance," *Appl. Phys. Lett.*, vol. 85, no. 18, p. 4231, 2004.

[116]Y. Shao, S. Xu, X. Zheng, Y. Wang, and W. Xu, "Optical fiber LSPR Biosensor prepared by gold nanoparticle assembly on polyelectrolyte multilayer," *Sensors*, vol. 10, no. 4, pp. 3585 – 3596, Apr. 2010.

[117]R. Dutta, R. Bharadwaj, S. Mukherji, and T. Kundu, "Study of localized surface-plasmon-resonance-based optical fiber sensor," *Appl. Opt.*, vol. 50, no. 25, pp. E138 – E144, Sep. 2011.

[118]Q. Zhang, C. Xue, Y. Yuan, J. Lee, D. Sun, and J. Xiong, "Fiber surface modification technology for fiber-optic localized surface plasmon resonance biosensors," *Sensors*, vol. 12, no. 3, pp. 2729 – 2741, Feb. 2012.

[119]B. S. Kawasaki and K. O. Hill, "Low-loss access coupler for multimode optical fiber distribution networks," *Appl. Opt.*, vol. 16, no. 7, pp. 1794 – 1795, Jul. 1977.

[120]B. S. Kawasaki, K. O. Hill, and R. G. Lamont, "Biconical-taper single-mode fiber coupler," *Opt. Lett.*, vol. 6, no. 7, pp. 327 – 328, Jul. 1981.

[121]K. Morishita and K. Yamazaki, "Wavelength and polarization dependences of fused fiber couplers," *J. Light. Technol.*, vol. 29, no. 3, pp. 330 – 334, Feb. 2011.

[122]F. P. Payne, C. D. Hussey, and M. S. Yataki, "Polarisation analysis of strongly fused and weakly fused tapered couplers," *Electron. Lett.*, vol. 21, no. 13, pp. 561 – 563, Jun. 1985.

[123]K. Morishita and K. Takashina, “Polarization properties of fused fiber couplers and polarizing beamsplitters,” *J. Light. Technol.*, vol. 9, no. 11, pp. 1503 – 1507, Nov. 1991.

[124]T. Findakly and C.-L. Chen, “Optical directional couplers with variable spacing,” *Appl. Opt.*, vol. 17, no. 5, pp. 769 – 773, Mar. 1978.

[125]F. P. Payne, C. D. Hussey, and M. S. Yataki, “Modelling fused single-mode-fibre couplers,” *Electron. Lett.*, vol. 21, no. 11, pp. 461 – 462, May 1985.

[126]A. . Snyder and J. D. Love, “Coupled-mode theory for optical fibers,” *J. Opt. Soc. Am.*, vol. 62, no. 11, pp. 1267 – 1277, Nov. 1972.

[127]R. Tewari and K. Thyagarajan, “Analysis of tunable single-mode fiber directional couplers using simple and accurate relations,” *J. Light. Technol.*, vol. 4, no. 4, pp. 386 – 390, Apr. 1986.

[128]A. G. Bulushev, Y. V. Gurov, E. M. Dianov, O. G. Okhotnikov, A. M. Prokhorov, and B. P. Shurukhin, “Wavelength- and polarization-selective fused single-mode couplers,” *Opt. Lett.*, vol. 13, no. 3, pp. 230 – 232, Mar. 1988.

[129]F. Bilodeau, K. O. Hill, S. Faucher, and D. C. Johnson, “Low-loss highly overcoupled fused couplers: fabrication and sensitivity to external pressure,” *J. Light. Technol.*, vol. 6, no. 10, pp. 1476 – 1482, Oct. 1988.

[130]Y. Jung, G. Brambilla, and D. J. Richardson, “Polarization-maintaining optical microfiber,” *Opt. Lett.*, vol. 35, no. 12, pp. 2034 – 2036, Jun. 2010.

[131]J. L. Armstrong, M. J. Matthewson, and C. R. Kurkjian, “Humidity dependence of the fatigue of high-strength fused silica optical fibers,” *J. Am. Ceram. Soc.*, vol. 83, no. 12, pp. 3100 – 3109, 2000.

[132]M. Muraoka, K. Ebata, and H. Abe, “Effect of humidity on small-crack growth in silica optical fibers,” *J. Am. Ceram. Soc.*, vol. 76, no. 6, pp. 1545 – 1550, Jun. 1993.

[133]G. Brambilla, F. Xu, and X. Feng, “Fabrication of optical fibre nanowires and their optical and mechanical characterisation,” *Electron. Lett.*, vol. 42, no. 9, pp. 517 – 519, Apr. 2006.

[134]N. Yamazoe and Y. Shimizu, “Humidity sensors: Principles and applications,” *Sens. Actuators*, vol. 10, no. 3 – 4, pp. 379 – 398, Nov. 1986.

[135]M. G. Lawrence, “The relationship between relative humidity and the dewpoint temperature in moist air: a simple conversion and applications,” *Bull. Am. Meteorol. Soc.*, vol. 86, pp. 225 – 233, Feb. 2005.

[136]C. R. K. M. JOHN MATTHEWSON, "Environmental effects on the static fatigue of silica optical fiber," *J. Am. Ceram. Soc.*, vol. 71, no. 3, pp. 177 – 183, 1988.

[137]T. L. Yeo, T. Sun, and K. T. V. Grattan, "Fibre-optic sensor technologies for humidity and moisture measurement," *Sens. Actuators Phys.*, vol. 144, no. 2, pp. 280 – 295, Jun. 2008.

[138]Y. Wu, T. Zhang, Y. Rao, and Y. Gong, "Miniature interferometric humidity sensors based on silica/polymer microfiber knot resonators," *Sens. Actuators B Chem.*, vol. 155, no. 1, pp. 258 – 263, Jul. 2011.

[139]P. Wang, F. Gu, L. Zhang, and L. Tong, "Polymer microfiber rings for high-sensitivity optical humidity sensing," *Appl. Opt.*, vol. 50, no. 31, pp. G7 – G10, Nov. 2011.

[140]Y. Zheng, X. Dong, C. Zhao, Y. Li, L. Shao, and S. Jin, "Relative humidity sensor based on microfiber loop resonator," *Adv. Mater. Sci. Eng.*, vol. 2013, p. e815930, Sep. 2013.

[141]S. Acikgoz, B. Bilen, M. M. Demir, Y. Z. Menceloglu, Y. Skarlatos, G. Aktas, and M. N. Inci, "Use of polyethylene glycol coatings for optical fibre humidity sensing," *Opt. Rev.*, vol. 15, no. 2, pp. 84 – 90, Apr. 2008.

[142]M. Konstantaki, S. Pissadakis, S. Pispas, N. Madamopoulos, and N. A. Vainos, "Optical fiber long-period grating humidity sensor with poly(ethylene oxide)/cobalt chloride coating," *Appl. Opt.*, vol. 45, no. 19, pp. 4567 – 4571, Jul. 2006.

[143]D. C. Bownass, J. S. Barton, and J. D. C. Jones, "Detection of high humidity by optical fibre sensing at telecommunications wavelengths," *Opt. Commun.*, vol. 146, no. 1 – 6, pp. 90 – 94, Jan. 1998.

[144]M. A. Cohen Stuart, G. J. Fleer, and B. H. Bijsterbosch, "The adsorption of poly(vinyl pyrrolidone) onto silica. I. Adsorbed amount," *J. Colloid Interface Sci.*, vol. 90, no. 2, pp. 310 – 320, Dec. 1982.

[145]J. Mathew, Y. Semenova, G. Rajan, and G. Farrell, "Photonic crystal fiber interferometer for dew detection," in *Proc. SPIE 7753, 21st International Conference on Optical Fiber Sensors*, 2011, vol. 7753, p. 77531P – 77531P – 4.

[146]S. F. H. Correia, P. Antunes, E. Pecoraro, P. P. Lima, H. Varum, L. D. Carlos, R. A. S. Ferreira, and P. S. André, "Optical fiber relative humidity sensor based on a FBG with a di-ureasil coating," *Sensors*, vol. 12, no. 7, pp. 8847 – 8860, Jun. 2012.

[147]A. Alvarez-Herrero, H. Guerrero, and D. Levy, "High-sensitivity sensor of low relative humidity based on overlay on side-polished fibers," *IEEE Sens. J.*, vol. 4, no. 1, pp. 52 – 56, Feb. 2004.

[148]Y. Liu, L. Wang, M. Zhang, D. Tu, X. Mao, and Y. Liao, "Long-period grating relative humidity sensor with hydrogel coating," *IEEE Photonics Technol. Lett.*, vol. 19, no. 12, pp. 880 – 882, Jun. 2007.

[149]R. Ismaeel, T. Lee, M. Gouveia, M. Ding, T. Melvin, and G. Brambilla, "Design and optimization of a microfiber coupler for biosensing," in *Advanced Photonics 2013*, 2013, p. SM2D.3.

[150]D. R. Thévenot, K. Toth, R. A. Durst, and G. S. Wilson, "Electrochemical biosensors: recommended definitions and classification," *Biosens. Bioelectron.*, vol. 16, no. 1 – 2, pp. 121 – 131, Jan. 2001.

[151]N. B. Ramírez, A. M. Salgado, and B. Valdman, "The evolution and developments of immunosensors for health and environmental monitoring: problems and perspectives," *Braz. J. Chem. Eng.*, vol. 26, no. 2, pp. 227 – 249, 2009.

[152]M. S. Azam, M. R. T. Rahman, Z. Lou, Y. Tang, S. M. Raqib, and J. S. Jothi, "Review: Advancements and application of immunosensors in the analysis of food contaminants," *Nusantara Bioscie.*, vol. 6, no. 2, pp. 186 – 195, Nov. 2014.

[153]B. J. Tromberg, M. J. Sepaniak, T. Vo-Dinh, and G. D. Griffin, "Fiber-optic chemical sensors for competitive binding fluoroimmunoassay," *Anal. Chem.*, vol. 59, no. 8, pp. 1226 – 1230, 1987.

[154]G. P. Anderson and N. L. Nerurkar, "Improved fluoroimmunoassays using the dye Alexa Fluor 647 with the RAPTOR, a fiber optic biosensor," *J. Immunol. Methods*, vol. 271, no. 1 – 2, pp. 17 – 24, Dec. 2002.

[155]T. Endo, S. Yamamura, N. Nagatani, Y. Morita, Y. Takamura, and E. Tamiya, "Localized surface plasmon resonance based optical biosensor using surface modified nanoparticle layer for label-free monitoring of antigen – antibody reaction," *Sci. Technol. Adv. Mater.*, vol. 6, no. 5, p. 491, Jul. 2005.

[156]J. M. Corres, I. R. Matias, J. Bravo, and F. J. Arregui, "Tapered optical fiber biosensor for the detection of anti-gliadin antibodies," *Sens. Actuators B Chem.*, vol. 135, no. 1, pp. 166 – 171, Dec. 2008.

[157]Y. Tian, W. Wang, N. Wu, X. Zou, and X. Wang, "Tapered optical fiber sensor for label-free detection of biomolecules," *Sensors*, vol. 11, no. 4, pp. 3780 – 3790, Mar. 2011.

[158]T. Tagawa, T. Tamura, and P. A. Oberg, *Biomedical sensors and instruments, second edition*. CRC Press, 2011.

[159]G. Khot, F. Kuforiji, R. Wright, and P. Roach, "Dynamic assessment of fibrinogen adsorption and secondary structure perturbation," in *UK Society for Biomaterials Annual Conference 2013*, 2014, vol. 2014, p. e601546.

[160]F. Xu and G. Brambilla, "Embedding optical microfiber coil resonators in Teflon," *Opt. Lett.*, vol. 32, no. 15, pp. 2164 – 2166, Aug. 2007.

[161]G. Vienne, Y. Li, and L. Tong, "Effect of host polymer on microfiber resonator," *IEEE Photonics Technol. Lett.*, vol. 19, no. 18, pp. 1386 – 1388, Sep. 2007.

[162]G. Decher, J. D. Hong, and J. Schmitt, "Buildup of ultrathin multilayer films by a self-assembly process: III. Consecutively alternating adsorption of anionic and cationic polyelectrolytes on charged surfaces," *Thin Solid Films*, vol. 210 – 211, Part 2, pp. 831 – 835, Apr. 1992.

[163]K. Ray, R. Badugu, and J. R. Lakowicz, "Polyelectrolyte layer-by-layer assembly to control the distance between fluorophores and plasmonic nanostructures," *Chem. Mater.*, vol. 19, no. 24, pp. 5902 – 5909, Nov. 2007.

[164]M. Lösche, J. Schmitt, G. Decher, W. G. Bouwman, and K. Kjaer, "Detailed structure of molecularly thin polyelectrolyte multilayer films on solid substrates as revealed by neutron reflectometry," *Macromolecules*, vol. 31, no. 25, pp. 8893 – 8906, 1998.

[165]W. L. W. Hau, D. W. Trau, N. J. Sucher, M. Wong, and Y. Zohar, "Surface-chemistry technology for microfluidics," *J. Micromechanics Microengineering*, vol. 13, no. 2, p. 272, Mar. 2003.

[166]R. N. Smith, M. McCormick, C. J. Barrett, L. Reven, and H. W. Spiess, "NMR studies of PAH/PSS polyelectrolyte multilayers adsorbed onto silica," *Macromolecules*, vol. 37, no. 13, pp. 4830 – 4838, 2004.

[167]S. T. Lord, "Molecular mechanisms affecting fibrin structure and stability," *Arterioscler. Thromb. Vasc. Biol.*, vol. 31, no. 3, pp. 494 – 499, Mar. 2011.

[168]C. E. Hall and H. S. Slayter, "The fibrinogen molecule: its size, shape, and mode of polymerization," *J. Biophys. Biochem. Cytol.*, vol. 5, no. 1, pp. 11 – 27, Jan. 1959.

[169]A. Toscano and M. M. Santore, "Fibrinogen adsorption on three silica-based surfaces: conformation and kinetics," *Langmuir*, vol. 22, no. 6, pp. 2588 – 2597, Mar. 2006.

[170]G. Rajan, "A macro-bend fiber based wavelength demodulation system for optical fiber sensing applications," Ph.D., Dublin Institute of Technology, 2008.

[171]K. Nakanishi, T. Sakiyama, and K. Imamura, "On the adsorption of proteins on solid surfaces, a common but very complicated phenomenon," *J. Biosci. Bioeng.*, vol. 91, no. 3, pp. 233 – 244, 2001.

[172]T. Teranishi, M. Eguchi, M. Kanehara, and S. Gwo, "Controlled localized surface plasmon resonance wavelength for conductive nanoparticles over the ultraviolet to near-infrared region," *J. Mater. Chem.*, vol. 21, no. 28, p. 10238, 2011.

[173]S. J. Zalyubovskiy, M. Bogdanova, A. Deinega, Y. Lozovik, A. D. Pris, K. H. An, W. P. Hall, and R. A. Potyrailo, "Theoretical limit of localized surface plasmon resonance sensitivity to local refractive index change and its comparison to conventional surface plasmon resonance sensor," *J. Opt. Soc. Am. A*, vol. 29, no. 6, pp. 994 – 1002, Jun. 2012.

[174]J. Conde, J. Rosa, J. C. Lima, and P. V. Baptista, "Nanophotonics for molecular diagnostics and therapy applications," *Int. J. Photoenergy*, vol. 2012, p. e619530, Sep. 2011.

[175]S. F. Cheng and L. K. Chau, "Colloidal gold-modified optical fiber for chemical and biochemical sensing," *Anal. Chem.*, vol. 75, no. 1, pp. 16 – 21, 2002.

[176]H. Tu, T. Sun, and K. T. Grattan, "SPR-based optical fber sensors using gold-silver alloy particles as the active sensing material," *IEEE Sens. J.*, vol. 13, no. 6, pp. 2192 – 2199, Jun. 2013.

[177]S. Link, Z. L. Wang, and M. A. El-Sayed, "Alloy formation of gold-silver nanoparticles and the dependence of the plasmon absorption on their composition," *J. Phys. Chem. B*, vol. 103, no. 18, pp. 3529 – 3533, Apr. 1999.

[178]S. Link, Z. L. Wang, and M. A. El-Sayed, "Alloy formation of gold-silver nanoparticles and the dependence of the plasmon absorption on their composition," *J. Phys. Chem. B*, vol. 103, no. 18, pp. 3529 – 3533, 1999.

[179]J. F. Sánchez-Ramírez, U. Pal, L. Nolasco-Hernández, J. Mendoza-Álvarez, and J. A. Pescador-Rojas, "Synthesis and optical properties of Au-Ag alloy nanoclusters with controlled composition," *J. Nanomater.*, vol. 2008, p. e620412, Sep. 2008.

[180]D. Mahl, J. Diendorf, S. Ristig, C. Greulich, Z.-A. Li, M. Farle, M. Köller, and M. Epple, "Silver, gold, and alloyed silver – gold nanoparticles: characterization and comparative cell-biologic action," *J. Nanoparticle Res.*, vol. 14, no. 10, pp. 1 – 13, Sep. 2012.

[181]Y. Yang, J. Shi, G. Kawamura, and M. Nogami, "Preparation of Au – Ag, Ag – Au core – shell bimetallic nanoparticles for surface-enhanced Raman scattering," *Scr. Mater.*, vol. 58, no. 10, pp. 862 – 865, May 2008.

[182]W. Wu, P. N. Njoki, H. Han, H. Zhao, E. A. Schiff, P. S. Lutz, L. Solomon, S. Matthews, and M. M. Maye, "Processing core/alloy/shell nanoparticles: tunable optical properties and evidence for self-limiting alloy growth," *J. Phys. Chem. C*, vol. 115, no. 20, pp. 9933 – 9942, 2011.

[183]L. Lu, G. Burkey, I. Halaciuga, and D. V. Goia, "Core-shell gold/silver nanoparticles: synthesis and optical properties," *J. Colloid Interface Sci.*, vol. 392, pp. 90 – 95, Feb. 2013.

[184]A. K. Sharma and B. D. Gupta, "Fibre-optic sensor based on surface plasmon resonance with Ag-Au alloy nanoparticle films," *Nanotechnology*, vol. 17, no. 1, p. 124, Jan. 2006.

[185]J. Conde, J. Rosa, J. M. de la Fuente, and P. V. Baptista, "Gold-nanobeacons for simultaneous gene specific silencing and intracellular tracking of the silencing events," *Biomaterials*, vol. 34, no. 10, pp. 2516 – 2523, Mar. 2013.

[186]Y. Cui, P. P. Shum, G. Wang, H. Chang, X. Q. Dinh, M. Jiang, and G. Humbert, "Size effect of gold nanoparticles on optical microfiber refractive index sensors," in *2011 IEEE Sensors*, 2011, pp. 371 – 374.

[187]T. A. Birks and C. D. Hussey, "Adiabaticity of miniature loops in tapered single-mode fibre," *Electron. Lett.*, vol. 28, no. 22, pp. 2034 – 2035, Oct. 1992.

[188]D. Marcuse, "Curvature loss formula for optical fibers," *J. Opt. Soc. Am.*, vol. 66, no. 3, pp. 216 – 220, Mar. 1976.

[189]M. Schönhoff, "Self-assembled polyelectrolyte multilayers," *Curr. Opin. Colloid Interface Sci.*, vol. 8, no. 1, pp. 86 – 95, Mar. 2003.

[190]M. H. Tu, T. Sun, and K. T. V. Grattan, "Optimization of gold-nanoparticle-based optical fibre surface plasmon resonance (SPR)-based sensors," *Sens. Actuators B Chem.*, vol. 164, no. 1, pp. 43 – 53, Mar. 2012.

[191]K. A. Willets and R. P. Van Duyne, "Localized surface plasmon resonance spectroscopy and sensing," *Annu. Rev. Phys. Chem.*, vol. 58, pp. 267 – 297, 2007.

[192]W. C. Michie, B. Culshaw, M. Konstantaki, I. McKenzie, S. Kelly, N. B. Graham, and C. Moran, "Distributed pH and water detection using fiber-optic sensors and hydrogels," *J. Light. Technol.*, vol. 13, no. 7, pp. 1415 – 1420, Jul. 1995.

[193]B. Gu, M.-J. Yin, A. P. Zhang, J.-W. Qian, and S. He, "Low-cost high-performance fiber-optic pH sensor based on thin-core fiber modal interferometer," *Opt. Express*, vol. 17, no. 25, pp. 22296 – 22302, Dec. 2009.

[194]L.-Y. Shao, M.-J. Yin, H.-Y. Tam, and J. Albert, "Fiber optic pH sensor with self-assembled polymer multilayer nanocoatings," *Sensors*, vol. 13, no. 2, pp. 1425 – 1434, Jan. 2013.

[195]A. B. Socorro, I. del Villar, J. M. Corres, F. J. Arregui, and I. R. Matias, "Tapered Single-Mode Optical Fiber pH Sensor Based on Lossy Mode Resonances Generated by a Polymeric Thin-Film," *IEEE Sens. J.*, vol. 12, no. 8, pp. 2598 – 2603, Aug. 2012.

[196]I. Kasik, J. Mrazek, T. Martan, M. Pospisilova, O. Podrazky, V. Matejec, K. Hoyerova, and M. Kaminek, "Fiber-optic pH detection in small volumes of biosamples," *Anal. Bioanal. Chem.*, vol. 398, no. 5, pp. 1883 – 1889, Nov. 2010.

[197]Z. Q. Tou, C. C. Chan, and S. Leong, "A fiber-optic pH sensor based on polyelectrolyte multilayers embedded with gold nanoparticles," *Meas. Sci. Technol.*, vol. 25, no. 7, p. 075102, Jul. 2014.

[198]R. N. Smith, M. McCormick, C. J. Barrett, L. Reven, and H. W. Spiess, "NMR studies of PAH/PSS polyelectrolyte multilayers adsorbed onto silica," *Macromolecules*, vol. 37, no. 13, pp. 4830 – 4838, Jun. 2004.

[199]E. Kharlampieva, V. Kozlovskaya, O. Zavgorodnya, G. D. Lilly, N. A. Kotov, and V. V. Tsukruk, "pH-responsive photoluminescent LbL hydrogels with confined quantum dots," *Soft Matter*, vol. 6, no. 4, pp. 800 – 807, Feb. 2010.